MEDICAL DECISION MAKING – A PERSONALIZED APPROACH

A Dissertation
Presented to
The Academic Faculty

by

Xin Wei

In Partial Fulfillment
of the Requirements for the Degree
Doctor of Philosophy in the
H. Milton Stewart School of Industrial and System Engineering

Georgia Institute of Technology
August 2018

MEDICAL DECISION MAKING – A PERSONALIZED APPROACH

Approved by:

Dr. Eva K. Lee, Advisor
H. Milton Stewart School of Industrial and Systems Engineering
Georgia Institute of Technology

Dr. Andy Sun
H. Milton Stewart School of Industrial and Systems Engineering
Georgia Institute of Technology

Dr. Edwin Romeijn
H. Milton Stewart School of Industrial and Systems Engineering
Georgia Institute of Technology

Dr. Alexander Quarshie
Clinical Research Center
Morehouse School of Medicine

Dr. Yajun Mei
H. Milton Stewart School of Industrial and Systems Engineering
Georgia Institute of Technology

Date Approved: July 11, 2018

ACKNOWLEDGEMENTS

I would like to express my sincere appreciation to my advisor, Dr. Eva Lee, for her guidance, understanding and financial support for my PhD study. The accomplishment of this dissertation would have been impossible without her inspiration and instruction.

I would like to thank Dr. Edwin Romeijn, Dr. Yajun Mei, Dr. Andy Sun, and Dr. Alexander Quarshie for serving on my dissertation committee. I am particularly thankful to their valuable comments and feedback on my work.

I would like to acknowledge National Science Foundation, the National Institutes of Health, and the Centers for Disease Control and Prevention for their funding support.

I would like to acknowledge ISyE faculties for their excellent teaching, ISyE staffs for their administrative support, and current and former fellow students for their help in my academic and personal life. Specially, I want to thank the members in the Center for Operations Research in Medicine and Healthcare for their support of my research.

I also want to thank all my friends in Atlanta who accompanied with me during my PhD study. I really cherish the friendship and will remember all the happiness for my life. At last, I want to thank my parent for their endless love. I know you are always my supporters and encourage me during my PhD study.

TABLE OF CONTENTS

LIST OF TABLES

LIST OF FIGURES

SUMMARY

Medical decision making seeks to explain how physicians and patients routinely make decisions and identify both barriers and facilitators of effective decision making. In real practice, patients are different in their personal characteristics, drug response and treatment compliance. Furthermore, physicians are still depending on trial-and-error approach to treat patients. In this dissertation, we focus on developing mathematical foundation and computational tools that guide physicians (and patients) to make good decisions. Specifically, we developed models that estimate the patient's personalized response to treatment and optimized the treatment to achieve best possible outcome.

The first topic of this dissertation focuses on the management of diabetes mellitus. A pharmacokinetic and pharmacodynamics (PK/PD) drug effect model was developed to characterize the dose response of patients receiving anti-diabetic drug therapy. A linear disease progression model was combined with a drug effect model to characterize the trend of blood glucose level over time. The personalized dose response was estimated using the daily self-monitored blood glucose (SMBG) data recorded by the patient during the first 4 weeks of diabetes treatment. We tested the model on patients with gestational diabetes mellitus (GDM). Compared to the standard autoregression model, our treatment effect model gives better long-term prediction on the trend of blood glucose level. It offers the first predictive treatment-effect model which relates drug dose to drug effect.

We utilized the individualized treatment effect model and result to design a personalized treatment planning model to optimize the dosing strategy for each patient. A mixed-integer program was developed to optimize the drug prescription for each patient based on his/her

own personalized dose response and disease progression. In a retrospective study, we optimized the dose regimen using our model. Compared to the original dose regimen that is used to treat these patients in the clinic, the optimized dose regimen uses smaller or equal amount of drug but achieve better glycemic control.

The second topic focuses on the optimization of external radiation therapy. We first proposed a math programming formulation to the isocenter selection problem and developed a fast heuristic approach to determine the number and location of the isocenters of the radiation beams. Second, we proposed a multi-objective direct aperture and beam-angle model that optimizes each treatment objective based on its clinical priority. The objectives are determined by a patient's personalized need. To solve these optimization problems, we developed an efficient heuristic column generation algorithm that creates apertures without using any dose information. Finally, we incorporated a mixed-integer beam selection module into the direct aperture optimization to optimally select beam angles from which the radiation is delivered. The test result of three types of patients (lung, prostate, and intracranial cancer) shows that our method can create deliverable clinically acceptable plans within reasonable time. The resulting plans offer better dose distribution than the clinical plans with bean angles that cannot be pre-selected by human planner.

CHAPTER I

INTRODUCTION

Medical science has been greatly enriched during the last three decades. Numerous technological innovations have been developed to enable more accurate diagnosis and more effective treatment. For example, the human genome project, completed in 2003, has greatly benefitted the society and medical science[1]. Understanding the human variation can directly translate to human health with the creation of better treatments and personalized medicine. This led to extensive clinical and translational research effort in advancing early diagnosis and targeted treatment[2]. The launch of the 10-year-effort to create a national electronic medical record (EMR) system by the United State government in 2004 helped fuel the medical advance[3]. Clinicians are more eager to adopt and leverage data to help them formulate and make decisions that can benefit the patients.

While these technologies have the potential to greatly improve the health of humans, they have also increased the complexity of decision making for healthcare providers and policymakers[4]. Specifically, the process of medical decision making, including the complex tradeoffs between risks and benefits of diagnosis and treatments, is still lagged behind the advances in technology.

Clinicians began to improve the diagnosis and treatment by bringing tools from other disciplines, such as statistics, decision science and computer science. Many mathematical models have been developed to help them optimize decision making and improve treatment

outcome. Some of these models seek to explain how physicians and patients routinely make decisions and identify both barriers and facilitators of effective decision making. Others help guide physicians, patients and healthcare policymakers to make good decisions in practice. Among them, methods like simulation, optimization, machine learning have been successfully used in real practice[4-7].

One of the challenges in medical decision making is the complexity, variability and uncertainty that exist in both patients and different treatment methods. Through clinical training and residency programs, doctors learn to make their decisions based on personal experience. This results in practice variability which may affect the outcome. Clinical guidelines, which are summarized from clinical trials, are often population-specific and average out the individual variability. An effective treatment for one patient may not guarantee the same result for others. Hence, each patient must go through a trial-and-error process until the treatment outcome becomes satisfactory. This drives up the cost of healthcare and delay expected outcome.

In this dissertation, we focus on developing mathematical models that target medical treatment to personalized characteristics of each patient, which is often called *personalized medicine* (PM). Formally, personalized medicine is defined as a medical procedure that separates patients into different groups with medical decisions, practices, interventions being tailored to the individual patient based on their predicted response or risk of disease[8]. Personalized characteristics, from genetic content to all sorts of personalization measures are identified by informatics approaches. Such evidence is then used in diagnosis or treatment to improve accuracy or treatment outcome.

Inspired by this idea, we developed a personalized approach for diabetes management[9-11]. In chapter II, we derived a mathematical model to characterize the drug effect of diabetes patients taking anti-diabetes drugs[10]. The model estimates a patient's dose response and disease progression using his/her daily recorded blood glucose data. It provides an accurate long-term prediction on the trend of blood glucose level in the future. This work answers a fundamental century-long puzzle in pharmacology on how to predict dose effect without using invasive procedures to measure drug concentration in the body. In chapter III, such personalized evidence of dose response is utilized within an individualized treatment planning model that optimizes the dose regimen for diabetes[11]. Empowered by the accurate drug dose-effect prediction on each patient, the resulting optimized dose regimen achieves better glycemic control and uses less drug when compared to the original clinical treatment. Chapter II and Chapter III introduce *the first-of-its-kind* personalized drug-dose effective predictive treatment planning for diabetes management[9].

In chapter IV, we discussed the optimization of external radiation therapy treatment planning[12-14]. Radiation therapy, which uses ionizing radiation to treat cancers, has long employed sophisticated mathematics to help with personalized treatment design. Recently, it has become much more efficient by using flexible robotic systems. High-energy and precise radiation beams are produced to kill cancerous cells and keep surrounding normal tissues safe. A multi-objective model is developed where each clinical objective is optimized sequentially based on its clinical priority. Patient's anatomical structure and personalized dose requirement are considered in determining the priority and are also used

in optimization. The resulting plans are clinically acceptable with better dose distribution than the current clinical plans.

CHAPTER II

PREDICTING TREATMENT DOSE-EFFECT USING SELF-MONITORED BLOOD GLUCOSE DATA FOR DIABETES MANAGEMENT

The content of this chapter is based on two manuscripts:

[9]Eva K. Lee, X.W., Francine Baker-Witt, Michael D. Wright, Alexander Quarshie, Outcome-Driven Personalized Treatment Design for Managing Diabetes. *Interfaces - The Daniel H. Wagner Prize for Excellence in Operations Research Practice*. To appear 2018

[10]Eva K. Lee, X.W., Francine Baker-Witt, Michael D. Wright, Alexander Quarshie, Predicting Treatment Dose-effect Using Self-Monitored Blood Glucose Data for Diabetes Management. 2018: *British Journal of Clinical Pharmacology*. Manuscript submitted for publication.

2.1 Introduction

Diabetes is one of the most popular chronic disease, with a devastating impact on the affected patients and their families. As of 2015, approximately 415 million people had diabetes worldwide and is one of the top 10 leading cause of death[15]. More than $245 billion were spent for the diabetes management in 2012[16].

Patients with diabetes either cannot produce enough insulin or cannot respond properly to the insulin produced[17]. High blood glucose level is often observed in diabetic patients and increases the risk of the complications such as stroke, diabetic retinopathy and glaucoma[18]. Therefore, the management of diabetes focuses on the control of blood glucose level within the recommended range. Dietary control and physical activities are the most common interventions. If they fail to control the blood glucose level, insulin injection or oral anti-diabetic medications will be used. One of the difficulties in diabetes management is to estimate the treatment effect on patients receiving insulin or drug therapy. Since patients are different in eating habit, dose response and treatment compliance, it is hard for clinicians to figure out whether the treatment is effective or not. Therefore, clinicians still use trial-and-error approach in prescribing the drug and the dosage.

Many mathematical models are developed to help clinicians address the complexity, variability, and uncertainties of diabetes management. Computer simulation models have been used to analyze and predict the health outcomes and economic consequences of various diabetes therapies[19, 20]. These models focus on predicting the long-term treatment effects such as death rate and expected quality-adjusted life years (QALYs). Another type of model tries to describe the insulin-glucose dynamics in human body. The insulin-glucose dynamics is modeled by a set of ordinary differential equations (ODEs)[21]. The minimal model developed by Bergman et al.[22] is one of the first models that characterize the change in glucose and insulin concentration after the steady state is broken by perturbations (e.g. food intake or insulin injection). These models are commonly used to analyze the results of glucose tolerance tests, which only last for several hours.

More elegant models are proposed to capture deterioration of the β-cells over time, and allows more accurate prediction of the time course of glucose and insulin concentrations in the long run[23]. The pharmacokinetic/pharmacodynamics (PK/PD) models are proposed to study the effects of antidiabetic drugs on insulin-glucose homeostasis[24]. These models often treat the body as a system of compartments and assume that the rate of transfer between compartments follow first-order or linear kinetics. The drug effect is then described by a sigmoid function, which is driven by drug concentrations in the hypothetical effect compartment[25]. These models characterize the mechanism of drug action and, in practice, are mostly used to estimate the efficacy and toxicity of a drug on its target patients. They can also be used to explore the influence of demographic characteristics or the disease status and progression on drug effects[26]. However, some studies show that these PK/PD models cannot fit all doses simultaneously with a single set of parameters, which suggest that they cannot explain the underlying system sufficiently[27]. Advanced statistical models are also developed to analyze the dynamic of insulin glucose system and to predict blood glucose levels in the near future[28, 29]. Wang et al. developed an autoregressive model with time-varying parameters that captures the dynamic of blood glucose level in a short period of time. Compared with models with non-time-varying parameters, their model gives better prediction on near future blood glucose level based on insulin delivery and meal intake[30]. In [31], a data assimilation framework is proposed to combine the sparse measurement of glucose regulatory system with a nonlinear mechanism-based model in the ICU setting. In a simulation study, the author demonstrated that the model can predict the short-term glucose dynamics and improve the glucose control in ICU. For

these methods, complicated techniques are often needed to account for the high variability and missing values of the data, which is common in diabetes management.

The ability to estimate, predict and control blood glucose level is the most important problem in diabetes management. In this chapter, we proposed a treatment effect model combining a PK/PD drug effect model and a linear disease progression model. The model captures the drug-glucose dynamics and the effect of different drug dosages to the value of blood glucose level. Patient's personalized characteristics of dose response and disease progression are estimated by fitting the treatment effect model to the self-monitored blood glucose levels (SMBG). Although self-monitoring has long been accepted as an important component of diabetes management, it is still difficult to successfully utilize it in the treatment. To our knowledge, this is the first model that use SMBG to draw insights of the personalized drug effect and disease progression of the patient. Moreover, compared to the descriptive autoregression model, our mechanism-based model gives better forecast on the trend of blood glucose level. Therefore, it can be potentially used to optimize the dosing strategy of diabetes treatment to improve the outcome. In section 2, we will build the treatment effect model. In section 3, we test the model on 14 clinical patients with gestational diabetes mellitus(GDM) and the results will be compared to a standard autoregression model.

2.2 Methods

2.2.1 The PK/PD drug effect model

In clinical pharmacology, the intensity of pharmacological effects directly relates to the concentration of drug at the effect site[32]. Pharmacokinetic(PK) models characterize the time course of drug concentration in the body fluids. The simplest one-compartment model is particularly useful for the analysis of drugs that distribute rapidly throughout the body. According to first-order kinetics, the plasma drug concentration after a rapid intravenous injection is given by

$$C_p(t) = \frac{D}{V} e^{-k_{el} \cdot t} \tag{2.2.1}$$

where $C(t)$ is the plasma drug concentration at time t, D is the injected dose, and k_{el} is the apparent first-order elimination rate constant for the drug. Here V is the apparent volume of distribution which has no direct physiologic meaning but is an indication of the extent of drug distribution in the body[33].

Pharmacodynamics(PD) models characterize the relationship between the drug concentration and the drug effect. The effect of a drug present at the site of action is determined by that drug's binding with a receptor and the most commonly used model is the sigmoid E_{max}-model, which is of the form:

$$E = \frac{E_{max} \cdot {C_e}^n}{{EC_{50}}^n + {C_e}^n} \tag{2.2.2}$$

where E_{max} is the maximum effect, C_e is the concentration of the drug at the effect site, EC_{50} is the concentration that produces half of the maximal effect, and n is the shape factor. Here EC_{50} characterizes the potency of the drug in the system and E_{max} reflects its efficacy. Although the shape factor n is derived from receptor theory as the number of

molecules interacting with a receptor and can provide better data fits, it is rarely used in practice[32].

PK and PD models are linked together through the plasma drug concentration C_p and the effect site drug concentration C_e. The relationship between plasma and effect site concentration may either be constant or change over time. For direct link models, equilibrium between both concentrations is assumed to be rapidly achieved and thus their ratio is a constant (**fig. 2.1a**). For indirect link models, however, there is a temporal dissociation between the time course of concentration and effect, which is most likely caused by the distributional delay between the concentrations in plasma and at the effect site. A general approach to characterize this delay is the effect compartment model first introduced by Holford and Sheiner[34, 35]. A hypothetical effect-compartment is attached to the pharmacokinetic model to describe the concentration at the effect site (**fig. 2.1b**).

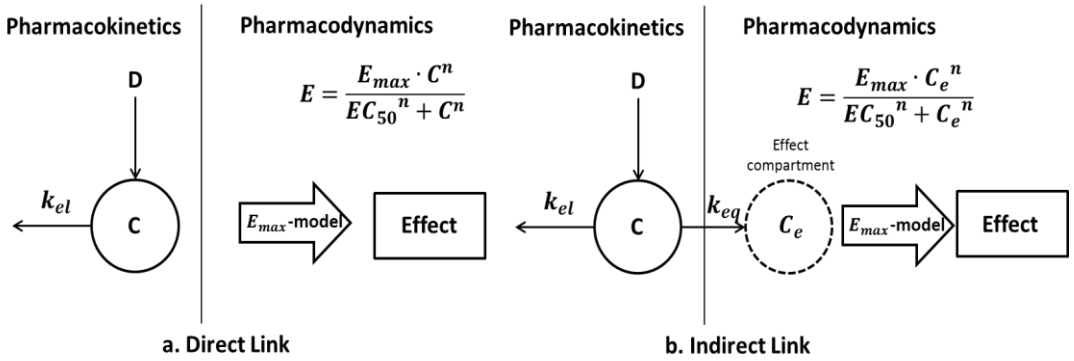

Figure 2.1. Direct link vs. indirect link models[32]. Two ways to calculate the effect site drug concentration C in the drug effect E_{max}-model. (a) Direct link model uses plasma drug concentration C_p as C. (b) Indirect link model uses effect compartment drug concentration $C_e = C_p \cdot \left(1 - e^{-k_{eq} \cdot t}\right)$ as C.

To see the relationship of C_p and C_e in the indirect link models, assume that the drug influx into the effect compartment follows a first-order process. Then we have

$$\frac{dC_e}{dt} = k_{eq} \cdot (C_p - C_e) \tag{2.2.3}$$

where k_{eq} is the equilibration rate constant. Solving this differential equation, we have

$$C_e(t) = C_p(t) \cdot \left(1 - e^{-k_{eq} \cdot t}\right). \tag{2.2.4}$$

Therefore, by substituting (2.2.4) into (2.2.2) and let the shape factor $n = 1$, the drug-concentration drug-effect relationship can be modeled as

$$E(t) = \frac{E_{max} \cdot C_p(t) \cdot \left(1 - e^{-k_{eq} \cdot t}\right)}{EC_{50} + C_p(t) \cdot \left(1 - e^{-k_{eq} \cdot t}\right)} \tag{2.2.5}$$

Since it is impossible to measure drug concentration frequently, $C_p(t)$ is often replaced by its estimation. For example, Frey et al. compensated for the lack of concentration by using the area under the curve[36].

$$E(t) = \frac{E_{max} \times AUC \times (1 - e^{-k_{eq} \cdot t})}{AUC \times \left(1 - e^{-k_{eq} \cdot t}\right) + AUC_{50}} \tag{2.2.6}$$

Area under the concentration-time curve (AUC), which is the integration of (2.2.1) from zero to infinity represents the total drug exposure over time and is used in computing the average drug concentration over a time period. Most drugs are administered periodically with sufficient frequency to maintain the presence of drug in the body. For drugs given in a fixed dose at a constant dosing interval, they accumulate in the body until a steady-state plasma level is achieved. At steady-state, the drug concentration at any time during any

dosing interval will be identical to the concentration at the same time during any other dosing interval[33](**fig. 2.2**). Suppose a drug is administered at dose D with dosing interval τ for N intervals, then the drug concentration at time $N \cdot \tau + t$ will be

$$C_N(t) = \frac{D}{V} e^{-k_{el} \cdot t} \cdot \sum_{n=0}^{N} e^{-n \cdot k_{el} \cdot \tau} = \frac{D}{V} e^{-k_{el} \cdot t} \cdot \frac{(1 - e^{-(N+1) \cdot k_{el} \cdot \tau})}{(1 - e^{-k_{el} \cdot \tau})} \tag{2.2.7}$$

So the steady state drug concentration at any time t is given by

$$C_{ss}(t) = \lim_{N \to \infty} C_N(t) = \frac{D}{V} \cdot \frac{e^{-k_{el} \cdot t}}{(1 - e^{-k_{el} \cdot \tau})}, \quad t \in [0, \tau) \tag{2.2.8}$$

By (2.2.8), we have the following relationship:

$$AUC_1{}^{0-\infty} = \int_0^{\infty} C(t)dt = \frac{D}{V \cdot k_{el}} = \int_0^{\tau} C_{ss}(t)dt = AUC_{ss}{}^{0-\tau} \tag{2.2.9}$$

Therefore, AUC during any dosing interval at steady state ($AUC_{ss}{}^{0-\tau}$) is the same as the overall AUC after the first dose ($AUC_1{}^{0-\infty}$) and $AUC_{ss}{}^{0-\tau} = \frac{D}{V \cdot k_{el}}$. Finally, by substituting $AUC_{ss}{}^{0-\tau}$ with $\frac{D}{V \cdot k_{el}}$ in (2.2.6), we have

$$\begin{aligned} E(t) &= E_{max} \times \frac{\frac{D}{V \cdot k_{el}} \times (1 - e^{-k_{eq} \cdot t})}{\frac{D}{V \cdot k_{el}} \times \left(1 - e^{-k_{eq} \cdot t}\right) + AUC_{50}} \\ &= E_{max} \times \frac{D \cdot R_d \cdot \left(1 - e^{-k_{eq} \cdot t}\right)}{1 + D \cdot R_d \cdot \left(1 - e^{-k_{eq} \cdot t}\right)} \end{aligned} \tag{2.2.10}$$

Here, for model simplicity, we combine pharmacokinetic parameters into $R_d = \frac{1}{V \cdot k_{el} \cdot AUC_{50}}$ (mg^{-1}). It reflects the drug sensitivity of a patient as the drug will be more effective for patients having larger R_d.

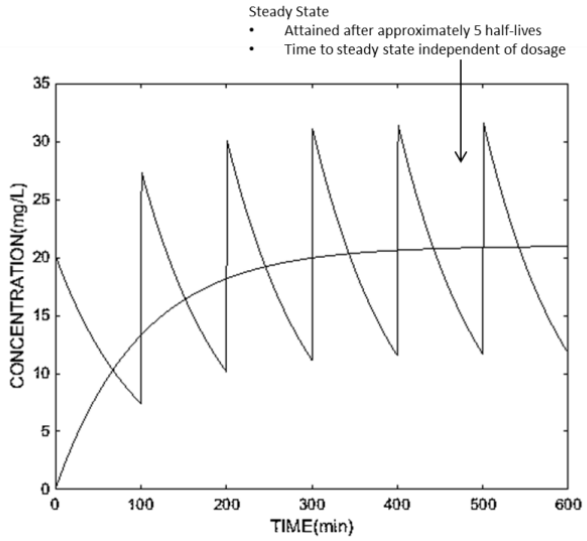

Figure 2.2. This figure shows the time course of drug concentration after multiple intravenous dosing with $D = 200$ mg; $V = 10$L; $k_{el} = 0.1$ min^{-1} and $\tau = 100$ min. Since no absorption time is considered, the drug concentration will spike suddenly at each drug administration time.

2.2.2 Treatment effect model combining disease progression

The treatment effect of diabetes management consists of two main parts: disease progression and drug effect. Frey et al. proposed a mixture model capturing both parts of the diabetes treatment. In their model, the fasting plasma glucose level (FPG) for a patient taking an anti-diabetic drug can be represented by

$$FPG(t) = Base + S(t) - E(t) \tag{2.2.11}$$

where $FPG(t)$ is the fasting blood glucose at time t, $Base$ is the predicted baseline level, $S(t)$ is the disease progression model, and $E(t)$ the drug effect model. Since diabetes is a progressive disease, patient's ability to control blood glucose will gradually get worse over time. Therefore, the blood glucose level is expected to increase if the patient is left alone without any interventions. A linear time disease progression is commonly used[37], which

is $S(t) = \alpha \cdot t$ with constant α. By substituting the PK/PD drug effect model (2.2.10) into (2.2.11), the blood glucose level can be represented as

$$BGL(\boldsymbol{\beta}, t) = Base + \alpha \cdot t - E_{max} \cdot \frac{D \cdot R_d \cdot \left(1 - e^{-k_{eq} \cdot t}\right)}{1 + D \cdot R_d \cdot \left(1 - e^{-k_{eq} \cdot t}\right)} \tag{2.2.12}$$

where parameters $\boldsymbol{\beta} = (Base, \alpha, E_{max}, R_d, k_{eq})$.

The behavior of blood glucose level under this model can be divided into three phases according to the behavior of the function $BGL(\boldsymbol{\beta}, t)$. Notice that there are two roots of $\frac{\partial BGL}{\partial t}(\boldsymbol{\beta}, t) = 0$, denoted as $0 < t_1 < t_2$. When $t < t_1$, the blood glucose level will gradually increase. Before t_1, drug has not fully taken effect as the equilibrium between plasma and effect site drug concentration is not reached. Between t_1 and t_2, the drug effect becomes stronger and the blood glucose level start declining. After t_2, the level increases again as the disease progression dominates the drug effect again. It means that the drug, under current dosage D, is no longer effective to control the blood glucose level and a dose escalation is required. (2.2.12) is also the first to establish the direct relationship between drug dosage and the blood glucose level. This model, applied to each patient, can potentially help clinicians improve their dosing strategy during the treatment to achieve better outcome.

We are going to implement the treatment effect model to estimate the personalized disease progression and dose response of GDM patients and forecast the long-term variations of the blood glucose level. Under (2.2.12), the SMBG data collected during the treatment is the consequence of drug effect of the dose regimen combined with disease progression

over time. Let D_{t} denote the dosage level at time t and $\{D_{\mathrm{t}}, \mathrm{t} = 1 \ldots \mathrm{T}\}$ denote the dose regimen during the treatment. We can rewrite (2.2.12) as a difference equation

$$BGL(\boldsymbol{\beta}, t+1) = BGL(\boldsymbol{\beta}, t) + \alpha - E_{max} \cdot \frac{D_{\mathrm{t}} \cdot R_d \cdot k_{eq} \cdot e^{-k_{eq} \cdot t}}{\left(1 + D_{\mathrm{t}} \cdot R_d \cdot \left(1 - e^{-k_{eq} \cdot t}\right)\right)^2} \quad (2.2.13)$$

Here, $\alpha - E_{max} \cdot \frac{D_{\mathrm{t}} \cdot R_d \cdot k_{eq} \cdot e^{-k_{eq} \cdot t}}{\left(1 + D_{\mathrm{t}} \cdot R_d \cdot \left(1 - e^{-k_{eq} \cdot t}\right)\right)^2}$ is the first-order derivative of $BGL(\boldsymbol{\beta}, t)$ with respect to t. Therefore, the whole drug-glucose system can be represented as a discrete nonlinear state-space system, where the state transition equation is

$$BGL(\boldsymbol{\beta}, t+1) = BGL(\boldsymbol{\beta}, t) + \alpha - E_{max} \cdot \frac{D_{\mathrm{t}} \cdot R_d \cdot k_{eq} \cdot e^{-k_{eq} \cdot t}}{\left(1 + D_{\mathrm{t}} \cdot R_d \cdot \left(1 - e^{-k_{eq} \cdot t}\right)\right)^2} + \eta_{\mathrm{t}}, \quad \mathrm{t} = 1 \ldots \mathrm{T} \quad (2.2.14)$$

and the measurement equation is

$$L(t) = BGL(\boldsymbol{\beta}, t) + \varepsilon_t, \quad \mathrm{t} = 1 \ldots \mathrm{T} \quad (2.2.15)$$

Here $\eta_t \sim N(0, Q_t)$ is the Gaussian white noise representing the unmodeled disease process and $\varepsilon_t \sim N(0, H_t)$ is the Gaussian white noise modeling the blood glucose measurement error. The dose regimen $\{D_{\mathrm{t}}, \mathrm{t} = 1 \ldots \mathrm{T}\}$ is the control variable and $L(t)$ is the SMBG readings observed at time t. Kalman filtering method (KF) is commonly used to fit the system (2.2.14) ~ (2.2.15) to the data and forecast future blood glucose levels. The value of $BGL(\boldsymbol{\beta}, t+1)$ is first predicted based on the value of $L(1) \ldots L(t)$ and is then corrected after $L(t+1)$ is observed. However, the standard KF method is only designed to give a one-step-ahead prediction and is theoretically difficult to make accurate multi-step predictions[38, 39]. As our goal is to develop a model that can give long-term prediction

of the treatment effect, we need to modify (2.2.14) and (2.2.15). In the treatment of diabetes, the daily record of blood glucose level is highly stochastic due to various food intake. The trend of blood glucose level, which is the moving average of daily blood glucose level, tells the efficacy of the treatment. For example, an effective treatment will result in the decline of blood glucose level over time. Moreover, a model that can give accurate long-term prediction on the trend of blood glucose level can potentially help clinicians adjust their dose regimen promptly. Therefore, we use equation (2.2.12) and $BGL(\boldsymbol{\beta}, t)$ to directly estimate the trend of blood glucose level

$$BGL(\boldsymbol{\beta}, t) = Base + \alpha \cdot t - E_{max} \cdot \frac{D_t \cdot R_d \cdot \left(1 - e^{-k_{eq} \cdot t}\right)}{1 + D_t \cdot R_d \cdot \left(1 - e^{-k_{eq} \cdot t}\right)} + \phi_t, \quad t = 1 \ldots T \qquad (2.2.16)$$

where $\phi_t \sim N(0, \Phi_t)$ is the white noise capturing the errors of the trend to the actual blood glucose level.

2.2.3 Fitting the treatment effect model by SMBG data

In this study, self-monitored blood glucose(SMBG) data from real clinical treatment are used to estimate the parameters in the model. Let $\{l_1, l_2, \ldots, l_T\}$ denote the blood glucose level recorded from day 1 to day T, then parameter $\boldsymbol{\beta}$ for that phase is obtained by solving the non-negative least square (NNLS) problem

$$\boldsymbol{\beta}^* = \underset{\beta \geq 0}{\operatorname{argmin}}\, Err(\boldsymbol{\beta}) = \underset{\beta \geq 0}{\operatorname{argmin}} \sum_{t=1}^{T} (l_t - BGL(\boldsymbol{\beta}, t))^2 \qquad (2.2.17)$$

An efficient gradient descent algorithm is developed to solve (2.2.17). To ensure non-negativity of $\boldsymbol{\beta}$ throughout the gradient descent algorithm, we first replace $\boldsymbol{\beta}$ with $\widehat{\boldsymbol{\beta}} = \left(ln(Base), ln(\alpha), ln(E_{max}), ln(R_d), ln\left(k_{eq}\right)\right)$.

Define $\mathrm{T}(\boldsymbol{\beta}, D_{\mathrm{t}}, t) = \alpha - E_{max} \cdot \frac{D_{\mathrm{t}} \cdot R_d \cdot k_{eq} \cdot e^{-k_{eq} \cdot t}}{\left(1 + D_{\mathrm{t}} \cdot R_d \cdot \left(1 - e^{-k_{eq} \cdot t}\right)\right)^2}$ as the treatment effect at time t with dose D_{t}. By (2.2.13), we have

$$BGL\left(\widehat{\boldsymbol{\beta}}, t+1\right) = BGL\left(\widehat{\boldsymbol{\beta}}, 0\right) + \sum_{s=0}^{t} \mathrm{T}(\widehat{\boldsymbol{\beta}}, D_s, s)$$

$$= Base + \alpha \cdot t - \sum_{s=0}^{t} E_{max} \cdot \frac{D_s \cdot R_d \cdot k_{eq} \cdot e^{-k_{eq} \cdot s}}{1 + D_s \cdot R_d \cdot \left(1 - e^{-k_{eq} \cdot s}\right)} \qquad (2.2.18)$$

And the gradient is calculated as

$$\frac{\partial BGL(\widehat{\boldsymbol{\beta}}, t)}{\partial \widehat{\boldsymbol{\beta}}} = \frac{\partial BGL(\widehat{\boldsymbol{\beta}}, 0)}{\partial \widehat{\boldsymbol{\beta}}} + \sum_{s=0}^{t} \frac{\partial^2 T}{\partial \widehat{\boldsymbol{\beta}} \partial s}\left(\widehat{\boldsymbol{\beta}}, D_s, s\right) \qquad (2.2.19)$$

Therefore, $BGL\left(\widehat{\boldsymbol{\beta}}, t\right)$ and its gradient $\frac{\partial BGL(\widehat{\boldsymbol{\beta}}, t)}{\partial \widehat{\boldsymbol{\beta}}}$ can be obtained simultaneously as we calculate the objective value $Err\left(\widehat{\boldsymbol{\beta}}\right)$, which is efficient in terms of computational cost.

2.3 Result and Discussion

We tested the treatment effect model on 14 de-identified patients with GDM. Eight of them are African American, and six are Caucasian American. Furthermore, three patients have history of GDM; three have a history of DM; 4 patients are obese; one patient has hypotension; and one patient is blind.

2.3.1 Establishing the predictive treatment effect parameters

In this study, SMBG data from real clinical treatment are used to fit the treatment effect model. Each patient was asked to record her blood glucose level at 4 different times/phases of a day: before breakfast(BB), after breakfast(AB), after lunch(AL) and after dinner(AD) until delivery. Since the activity and food intake are different between different phases, each phase will have its own treatment effect model fitted by the SMBG data recorded at that phase. For example, a patient may have a good glycemic control before breakfast but a poor control after breakfast because she is not compliant to diet control. Therefore, each patient will have 4 sets of parameters of the treatment effect model estimated to characterize her personalized disease progression and dose response.

Missing data are common in SMBG as patients often forget or fail to measure it. Although a SMBG reading may be missing on day t, the prescription dose D_{t} is known and both $BGL(\boldsymbol{\beta}, t)$ and the gradient will be calculated. However, they are only used in the calculation of future BGL and are excluded in the calculation of the total squared error $Err(\boldsymbol{\beta})$.

Since the problem $\min_{\beta \geq 0} Err(\boldsymbol{\beta})$ is nonconvex in the corresponding parameters $\boldsymbol{\beta}$, the gradient descent algorithm cannot guarantee global optimality of the solution. As a result, different choices of the initial value of $\boldsymbol{\beta}$ can lead to different estimations. To avoid local optima and ensure the quality of the solution, we run the algorithm 10 times with different initial values and choose the one with the minimum estimation error. Different initial values are chosen according to the population mean and variance of these parameters in the literature[36] as we assume that the value of these parameters for each patient will not

differ very much to the population mean. For these patients with gestational diabetes, according to our experiment, the initial value for $Base$ could be 90 ± 10 mg·dl^{-1} for the phase of before breakfast and 130 ± 10 mg·dl^{-1} for other phases. α could be 0.005 ± 0.001 mg·dl^{-1}·day^{-1}, E_{max} could be 90 ± 10 mg·dl^{-1}, R_d could be 0.2 ± 0.1 mg^{-1} and k_{eq} could be 0.05 ± 0.01 day^{-1}. However, in real practice, other values can be used to shows the importance of each parameter in the model and reflects clinician's initial judgement of the patient's dose response.

2.3.2 Model validation and comparison

The moving average(MA) is often used to uncover the trend of the time series data. Therefore, we will compare the moving average of blood glucose level to the predicted level to evaluate the performance of our model. For time series $\{X_t\}$ the moving average of window size q is defined by

$$W_t = (2q-1)^{-1} \sum_{j=-q}^{q} X_{t-j} \qquad (2.3.1)$$

Based on the SMBG data, we calculated the moving average of the blood glucose level with window size 7 (**fig. 2.3 left**). By checking the residual of the glucose data, we can assume that the data series, after subtracting the moving average, is approximately stationary (**fig. 2.3 right**). The outliers are chosen if they are three times standard deviation away from the value moving average.

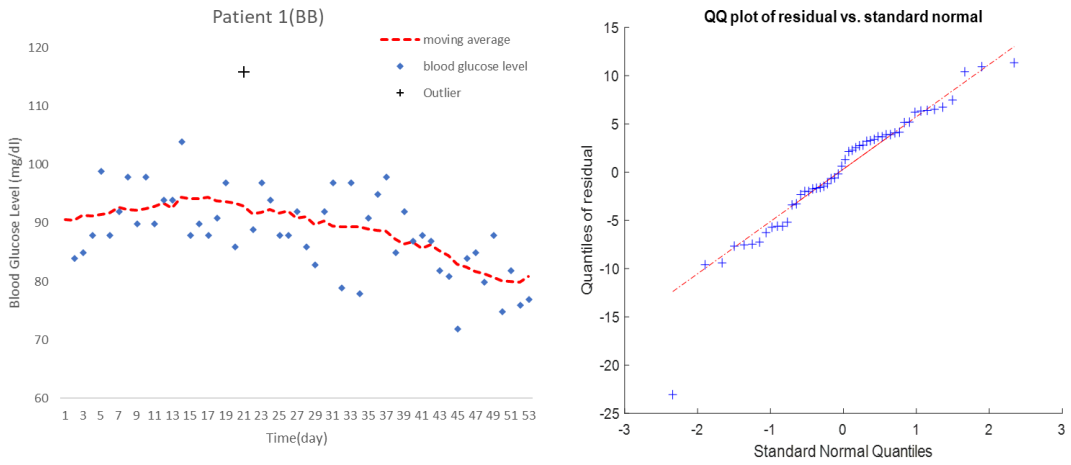

Figure 2.3. Left: Blood glucose level recorded before breakfast of patient 1. Right: Q-Q plot of the residual of blood glucose data after the moving average is subtracted

We also developed an autoregression model(AR) to compare with our treatment effect model. Autoregression models are commonly used to describe certain time-varying process. The model specifies that the signal is linearly dependent on its previous values and a stochastic noise. In this study, an AR model describing the SMBG data is developed as follows:

$$BGL(t) = c + \theta_1 \cdot BGL(t-1) + \theta_2 \cdot BGL(t-2) \; + \gamma \cdot D_t + \delta \cdot t \; + \varepsilon_t, \;\; t = 1 \ldots T-1 \quad (2.3.2)$$

This is an AR model with lag 2 and constant c, exogenous predictor variables D_t and linear trend value δ. ε_t is the random Gaussian noise. We used AR(2) model simply because it gives better fitting than AR(1) model based on our experiment. The biggest difference between (2.2.13) and (2.3.2) is the term that characterizes the treatment effect. In (2.2.13), the treatment effect is modeled as the mixed effect of disease progression and drug effect, $\alpha - E_{max} \cdot \frac{D_t \cdot R_d \cdot k_{eq} \cdot e^{-k_{eq} \cdot t}}{\left(1 + D_t \cdot R_d \cdot \left(1 - e^{-k_{eq} \cdot t}\right)\right)^2}$. In (2.3.2), this part is modeled as a linear combination of

drug dosage D_t and treatment time t. Therefore, we want to explore the benefit of using mechanism-based PK/PD model against the descriptive model totally based on the observed data.

For both methods, the dosage level D_t comes from the dose regimen that clinicians used for the patient in real treatment. The patients and her doctor meet every week to monitor the disease progression. Drug dosage will possibly be changed after checking the outcome of previous regimen. For each patient, the first 4 weeks of SMBG data (or first 50% for small datasets), which we refer to as the titration period, are used to fit both models. Once the parameters are estimated, the remaining data is used to validate the predicted blood glucose level of the model. The blood glucose values after the 4th week is predicted by the fitted model using the original dose regimen applied for the patient. For the AR(2) model, the value is predicted by

$$BGL(t) = \hat{c} + \hat{\theta}_1 \cdot BGL(t-1) + \hat{\theta}_2 \cdot BGL(t-2) + \hat{\gamma} \cdot D_t + \hat{\delta} \cdot t\,, \quad t = 1 \ldots T-1 \qquad (2.3.3)$$

where $\hat{c}, \hat{\theta}_1, \hat{\theta}_2, \hat{\gamma}, \hat{\delta}$ are the maximum likelihood estimators. For the treatment effect model, the value is predicted by

$$BGL(t+1) = BGL(t) + \hat{\alpha} - \hat{E}_{max} \cdot \frac{D_t \cdot \hat{R}_d \cdot \hat{k}_{eq} \cdot e^{-\hat{k}_{eq} \cdot t}}{\left(1 + D_t \cdot \hat{R}_d \cdot \left(1 - e^{-\hat{k}_{eq} \cdot t}\right)\right)^2} \qquad (2.3.4)$$

and $BGL(0) = \widehat{Base}$. The parameter $\hat{\alpha}, \hat{E}_{max}, \hat{R}_d, \hat{k}_{eq}$ and $\widehat{Base}$ are then obtained by solving (2.2.17) by gradient descent algorithm.

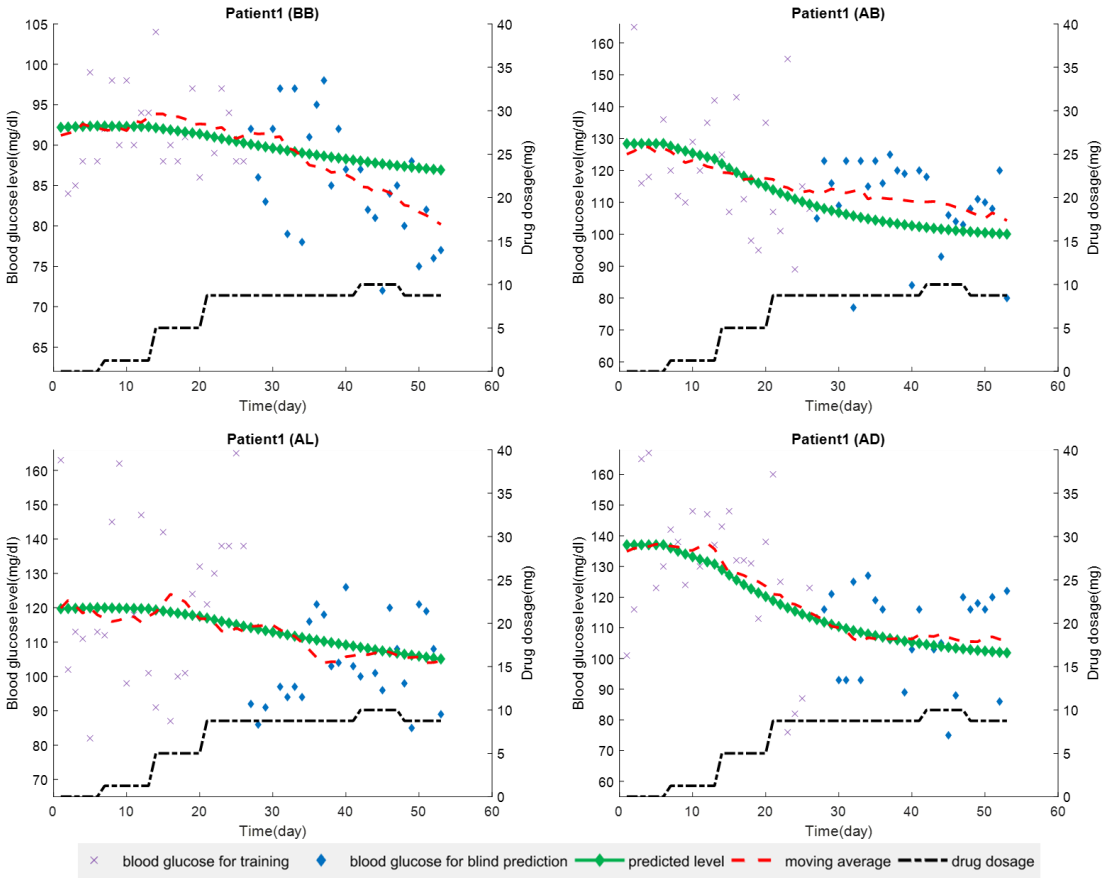

Figure 2.4. Result of fitting the treatment effect model for patient 1 in all 4 phases: before breakfast(BB), after breakfast(AB), after lunch(AL), after dinner(AD). The moving average(red dotted line) is calculated using all SMBG data with window size 7. The predicted level(green curve) is obtained by using the treatment effect model fitted by the first 4 weeks SMBG data(purple cross) and the dose regimen(black dash dotted line).

The result of fitting the treatment effect model for patient 1 is shown in **fig. 2.4**. Several dose escalations occur during the early stage of the treatment (titration period) and the maintenance dose of 8.75mg is kept for most of the time during the rest of treatment. Therefore, the trend of blood glucose level, under such dose regimen, is gradually decreasing over time. The treatment effect model captures the disease progression and dose response information of the patient from the titration period and gives good prediction on the trend of blood glucose level after the titration period. The AR(2) model, fitted by the

same training data, gives less accurate prediction on the trend of blood glucose level (**fig. 2.5**). For all 4 phases, the predicted blood glucose level is higher than the moving average. The prediction accuracy of the two methods is measured and compared by the root-mean-square error (RMSE) defined as

$$RMSE = \sqrt{\left(\frac{\sum_{t=1}^{T}(\text{observation}_t - \text{prediction}_t)^2}{T}\right)} \tag{2.3.5}$$

Across all 14 patients, the RMSE of the treatment effect model is less than the AR(2) model. The average of the percentage of RMSE reduction, calculated as $\frac{RMSE_{TE} - RMSE_{AR}}{\text{RMSE}_{\text{AR}}} \times 100\%$, is -8.77% with $95\%\ \text{CI} = [-16.73, -0.81]$ for before breakfast, -7.23% with $95\%\ \text{CI} = [-19.69, 5.23]$ for after breakfast, -9.87% with $95\%\ \text{CI} = [-18.14, -1.60]$ for after lunch and -9.49% with $95\%\ \text{CI} = [-21.54, 2.55]$ for after dinner. The result shows that our treatment effect model performs better at predicting the long-term blood glucose level than the AR(2) model. SMBG data often has high variability due to personalized food intake and poor compliance. Additionally, missing data is common as patients often forget to record it. Therefore, the AR model, like other descriptive methods, gives worse estimation and prediction for such dataset. However, our treatment effect model shows that it is robust to high variability and large amount of missing data. It models the underlying drug-glucose mechanism which is not directly reflected by the SMBG data.

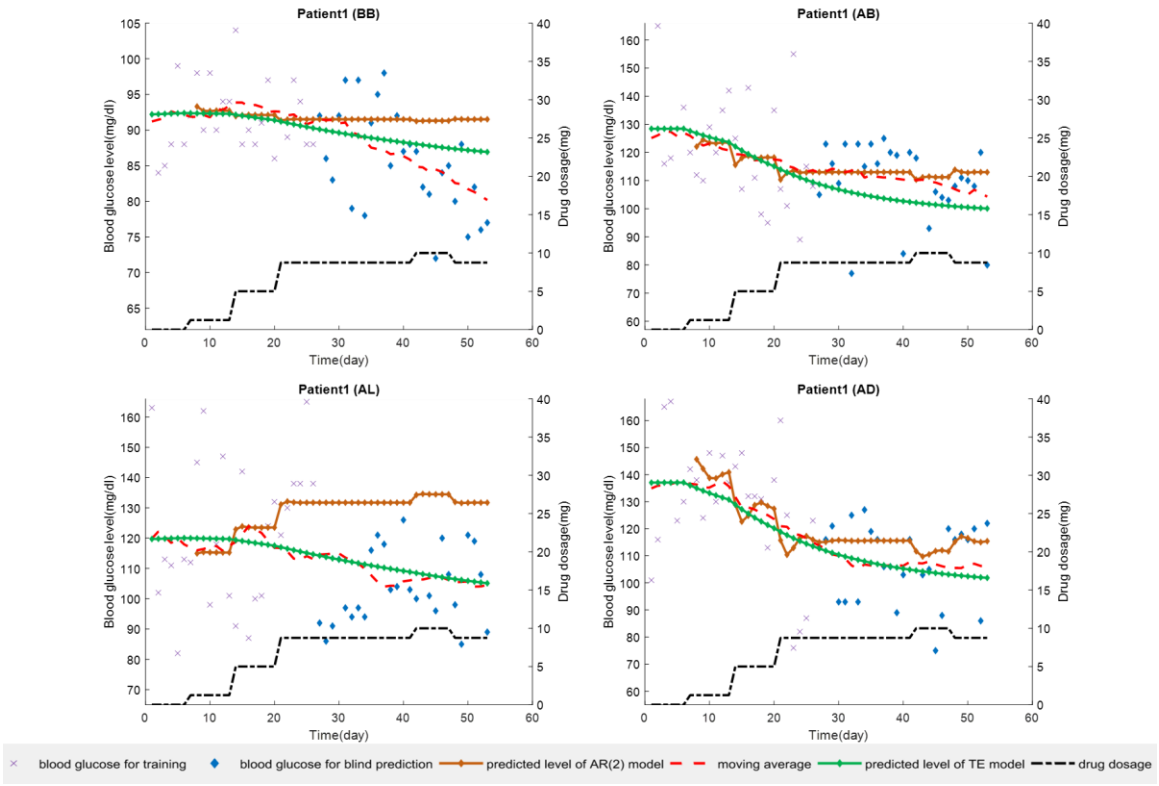

Figure 2.5. Result of fitting the AR(2) model for patient 1 in all 4 phases: before breakfast(BB), after breakfast(AB), after lunch(AL), after dinner(AD). The first 4 weeks data(purple line) are used for fitting the model and the first week data serve as the initial value for predicting future values. The predicted level of AR(2) model(orange curve) is compared to the moving average(red dotted line) and the predicted level of the treatment effect model(green curve).

2.4 Conclusion

In this chapter, we developed a treatment effect model that combines disease progression with a PK/PD drug effect model. This mechanism-based PK/PD model establishes the direct relationship between drug dosage and drug effect (the amount of decrease in blood glucose level), which overcomes the obstacle of many existing models that require continuous measurement of insulin or drug concentration in the blood. It utilizes the most commonly collected SMBG data in diabetes management to estimate the dose response of the patients. By using her own SMBG data recorded in titration period, the fitted model

tells the personalized characteristics of each patients, including dose response, disease progression and compliance. Moreover, compared to descriptive models, the model gives better long-term prediction on the trend of blood glucose level. Such information can help clinicians get a better understanding of each patient and target treatment to the patient's specific needs. Also, it is the first model that tries to build the direct relationship between drug dosage and blood glucose level. Therefore, doctors can quantitatively optimize the dosing strategy based on patient's personalized disease progression and dos response so that better treatment outcome can be achieved. Currently, the treatment of GDM and other types of diabetes rely heavily on clinicians' experience. However, it is unrealistic to expect the human mind to be able to address the complexity, variability, and uncertainties of health and disease. Therefore, this treatment effect model, which only uses SMBG, provides clinicians a good insight on a patient's personalized dose response and potentially guides their decision making during the treatment.

With more patients studied, we can use machine learning techniques to identify specific characteristics of patients that relate to the dose response and disease progression pattern. Therefore, patient's dose response can be predicted at the beginning of the treatment so that personalized treatment can be implemented.

CHAPTER III

DOSE-EFFECT EVIDENCE-BASED PERSONALIZED TREATMENT PLANNING FOR MANAGING GESTATIONAL DIABETES MELLITUS

The content of this chapter is based on two manuscripts:

[9]Eva K. Lee, X.W., Francine Baker-Witt, Michael D. Wright, Alexander Quarshie, Outcome-Driven Personalized Treatment Design for Managing Diabetes. *Interfaces - The Daniel H. Wagner Prize for Excellence in Operations Research Practice*. To appear 2018

[11]Eva K. Lee, X.W., Francine Baker-Witt, Michael D. Wright, Alexander Quarshie, Dose-effect Evidence-based Personalized Treatment Planning for Managing Gestational Diabetes Mellitus. 2018: *Diabetes Care.* Manuscript submitted for publication.

3.1 Introduction

Gestational diabetes mellitus (GDM) is defined as any degree of glucose intolerance with onset or first recognition during pregnancy[40]. Women with GDM and elevated glucose levels are at higher risks of maternal and fetal complications during pregnancy and birth, including shoulder dystocia, birth injuries, hypoglycemia, respiratory distress syndrome, cesarean section, pre-eclampsia and fetal overgrowth[41]. It can also trigger the occurrence of type-2 diabetes for mothers after pregnancy[42]. GDM affects up to 7% of all

pregnancies, resulting in over 200,000 cases annually[43], and incurs approximately $636 million of annual treatment cost[44].

Though the precise mechanisms underlying gestational diabetes remain unknown, the diagnosis of GDM presumes a threshold value above which women are at increased risk of pregnancy complications[45]. It is shown that the risk for both short-term and long-term complications can be mitigated by glycemic control during pregnancy[46]. As a result, the management of GDM targets close monitoring of blood glucose levels up to 4 times a day: before breakfast (fasting level) with goal $\leq$ 95 mg/dl and two hours after each meal with goal $\leq$ 120mg/dl[47]. The treatment of GDM is similar to Type 2 diabetes. Dietary control and physical activities are the most common interventions. If they fail to control the blood glucose level, more effective insulin therapies will be prescribed[48]. Oral hypoglycemic agents (OHAs), though not approved by FDA for treating pregnant women, are also common GDM drugs because of easy usage and low cost. Glibenclamide/Glyburide, which is used in this study, has been proven an effective alternative to insulin for achieving adequate glycemic control[49]. In real practice, combination therapies are often prescribed to achieve better treatment outcome.

Many clinical trials have been performed to evaluate the efficacy of different types of therapies for GDM[50-56]. Scarpello reviewed the United Kingdom Prospective Diabetes Study and identified an optimal dosing strategy for treating diabetes with metformin[57]. The author showed that the anti-hyperglycemic efficacy of metformin increases with increasing daily doses between 500 mg and the upper limits of the recommended daily dosage ($\geq$ 2000 mg/day). Alwan et al. systematically reviewed eight different randomized controlled trials, contrasting GDM treatment plans versus maternal and infant outcomes.

Comparing specific treatment (e.g. dietary advice, glucose monitoring, and insulin therapy) with routine antenatal care, there was a reduction in the proportion of infants weighing more than 4 kilograms or greater than 90th birth percentile. While GDM treatment appears to be useful, there is no evidence indicating which treatment is best or how long-term treatment outcomes can be assessed[58].

One of the key problems in diabetes management is to choose the right drug with right dose to treat the right patient. However, it becomes increasingly complex now because of the variability in patients and the widening alternatives of pharmacological agents. Clinicians make their decisions based on personal experience and clinical guidelines. These evidence-based advice, which mainly comes from clinical trials, does not address the different choices of drugs and only shows the median responses of the recruited patients. In this chapter, we address the dosing strategy in GDM management by introducing a patient-centered decision support tool that couples a treatment-effect model with a dose optimization mode. The treatment-effect model, which is introduced in the chapter II, is a mechanism-based PK/PD model that captures the underlying glucose dynamics and personalized drug effects of each patient. Self-monitoring of blood glucose (SMBG) is commonly used as a tool of self-management in diabetes treatment. However, the effectiveness of SMBG on glycemic control is still not clear[59]. Our model provides a new mathematic tool to utilize SMBG data in diabetes management. These data, which are recorded by patients at home, are used to estimate the personalized disease progression and dose response characteristics of patients. And a mixed-integer program is developed to utilize this patient-specific information and optimize the dose regimen in a given treatment

horizon. To the best of our knowledge, this is the first model that quantitatively optimizes dosing strategy through mathematical programming.

3.2 Method

3.2.1 The treatment effect model

To optimize the dosing strategy, we need to first estimate the effect of drugs on the blood glucose level. In chapter II, we developed a mechanism-based treatment effect model that build the direct relationship between the drug dosage to the blood glucose level. In that model, the blood glucose level changes by a combination effect of linear disease progression and drug effect from anti-diabetic drugs.

$$BGL(t) = Base + \alpha \cdot t - E_{max} \cdot \frac{D \cdot R_d \cdot \left(1 - e^{-k_{eq} \cdot t}\right)}{1 + D \cdot R_d \cdot \left(1 - e^{-k_{eq} \cdot t}\right)}$$

where $Base$ is the baseline blood glucose level at the beginning of the treatment. α is the constant rate of disease progression. As diabetes is a progressive disease, the blood glucose level is expected to increase due to the deterioration of the ability to control glucose by patients themselves. The drug effect term $E_{max} \cdot \frac{D \cdot R_d \cdot \left(1 - e^{-k_{eq} \cdot t}\right)}{1 + D \cdot R_d \cdot \left(1 - e^{-k_{eq} \cdot t}\right)}$ models the expected reduction of blood glucose level by taking drug with dosage D.

In chapter II we showed that the treatment effect model can give good estimate and forecast of the trend of blood glucose level during the treatment. The model has four distinct features. First, the PK/PD drug effect model captures the drug-glucose dynamics and

uncovers the effect of different drug dosages on the value of blood glucose level. Though PK/PD models are widely used in all phases of preclinical and clinical drug development, little research has been done to apply those concepts in clinical therapy. Second, self-monitored blood glucose (SMBG) data are utilized to fit the model and estimate the personalized dose response and disease progression. This data is readily available as SMBG is widely used in diabetes management. Therefore, unlike other models which requires continuous monitoring of drug concentration in body fluids, our model is easily implementable in current clinical setting. Third, this mechanism-based PK/PD model, fitted by the blood glucose level recorded during the titration period (dosing experiment period), has the ability to predict the blood glucose level in the future. Compared to the descriptive autoregression models, our model is robust to the high variability and large number of missing values in SMBG data and gives better long-term prediction on the trend of blood glucose level. Last and most importantly, the model is fitted for each patient separately to get the personalized characteristics of dose response and disease progression.

3.2.2 Dose Optimization Model

The management of GDM starts with the diagnosis of the gestational diabetes (usually at weeks 24-28) and ends after the delivery. There are 3 types of treatment for gestational diabetes: (1) diet control only, (2) oral hypoglycemic agents (OHAs) therapy with diet control, and (3) insulin therapy with diet control. In this dissertation, we only consider the first two methods since insulin therapy is not used for our patients. The initial plan is decided when diagnosis is made and is set by determining the treatment type and the dosage level. The decisions on whether to maintain or switch treatment type or dose are made at

subsequent clinical visits until delivery. Patients are asked to record their blood glucose level at different times/phases of a day. The decisions are made after assessing the impact of prior treatment according to the self-monitored blood glucose (SMBG) data (**fig. 3.1**). Therefore, the dosing strategy is to decide on the weekly dosage level of the drug.

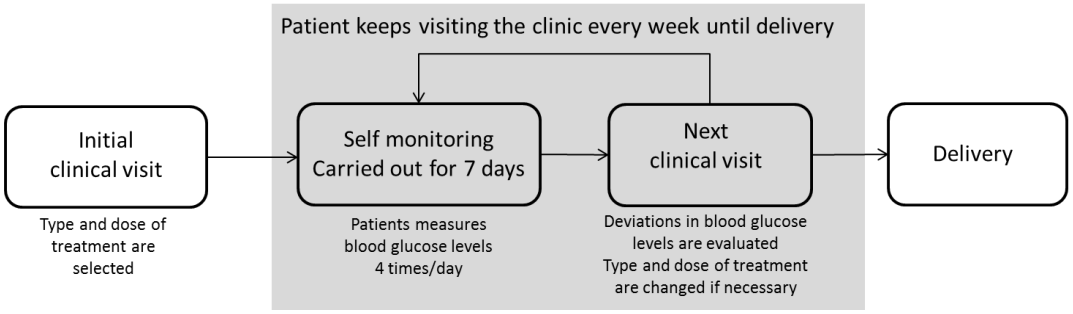

Figure 3.1. Decision process for the treatment of pregnant women with gestational diabetes

Currently the dosing strategy of GDM relies heavily on the result of clinical trials and clinician's personal experience. However, clinical trials often address the (trial) patient population for whom the intervention is appropriate, instead of individual patient characteristics. A trial-and-error approach is often used for clinicians to overcome the complexities and variabilities in each patient. In this paper, we developed a mixed-integer program that incorporates the treatment effect model to individualize and optimize the dosing strategy for treating GDM patients. Each patient's personalized disease progression and dose response are estimated from the daily SMBG data. The treatment effect model, as shown in chapter II, can give long-term prediction on how the trend of blood glucose level goes given different drugs and dosages. Therefore, we can quantitatively optimize the dose regimen for a given period of treatment to better control the blood glucose. Since the

estimations and predictions are based on patient's individual evidence, the optimized dose regimen tailors to the patient specific characteristics so that the treatment outcome is better than a trial-and-error approach.

In **Table 3.1** below, we introduce the parameters and decision variables used in our model.

Indices	
$\boldsymbol{w}$	index for week, $w = 1, \dots, W$
$\boldsymbol{m}$	index for phase of daily blood glucose level, $m = 1, \dots, 4$
$\boldsymbol{t}$	index for days during a week, $t = 1, \dots, 7$
$\boldsymbol{i}$	drug dosage level, $i = 0, \dots, L$
Parameters	
$\boldsymbol{g(m, w, t, i)}$	Treatment effect for dosage level i at week w day t and phase m.
$\boldsymbol{C_+}$	Cost of positive deviation of blood glucose level from upper bound level
$\boldsymbol{C_-}$	Cost of negative deviation of blood glucose level from lower bound level
$\boldsymbol{C(i)}$	cost of drug at dosage level i
$\boldsymbol{W}$	total number of weeks
$\boldsymbol{L}$	total number of dosage levels (dosage level increase 1.25mg per level).
$\boldsymbol{k_+}$	maximum positive dosage level change between 2 consecutive decisions
$\boldsymbol{k_-}$	maximum negative dosage level change between 2 consecutive decisions
$\boldsymbol{T(m)}$	upper bound of blood glucose level for phase m
$\boldsymbol{B(m)}$	lower bound of blood glucose level for phase m
Decision variables	
$\boldsymbol{x(w, i)}$	binary decision variable equals 1 if dosage level i is applied for week w, 0 otherwise.
$\boldsymbol{s(m, w, t)}$	blood glucose level at week w day t phase m
$\boldsymbol{p(m, w, t)}$	positive deviation of blood glucose level at week w day t phase m
$\boldsymbol{n(m, w, t)}$	negative deviation of blood glucose level at week w day t phase m

The treatment planning model can be formulated as

$$(\textbf{MIP})\ Min \quad \sum_m \sum_w \sum_t f_1(m,w,t) + \sum_w \sum_i f_2(w,i)$$

$$s.t. \quad f_1(m,w,t) = C_+ \cdot p(m,w,t) + C_- \cdot n(m,w,t), \quad \forall\, m = 1 \dots 4, w = 1 \dots W, t = 1 \dots 7 \tag{3.2.1}$$

$$f_2(w,i) = C(i) \cdot x(w,i), \quad \forall\, w = 1, \dots W, i = 0, \dots, L \tag{3.2.2}$$

$$\sum_i x(w,i) = 1, \quad \forall\, w = 1 \dots W \tag{3.2.3}$$

$$s(m,w,t) = s(m,w,t-1) + \sum_i g(m,w,t-1,i) \cdot x(w,i), \forall\, m = 1 \dots 4, w = 1 \dots W, t = 1 \dots 7 \tag{3.2.4}$$

$$s(m,0,0) = base(m), \forall\, m = 1 \dots 4 \tag{3.2.5}$$

$$p(m,w,t) \geq s(m,w,t) - T(m), \quad \forall\, m = 1 \dots 4, w = 0 \dots W, t = 1 \dots 7 \tag{3.2.6}$$

$$n(m,w,t) \geq B(m) - s(m,w,t), \quad \forall\, m = 1 \dots 4, w = 0 \dots W, t = 1 \dots 7 \tag{3.2.7}$$

$$x(w-1,i) + \sum_{j<i-k_-} x(w,j) + \sum_{j>i+k_+} x(w,j) \leq 1, \forall\, w = 1, \dots W, i = 0, \dots, L \tag{3.2.8}$$

$$s \geq 0, p \geq 0, n \geq 0, x \in B^{W \times L},\ x(0,0) = 1 \tag{3.2.9}$$

There are two objectives in this mixed-integer program. The first objective (3.2.1) is to minimize the total positive and negative deviation of the blood glucose level to the recommended target level. The positive deviation is calculated by (3.2.6) where the upper bound is 120mg/dl to ensure satisfactory glycemic control. The negative deviation is calculated by (3.2.7) where the lower bound is set to be 60mg/dl to avoid hypoglycemia. Basically, we want to control the expected blood glucose level within 60mg/dl ~ 120mg/dl. The second objective (3.2.2) is to minimize the total drug dosage. Although OHAs are commonly used for treating GDM, they are not formally approved. Minimizing dosage thus serves to improve safety for these patients. Constraint (3.2.3) ensures that a dosage level is selected for each week. Since OHAs are mostly in the form of pills, drug dosage in our model is restricted to discrete level. Dosage level 0 implies that the patient is on diet control and no drug is administered for that week. Constraints (3.2.4) ~ (3.2.5) calculate

the change of blood glucose level as a result of the drug dosage, as modelled in chapter II. Here we use the (2.2.13), which is

$$BGL(t+1) = BGL(t) + \alpha - E_{max} \cdot \frac{D_t \cdot R_d \cdot k_{eq} \cdot e^{-k_{eq} \cdot t}}{\left(1 + D_t \cdot R_d \cdot \left(1 - e^{-k_{eq} \cdot t}\right)\right)^2} \tag{3.2.10}$$

Therefore,

$$g(m, w, t, i) = \alpha(m) - E_{max}(m) \cdot \frac{D_i \cdot R_d(m) \cdot k_{eq}(m) \cdot e^{-k_{eq}(m) \cdot (7w+t)}}{1 + D_i \cdot R_d(m) \cdot \left(1 - e^{-k_{eq}(m) \cdot (7w+t)}\right)} \tag{3.2.11}$$

where D_i is the i-th dosage level. The parameters $(Base, \alpha, E_{max}, R_d, k_{eq})$ are estimated from patient's daily SMBG readings of phase m. As a result, the optimized dose regimen will be personalized. Constraint (3.2.8) follows clinical practice that the dosage level should not fluctuate too much from one visit to the next. Since there is no national standard regarding the choice, the fluctuation allowed can be physician dependent. In practice, clinicians always start with diet control only at the start of the visit. We comply with this practice by setting the initial treatment at week 0 with no dosage, which is $x(0,0) = 1$.

3.3 Result and discussion

A retrospective analysis of 14 de-identified patients is performed in this study. **Table 3.2** shows the statistics of these patients. Eight of them are African American, and six are Caucasian American. Furthermore, three patients have history of GDM; three have a history of DM; 4 patients are obese; one patient has hypotension; and one patient is blind.

Table 3.2. Patient statistics by age, height, weight, BMI and length of GDM treatment

	Age	Height(inch)	Weight(lb)	BMI($kg \cdot m^{-2}$)	Length(day)
Min	20	59	122	22.7	26
Max	41	70	260	50.8	153
Mean	33.7	62.9	184.5	32.8	79.5
Median	34.5	62	181.5	33.2	68.5
Standard deviation	5.3	3.0	38.6	6.5	38.8

For each patient, the blood glucose level is recorded at 4 different phases of a day: before breakfast(BB), after breakfast(AB), after lunch(AL) and after dinner(AD). Therefore, each patient will have 4 sets of parameters of the treatment effect model estimated to characterize her personalized disease progression and dose response.

The parameters of the treatment effect model are obtained by a fast gradient descent algorithm described in chapter II. They are then put into (3.2.4) and (3.2.5) to formulate the optimization model. The treatment horizon is set to be the same as the real treatment. All patients are treated by Glyburide and the dosage level is discretized as 1.25mg per level, which is the minimum weight of a Glyburide tablet sold in drug store. The upper bound target blood glucose levels are 95mg/dl before breakfast and 120mg/dl after meals. A lower bound baseline blood glucose levels of 60mg/dl for all 4 phases are also included to avoid hyperglycemia.

The optimization problem is solved by CPLEX® 12.6. Even though the model is a mixed-integer program, it has a simple constraint sets and can be solved efficiently. The average solution time of 14 patients is 3.27 secs. In **fig. 3.2 left**, we contrast the optimized regimen to the original regimen of patient 5. The optimized regimen achieves uniformly lower blood

glucose level than the original one. In terms of total positive deviation, which is calculated as $\sum_t (BGL(t) - T)_+$, where $x_+ = \max(x, 0)$ and T is the upper bound blood glucose level, the optimized dosing strategy results in lower (or the same) value for all 4 phases compared to the original treatment regimen (**fig. 3.2 right**).

Table 3.3 summarizes the optimized dose regimen produced by our model and the comparison to the original dose regimen used in real treatment. In this retrospective study, we observe that the optimized dose regimen from our model tends to prescribe a higher dose early on, and there is no change on dosage after Week 3. Therefore, the titration period is significantly shortened, and the maintenance dosage level will be quickly achieved. This demonstrates that, with accurate estimation of patient's dose response characteristics, the model allows clinicians to prescribe higher dose at the early stage with confidence without the concerns of overdosing. This is in agreement with recommendations to quickly increase the dose of oral hypoglycemic agent until adequate glycemic control is achieved or response is not observed[36].

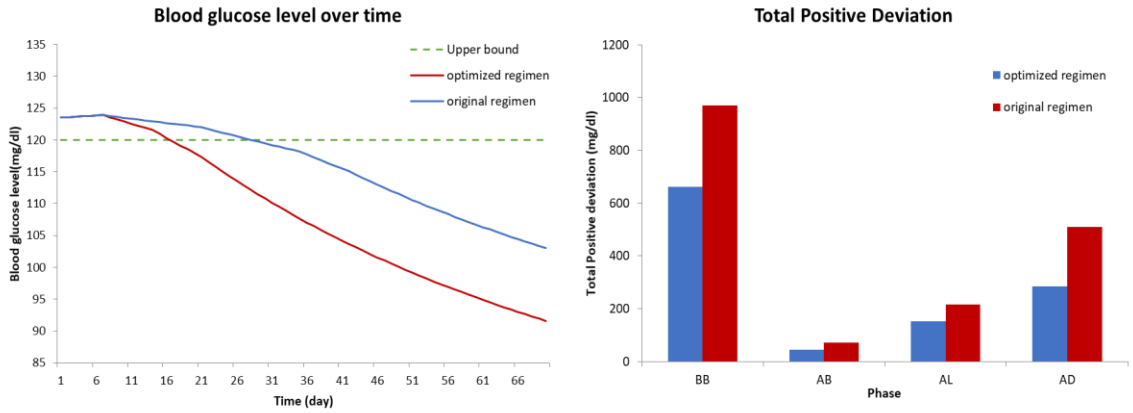

Figure 3.2. Comparison of original regimen vs. optimized regimen of patient 5. Left: the predicted trend of blood glucose level under the treatment effect model using original and optimized regimen. Right: total positive deviation of blood glucose level of original and optimized regimen of each phase.

Among these 14 cases, 4 of the optimized plans are identical to the original plans (Patients 4, 7, 12, 13). Of the remaining 9, all experience reduction in blood glucose (**fig. 3.3**) and 4 of the optimal plans use fewer drugs, too. We could not draw any conclusion for Patient 6 because of large number of missing data. From the result, we can see that the optimized dose regimen can provide better glycemic control and use fewer drugs at the same time. This proves that the dose optimization model, incorporated by the predictive treatment effect model can potentially can produce a personalized, drug efficient dose regimen that maximizes the treatment outcome for GDM patients.

Table 3.3. This table compares the dosage level of the optimized regimen (Opt) versus the original clinical regimen (Real) in a 10-week treatment horizon. Dosage prescribed for each week are shown and followed by the difference of total positive deviation of glucose level between optimized plan and the original plan. A negative value indicates that the optimized plan is better in glycemic control than the clinical plan. All 4 phases are reported.

	Patient 1		Patient 2		Patient 3		Patient 4		Patient 5	
week	Real[1]	Opt[2]	Real	Opt	Real	Opt	Real	Opt	Real	Opt
1	0	0	0	0	0	0	0	0	0	0
2	1.25	5	2.5	5	5	5	5	5	2.5	5
3	5	5	3.75	10	10	6.25	5	5	2.5	10
4	8.75	5	3.75	15	10	6.25	5	5	5	15
5	8.75	5	5	15	10	6.25	5	5	5	15
6	8.75	5	5	15	10	6.25	5	5	10	15
7	10	5	5	15	10	6.25	5	5	15	15
8	8.75	5	6.25	15	15	6.25	5	5	15	15
9			8.75	15			5	5	15	15
10			8.75	15			5	5	15	15
Total	51.25	35	48.75	120	70	42.5	45	45	85	120
Reduction of total positive deviation over the entire treatment horizon (Opt – Real, mg/dl)[3]										
BB	-	0.00	-	-48.86	-	-1.99	-	0.00	-	-307.15
AB	-	-36.73	-	0.00	-	-26.73	-	0.00	-	-27.19
AL	-	-42.25	-	0.00	-	-23.61	-	0.00	-	-63.83
AD	-	-23.70	-	-36.60	-	-16.60	-	0.00	-	-223.37

Table 3.3 continued

	Patient 6		Patient 7		Patient 8		Patient 9		Patient 10	
week	Real	Opt	Real	Opt	Real	Opt	Real	Opt	Real	Opt
1	2.5	0	0	0	0	0	2.5	0	0	0
2	5	5	0	0	5	5	2.5	0	0	1.25
3	5	6.25	0	0	5	6.25	2.5	0	0	1.25
4	7.5	6.25	0	0	5	6.25	2.5	0	5	1.25
5			0	0	5	6.25	2.5	0	5	1.25
6			0	0			2.5	0	5	1.25
7			0	0			2.5	0	5	1.25
8			0	0			2.5	0	5	1.25
9			0	0			2.5	0	5	1.25
10			0	0			2.5	0	5	1.25
Total	20	17.5	0	0	20	23.75	25	0	35	11.25
Reduction of total positive deviation over the entire treatment horizon (Opt – Real, mg/dl)[3]										
BB	-	N/A	-	0.00	-	0.00	-	0.00	-	-9.52
AB	-	N/A	-	0.00	-	-0.08	-	0.00	-	0.00
AL	-	N/A	-	0.00	-	0.00	-	0.00	-	0.00
AD	-	N/A	-	0.00	-	-0.03	-	0.00	-	0.00

Table 3.3 continued

	Patient 11		Patient 12		Patient 13		Patient 14	
week	Real	Opt	Real	Opt	Real	Opt	Real	Opt
1	0	0	0	0	0	0	0	0
2	2.5	5	0	0	0	0	0	5
3	2.5	8.75	0	0	0	0	5	5
4	2.5	8.75	0	0	0	0	2.5	5
5	5	8.75	0	0	0	0	5	5
6	5	8.75	0	0	0	0	5	5
7	5	8.75	0	0	0	0	5	5
8	5	8.75	0	0	0	0	5	5
9	5	8.75	0	0	0	0	5	5
10	7.5	8.75	0	0			5	5
Total	40	75	0	0	0	0	37.5	45
Reduction of total positive deviation over the entire treatment horizon (Opt – Real, mg/dl)[3]								
BB	-	-527.03	-	0.00	-	0.00	-	0.00
AB	-	-36.10	-	0.00	-	0.00	-	-36.73
AL	-	0.00	-	0.00	-	0.00	-	-42.25
AD	-	-361.27	-	0.00	-	0.00	-	-23.70

1. Original clinical regimen used in the real treatment

2. Optimal regimen produced by our optimization model

3. Total positive deviation of optimal regimen– total positive deviation of original regimen (over the entire treatment horizon)

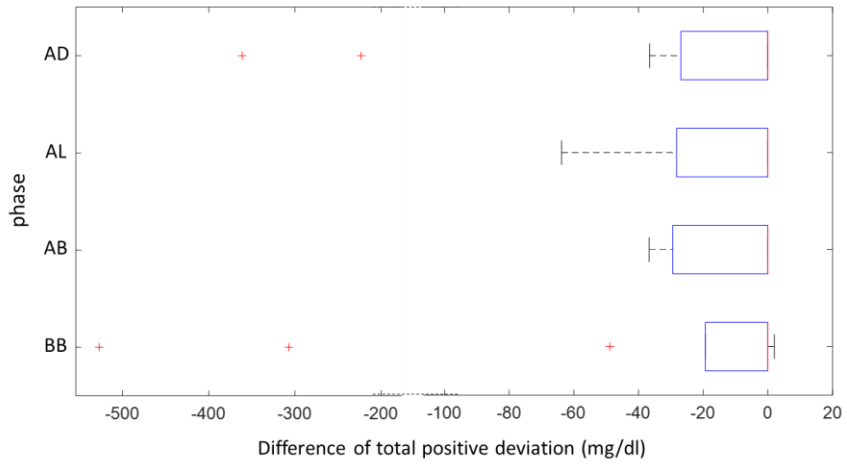

Figure 3.3. Box-Whisker plot of the reduction of total positive deviation over the entire treatment horizon of each phase

There are two objectives in the optimization: health outcome, which is the total positive and negative deviation of blood glucose level, and drug dosage cost. We optimize them by using the weighted sum of two objectives. The cost of drug increases with the dosage level. $C(i) = i, i = 0, \dots, 16$ where i corresponds to dosage level $1.25 * i$ mg. Define $\alpha = C_+/C(1)$ as the ratio of the cost of total positive deviation to the cost of drug dosage. The blood glucose level from optimized dose regimen never goes below the lower bound. So we do not consider C_- here. The different choices of ratio α reflect the importance of each objectives. With the increase of α, the optimized dosing strategy will change from minimizing drug dosage to improving health outcome (**fig. 3.4 left**). Since high blood glucose level relates to complications in delivery, glycemic control is more important than drug cost in managing GDM. From the experiment on all patient cases, there is no significant changes on the value of total positive deviation when α is greater than 0.3(**fig. 3.4 right**). Therefore, we select $\alpha = 0.3$ in the optimization to place more emphasis on the health outcome than drug dosage cost.

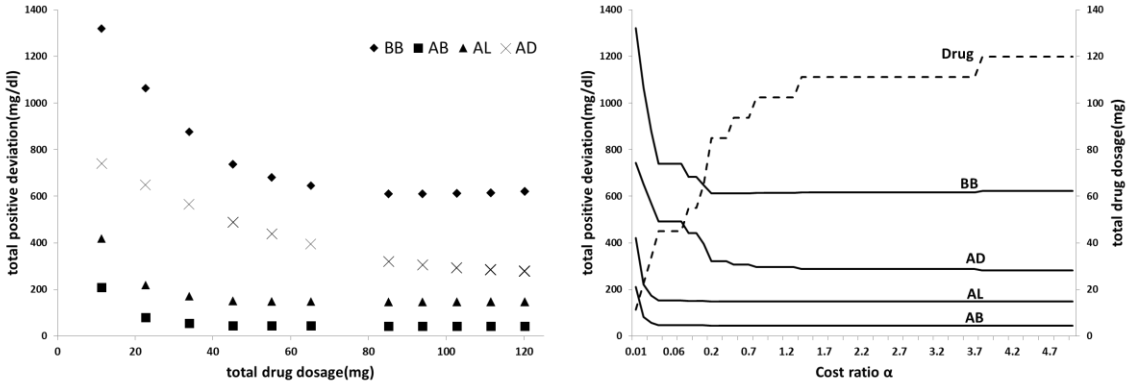

Figure 3.4. Left: The efficient frontier of the two-objective optimization. The numbers are the different cost ratio α. Right: The change of total drug dosage and total positive deviation for optimized plan as the cost ratio α increases.

3.4 Conclusion

In this chapter, we developed a dose optimization model for treating gestational diabetes. The model incorporates patient's personalized dose response characteristics to individualize and optimize the weekly dose prescription in a given treatment horizon. Such personalized evidence is estimated by a treatment effect model developed from classic PK/PD theory. This mechanism-based model provides a new mathematical way to analyze the daily SMBG data recorded by patients at home and extract insights of patient's unique disease progression and dose response information. Moreover, it provides an opportunity to quantitatively optimize the dosage level to manage the disease effectively. In a retrospective study, we tested the model on 14 clinical patients with GDM. The optimized regimens from our model, compared to the original regimens, produce better glycemic control with even smaller amount of drug prescribed. Moreover, this mixed-integer dose optimization model is solved fast and can be potentially used in real-time setting such as insulin pump therapy. Our method provides an analytic tool to help clinicians overcome

the complexity and variability in diabetes management and improve their decision making on dose prescription. In the future, more practical constraints can be identified by doctors and added to the optimization model to improve the result.

This work forms the foundation of a larger study of treatment of general diabetes patients. We have performed a larger study that involves hundreds of patients (GDM patients, and other types of diabetic patients) to further explore and validate our model [8]. We caution that clinical trials have to be carried out to confirm the potential gain in outcome.

CHAPTER IV

MULTI-OBJECTIVE DIRECT APERTURE OPTIMIZATION MODEL FOR RADIOTHERAPY PLANNING

The content of this chapter Section 4.2 and 4.3 is based on three submitted manuscripts:

[12]Eva K. Lee, X. Wei, Z. Li, Isocenter Selection in Radiation Therapy Treatment Planning. 2018: *Medical Physics*. Manuscript submitted for publication.

[13]Eva K. Lee, X. Wei, Z. Li, A Multi-Objective Direct Aperture and Beam Angle Optimization Model for External Beam Radiotherapy. 2018: *International Journal of Radiation Oncology • Biology • Physics*. Manuscript submitted for publication.

[14]Eva K. Lee, Y. Cao, X. Wei, Z. Li, Strategies in Aperture Generation within a Multi-Objective Direct Aperture and Beam Angle Optimization Framework. 2018: *International Journal of Radiation Oncology • Biology • Physics*. Manuscript submitted for publication.

4.1 Introduction

4.1.1 Background

Cancer is a major cause of morbidity and mortality with approximately 14 million new cases and 8 million cancer-related deaths worldwide in 2012[60]; and more than half of the patients receive radiotherapy during the course of treatment. Radiotherapies use ionizing radiation to damage the DNA of cells and exploit the fact that the recovery ability of cancerous cells is less efficient than that of normal cells. Therefore, the goal of radiotherapy

is to deliver sufficient dose to the tumor cells while sparing the surrounding normal tissues and critical organs. In external radiotherapy, this is achieved by using linear accelerator (LINAC) to generate multiple beams from different angles to crossfire the tumor so that tumor cells can be killed at a sufficiently high probability to control malignant disease and normal cells are kept safe by receiving a relatively low dose (**fig. 4.1**). Such technique is also known as three-dimensional conformal radiation therapy (3-DCRT). Field-shaping devices (e.g. wedges, blocks) are used to make the dose volume conform to the target shape. Beam parameters including beam geometries, beam weights will be set in a trial-and-error way to generate the best possible plan[61].

Intensity modulated radiation therapy, which is often called IMRT, improves the 3-DCRT by modifying the beam intensities across a radiation field using multi-leaf collimators (MLC). This increased freedom provides the ability to better shape the high dose volume to the tumor while avoiding the normal tissues. The optimization of IMRT plans starts with the desired dose requirement for tumor and normal organs and works backward to optimize the beam intensities. This is often referred to as inverse treatment planning[62]. In 2008, Otto introduced volumetric modulated arc therapy (VMAT) technique that allows machine dose-rate variation and can deliver the plan in a single arc of up to 360 degree[63]. The CyberKnife^{TM} system (Accuray Incorporated, Sunnyvale, CA, USA) uses a LINAC mounted on a robotic arm to deliver radiation with non-isocentric and non-coplanar beams with high precision. A tracking system is also implemented to monitor the respiration motion of patients during treatment and adjust the delivery configuration accordingly[64]. Other techniques are also developed to treat specific tumors. For example, Gamma knife,

which uses many beams with low intensity to target one or more tumors, is very effective in killing tiny tumors in brain and has little side effect on normal brain tissues.

In general, the treatment planning process of radiation therapy consists of the following steps:

- 3D Imaging of tumor sites and the surrounding region
- Delineating tumor and other anatomical structures
- Determining the required dose to tumor and tolerance dose to normal structures
- Selecting a set of beam orientations and target points
- Calculating dose for each beam
- Optimizing beam intensity for each beam selected
- Generating collimator shapes from beam intensity for actual delivery

These steps are usually performed sequentially. However, some can be combined together to improve the efficiency of the process.

Accurate imaging plays an important role in radiotherapy planning. 3D information of the tumor mass and affected region is obtained through computed tomography (CT) scan. Other methods like magnetic resonance imaging (MRI) may also be used to fuse with CT scan to allow radiation oncologist to more accurately identify the location and size of the tumor. The International Commission on Radiation Unites and Measurements (ICRU) has defined various volumes related to tumor[65]. The gross tumor volume (GTV) is defined to be the gross demonstrable volume of the malignant growth, which is generally the tumor seen from the CT image. Clinical target volume (CTV), expands GTV to include suspected region of tumor growth. It highly depends on the knowledge of the tumor type and the

patients personalized characteristics. To account for the uncertainties from both the CT imaging and the knowledge of tumor growth, a planning target volume (PTV) is defined to include additional margins to ensure adequate coverage of the target. In addition, organs at risk (OARs) are also delineated to consider the normal tissue structures whose functionality are prone to be damaged by radiation. All these structures are delineated by drawing the contours along their boundaries and the volumes are discretized into voxels at the same resolution of CT image. Combined with CT values, this volumetric information is stored in digital imaging and communications in medicine (DICOM) format for file transfer and future treatment planning (**fig. 4.2**).

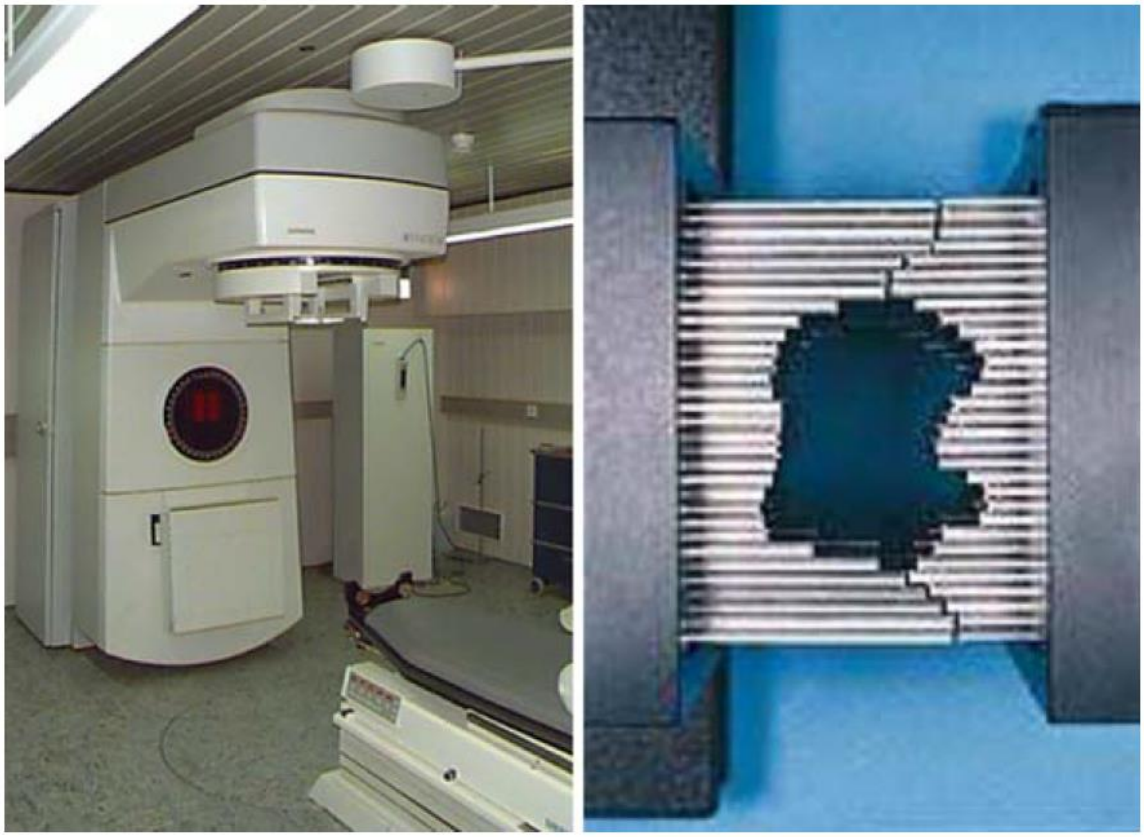

Figure 4.1. Left: A LINAC system[66]. Right: Multi-leaf collimator[67]

The treatment goals for each organ are determined by the radiation oncologists. First, to ensure the effectiveness of the treatment, a prescription dose is assigned to cover the PTV volume (e.g., > 95%). This is clinician-dependent and may vary across sites. The radiation exposure of normal tissues and critical organs must be kept to minimal. Therefore, dose spillage outside PTV should be minimized and the dose falloff should be rapid in all directions away from PTV. For OARs, the dose requirements often include maximum dose and dose volume limit, which constrains the dose distribution in OARs. For example, the volume (or percentage of volume) of an OAR with dose more than 10Gy should be less than 1cc (or 90%). Finally, the total dose of radiation is divided into several smaller doses over a period of several days, which is called dose fractionation. This procedure maximizes the effect of radiotherapy and reduces the toxic effect deposited to healthy tissues. Treatment objectives are often determined following common clinical protocols and personalized adjustments will be made to tailor patient's specific needs. The Radiation Therapy Oncology Group (RTOG), published more than 300 protocols for different tumor sites and radiotherapy delivery techniques.

The radiation dose is the amount of energy absorbed by tissues per unit of mass and is measured in the unit Gray (Gy) with $1\,\mathrm{Gy} = 1\,\mathrm{J/kg}$. The current dose calculation algorithms can be classified into three types: correction-based method, model-based method and the Monte Carlo method. Correction-based algorithms use parameters of dose measured in water phantoms and modify the data to apply to the patient's specific characteristics. Beam field shapes, irregular surface of the patient and heterogeneity of tissue densities are taken into account to calculate the dose. Though these methods are simple and fast, the accuracy is often lower than the other two methods[61]. Model-based

methods, however, directly compute the dose by modeling the beam and its interactions in the patient. It assumes that any beam hitting on the patient is actually a bunch of small and narrow “pencil beams”. Once a pencil beam hits the surface of the patient, dose will be deposited and spread out under the surface. The dose distribution of the pencil beam is often estimated by Monte Carlo simulation and is referred to as dose kernel. Then the dose of each voxel is calculated by the integration of dose deposited from all the surrounding pencil beams to that voxel, which is also called superposition. As inhomogeneities exists in real patients, different anatomical structures have different photon attenuation and dose absorption. Therefore, the dose distribution of each pencil beam is corrected based on voxel properties (usually CT number) through ray-tracing[68]. Fast convolution-superposition methods have been developed [69] and GPU acceleration has been used to speed up the superposition calculation[70], which makes them the most widely used algorithms in commercial treatment planning systems. The Direct Monte Carlo method, compared to the former methods, is the most accurate in terms of dose computation, especially in complex situations. The dose distribution of a beam is obtained by creating a large number of particles with their attenuation and scattering behavior simulated by computer[71]. To reduce errors of simulation, huge number of particles are often simulated which often makes the dose calculation time-consuming. Dose calculation plays a critical role in radiotherapy treatment planning and its accuracy directly relates to the quality of the plan optimization and delivery process.

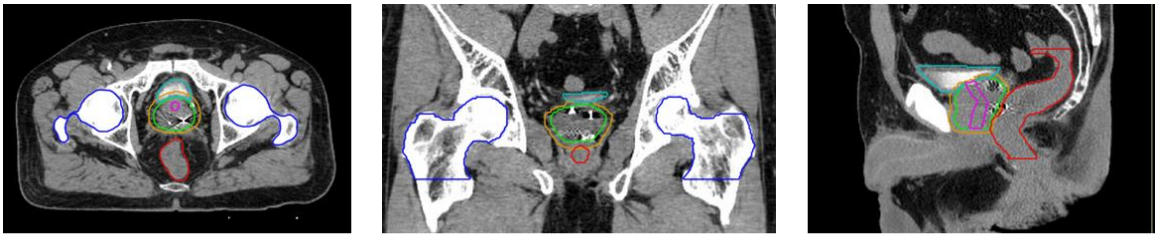

Figure 4.2. The DICOM image showing a case of prostate cancer. Anatomical structures: GTV(green), PTV(yellow), Bladder(light blue), Prostatic urethra(pink), Rectum(red), Femoral heads(dark blue)

4.1.2 Treatment planning

Since the publication of Shepard et al. [72], inverse planning of radiotherapy becomes one of the most important applications of operations research and various algorithms have been designed to solve this problem[73]. Generally, the treatment planning of radiotherapy consists of three sequential phases: beam angle optimization (BAO), fluence map optimization (FMO), and leaf sequencing (LS). Each process can be optimized separately or combined together to solve.

The BAO problem is to find the best selection of beam angles from which the beams are sent off. Beam selection is fundamental to the concept of cross-firing of radiation source. A plan with too many beams is time-consuming to deliver and may lead to errors due to its complexity. It may also increase the radiation exposure of critical organs. Moreover, BAO is very important in cases when the tumor shape is irregular or critical organs wrap around the tumor. In practice, usually a candidate set of beam angles is predetermined/chosen by the planner. These beam angles, either coplanar or non-coplanar, are often evenly distributed in the space. Angles that interfere with the patient will be eliminated. The

optimization of beam angles is combinatorial and computationally difficult to solve. Ehrgott et al. presented a minimum cost set covering approach to beam selection. The model requires each voxel to be covered by at least one angle and the cost of each beam angle is assigned to be proportional to the cost of violating the dose upper bound of OARs which that beam pass through[74]. Another way to score each beam is based on its ability of delivering more dose to the target without violating dose restrictions on the non-targeted regions[75]. Scoring functions are also used in heuristic iterative methods such as local search[74, 76, 77], simulated annealing[78, 79], genetic algorithm[80, 81] and particle swarm optimization (PSO)[82]. The PSO algorithm starts with a set of particles with each represents a selection of beam angles. In each iteration, each particle updates its beam selection based on the personal best solution, global best solution and a random shift. As iteration increases, the population (called swarm) of particles will converge to a local optimal beam selection. BAO problem is very closely related to the FMO problem which optimizes the intensities of beams. In all the heuristic algorithms mentioned above, whether mentioned explicitly or not, essentially solve the two problems consecutively. The combined models will be discussed together with FMO in the next paragraph.

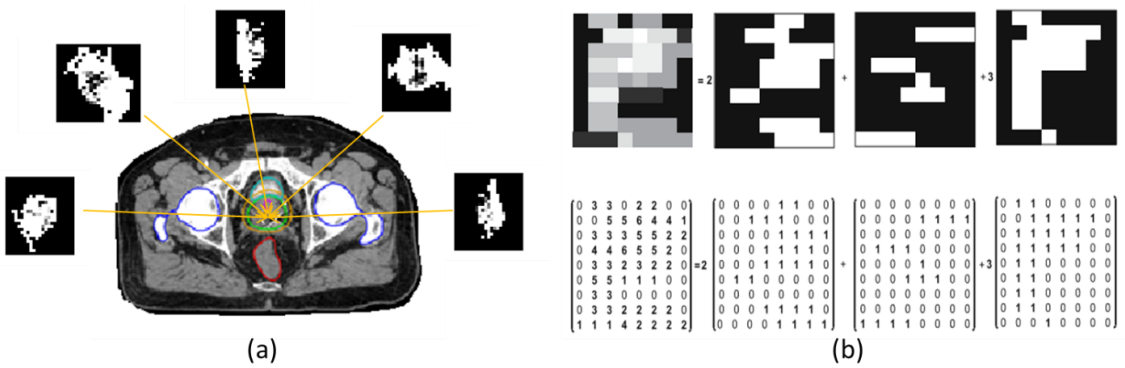

Figure 4.3. (a) Fluence map optimization with beamlet intensities represented in grayscale matrices. (b) Matrix C-1 decomposition in leaf sequencing. (adapted from *[83]*)

The core problem of treatment planning is to optimize the beam intensities so that a clinically satisfactory plan will be achieved (**fig. 4.3(a)**). To model beam intensities, the beam is discretized into beamlets or bixels whose size is determined by the MLC leaf configuration. Let d_{ijk} denote the dose received by voxel i from beamlet j of beam k, and $D = (d_{ijk})$ the dose matrix by indexing rows by i and columns by (j, k). Various optimization models have been developed to solve the FMO problem. Some models try to minimize the deviation of dose received by the target from the prescription dose and the overdose of organs at risk or normal tissues. The problem can be formulated as[84]

$$\min_{x \geq 0} \omega_{PTV} \|\mathrm{D_{PTV}x} - \mathrm{PrDose}\|_{\mathrm{p}} + \omega_{OAR} \|(\mathrm{D_{OAR}x} - \mathrm{OARUB})_+\|_{\mathrm{p}} + \omega_{NT} \|(\mathrm{D_{NT}x} - \mathrm{NTUB})_+\|_{\mathrm{p}} \quad (4.1.1)$$

where x is the beamlet intensity or beamlet weight and PrDose, OARUB, NTUB are prescription dose, dose upper bound on OARs and dose upper bound on normal tissues respectively. Here $(\cdot)_+ = max\{0, \cdot\}$ and $\|\cdot\|_{\mathrm{p}}$ is vector p-norm. ω_{PTV}, ω_{OAR}, and ω_{NT} are weight factors of each structures reflecting the importance of each objective. When $\mathrm{p} = 1$ or ∞, (4.1.1) becomes a linear program[85]. When $\mathrm{p} = 2$, (4.1.1) becomes one of the most prevalent weighted least squares model[86] that is often used in clinical planning in practice. Since both linear and quadratic program are convex, they can be solved to optimality rapidly. Another type of objective function is based on radiobiological effects produced by the dose distribution. Tumor control probability (TCP), which characterizes the response of target to radiation, is a commonly used in the radiobiological models. A Poisson-based TCP function[84] is

$$TCP = \prod_{i=1}^{m_T} exp\left(-(O/m_T)exp(-rd_i)\right) \quad (4.1.2)$$

where m_T is the number of equivolume voxels in the target, r is the radio sensitivity of the tumor clonogens, O is the total number of clonogens and d_i is the dose to voxel i. Based on TCP, Niemierko introduced the concept of tumor equivalent uniform dose (EUD), which assumes that two dose distributions are equivalent if they have the same tumor control probability[87]. The EUD is defined as

$$\mathrm{EUD} = -\frac{1}{\mathrm{a}}\ln\left(\frac{1}{\mathrm{m}}\sum_{\mathrm{i}=1}^{\mathrm{m}} \mathrm{e}^{-\mathrm{ad_i}}\right) \tag{4.1.3}$$

where m is the number of voxels and a is a structure dependent parameter that relates to the radiation response. The generalized equivalent uniform dose (gEUD), which is defined as

$$\mathrm{gEUD} = \left(\frac{1}{\mathrm{m}}\sum_{\mathrm{i}=1}^{\mathrm{m}} \mathrm{d_i}^{\mathrm{a}}\right)^{\frac{1}{a}} \tag{4.1.4}$$

extends the definition to normal tissues[88]. Moreover, Choi and Deasy proved that TCP is strictly concave and gEUD is convex when a ≥ 1 and concave when a < 1[89]. Many models developed their objective functions from TCP or gEUD[90, 91] and such biological-based optimization appears promising when compared to the least square minimization[92]. The constraints of FMO models often include non-negativity of beamlet intensity, upper and lower bound on the dose to tumor and OARs. One of the constraints appeared in RTOG is the dose volume constraint (DVC). These constraints differ from max/low point dose constraints in that they constrain the dose received by certain volume or percentage of volume of a structure. One approach is to divide the structure into high-dose and low-dose volume based on the distance to the beam isocenter and set different upper bounds for each volume separately[93]. Another approach, proposed by Romeijn et

al., use the concept of conditional value-at-risk (CVaR) to develop an approximation of DVCs[94]. CVaR models give a convex approximation to the standard optimization with dose volume constraints, which is proven to be non-convex[95], so that the optimization can be solved quickly. By introducing binary variables, dose volume constraints can be modeled as follows

$$\sum_{\mathrm{ij}} D_{p,ij} x_{ij} \leq \alpha\ \mathrm{PrDose}\ \mathrm{y}_p^{\alpha} + \mathrm{OARUBz_p}, p\ \in OAR \tag{4.1.5}$$

$$\sum_{p \in OAR} y_p^{\alpha} \geq \beta |OAR|, \tag{4.1.6}$$

$$\mathrm{y}_{\mathrm{p}}^{\alpha} + \mathrm{z_p} = 1, \mathrm{p} \in \mathrm{OAR} \tag{4.1.7}$$

where $\mathrm{y}_{\mathrm{p}}^{\alpha}$ and $\mathrm{z_p}$ are binary variables and x_{ij} is the intensity of beamlet j from beam i [96, 97]. OARUB is the dose upper bound on all OAR voxels and $|OAR|$ is the total number of OAR voxels. So (4.1.5) - (4.1.7) ensures that at least $100\beta\%$ of OAR voxels receive dose no greater than $100\alpha\%$ of prescription dose[96]. In addition, binary variables can also be used to represent beam selection in the combined FMO plus BAO model[98, 99]. For each beamlet j from beam i, let $\mathrm{y_i}$ be the binary variable indicating the on/off of a beam in B. Lee et al [96] formulate the beam selection, along with the fluence map optimization, as

$$\sum_{i \in B} y_i \leq \mathrm{B_{max}} \quad \text{and} \quad \mathrm{x_{ij}} \leq \mathrm{M_i y_i}, \quad \forall j \in B_i, i \in B \tag{4.1.8}$$

Here $\mathrm{B_{max}}$ is the maximum number of beam allowed to use and $\mathrm{M_i}$ is the maximum intensity allowed for each beamlet j from beam i. Mixed-integer programming (MIP) models provide high flexibility in modeling complex constraints and objectives and in turn gives superior results than continuous models. However, MIP models are in general much

more difficult to solve. With special branch-and-bound strategies and cuts implemented, good quality solutions can be obtained in a reasonable time[97]. From clinical perspective, there are often multiple criteria required for the delivery of radiation therapy[73]. Therefore, FMO problem is naturally a multi-objective optimization problem that involves the trade-off among different clinical objectives. A solution is called pareto-optimal if we cannot improve any treatment objective without deteriorating other objectives. Models introduced so far use *weighted sum* of different objectives as a single objective function, which is a widely used strategy called scalarization. Another approach, called lexicographic optimization (LO) (or *pre-emptive programming*), optimizes each objective sequentially based on the clinical priority of objectives. Moreover, higher priority objective functions, which have been optimized, will be constrained to their achieved values when optimizing lower priority objectives[100, 101]. Scalarization and lexicographic optimization are mathematically equivalent and can be switched between each other through Lagrangian multipliers[102].

Once the intensity profile of each selected beam is found, leaf sequencing (LS) algorithms are used to create MLC deliverable shapes, which is called segment or aperture, from the optimized fluence map. The fluence map obtained after FMO can be seen as a real nonnegative matrix I. Very often I will first be "smoothed" so that entries in I will have values at discrete intensity levels[103, 104]. Smoothing procedure makes the realization of the fluence map easier both mathematically and practically. Now the LS problem is to find a set of binary matrices K such that

$$I = \sum_{k \in K} \alpha_k Y^k \tag{4.1.9}$$

where $Y^k \in B^{m\times n}$ is called shape matrix with m rows representing the leaf pairs of MLC and n columns representing the number of beamlets for each leaf pair. $\alpha_k \geq 0$ is called the monitor unit (MU) of the aperture k. As each row represents the opening of a leaf pair, the shape matrix Y^k must possess the consecutive-ones (C1) property, which says that entries with value 1 in each row should be consecutive (**fig. 4.3(b)**). By (1.2.9), one can either minimize the total beam-on-time (BOT), $\mathrm{DT}(\alpha) \coloneqq \sum_{k\in K} \alpha_k$ or minimize the total number of apertures, $\mathrm{D}C(\alpha) \coloneqq |\{\alpha_\mathrm{k}: \alpha_\mathrm{k} > 0\}|$. Assume the average time needed for MLC to change aperture shape is τ, then one can also minimize the total treatment time $T\mathrm{T}(\alpha) \coloneqq \mathrm{DT}(\alpha) + \tau\mathrm{DC}(\alpha)$. DT problem can be solved by the sweep algorithm proposed by Bortfeld et al.[105]. The optimality of this algorithm is proven by transforming it into a network flow problem and can be solved in polynomial time[106]. In practice, more complex hardware constraints other than C1 constraint are needed based on the type of MLC. Interleaf motion constraints require that the opening of two neighboring rows should at least overlap with one column. Leaf width constraints requires that the opening of each row should be at least a constant value $\delta > 0$. Since most MLC systems use tongue-and-groove joints between adjacent leaf pairs, the tongue leaves will cause smaller radiation than groove leaves, which makes (4.1.9) not accurate in real delivery. Therefore, tongue-and-groove constraints is required to ensure that the opening of a column in the shape matrix be at least two rows long. Baatar et al. proved that DT problem with interleaf and width constraint can be solved in $\mathrm{O}(\mathrm{nm}^2)$ time[107]. Siochi developed a rod-pushing algorithm that solves the DT with tongue-and-groove correction[108]. Compared to DT problem, DC problem is proven to be NP-hard[107]. Some heuristic methods have been developed to solve this problem[109-111].

There are some shortcomings of the traditional two-step optimization framework, i.e. doing FMO and LS sequentially. First, as leaf sequencing often requires smoothing of the fluence map, there is often degradation of plan quality between FMO and LS solutions. Moreover, lots of apertures will be generated if the fluence map is complex, which will lead to long treatment time. Direct aperture optimization (DAO) method, which combines FMO and LS together, has been developed to address these issues. The solution of DAO is already deliverable and the total treatment time can be directly optimized in the DAO model. DAO directly optimized the shapes and intensities of apertures at the same time. However, the difficulties of DAO are that the aperture shape generation and optimization. And there are mainly three different methods to achieve it. The first type of models optimizes aperture shapes by performing small leaf position changes using heuristic algorithms. An initial set of apertures are predetermined to the beam's eye view (BEV) of the target. Shepard et al. developed a method to update the leaf positions using simulated annealing approach so that the objective value is improved[112]. In their method, the total number of apertures is fixed before the optimization. The second type of models, which is similar to the first one, considers the leaf positions as optimization variables and optimize them using gradient descent method. Both the objective function and its gradient are approximated as functions of leaf positions[113]. Such leaf refinement methods have been used in some commercial treatment planning systems(Pinnacle TPS, Philips Radiation Oncology Systems, Fitchburg, WI[114]). The last type of models adds apertures iteratively using column generation method. New apertures, which are promising to improve the objective value, are created by solving a pricing problem and added to the master problem to re-optimize the intensities[115, 116].

In Section 4.2, we summarize the contribution of treatment planning in this thesis. We first solve the problem of isocenter selection for radiation beams. This problem, which is rarely discussed in literature, is very important for improving plan quality of radiotherapy. Then we propose a multi-objective direct aperture optimization model that includes most commonly used clinical planning goals. The optimization is solved in a pre-emptive way such that treatment goals are optimized based on the priority that is determined by clinicians and/or that they are most suitable for each individual patient. Coupled with the optimization model, a novel heuristic column generation approach is designed to create new aperture shapes that can be added to improve the objective values. This column generation approach, which does not rely on beamlet dose calculation, efficiently produces large number of promising apertures so that the master multi-objective optimization problem can generate feasible deliverable plans in a short period of time. Moreover, we further integrate the beam selection into this direct aperture optimization framework. *Hence, this work presents the first treatment planning model that optimizes beam angle, aperture shape and aperture intensity in a single procedure*. We test the model for 15 real patient cases including 5 prostate, 5 lung and 5 intracranial cases. For all cases, our model can efficiently generate clinically acceptable and readily deliverable plans in a reasonable time.

4.2 Methods to advance treatment planning and applications to Cyberknife

The content of this section is based on three submitted manuscripts[12-14]

4.2.1 Isocenter selection

Single-isocenter plans are often used in radiation therapy treatment. Plans with multiple isocenters increase the complexity of the treatment and often use more MUs to deliver[96]. However, increasing the number of isocenters can greatly improve dose conformity of the target, especially for treating non-spherical, irregular, or large tumors that cannot be covered by the collimator[117]. Multiple-isocenter plans can be achieved by optimizing the location of isocenters[98]. We propose a general-purpose mathematical model for the optimization of isocenter locations.

Although the exact dose distribution produced by a single isocenter depends on the beam angle selection, it is nearly spherical and homogeneous around the isocenter for a LINAC system and can be approximated by a set of ellipsoids[118]. Since the dose fall-off is a function of distance from the isocenter, we can expect a highly conformal plan by choosing a set of ellipsoids that cover all target points and have minimum excess volume. Generally, this problem can be stated as an optimization problem. Suppose there is a set of points in $V \subset \mathbb{R}^3$. Given an integer $N_c \geq 1$, find N_c ellipsoids $E_1, \dots E_{N_c}$ such that $V \subset \cup_{i=1}^{N_c} E_i$ and the volume $Vol(\cup_{i=1}^{N_c} E_i)$ is minimized. Let $E_i = \{(x,y,z) \in \mathbb{R}^3 | \frac{(x-\alpha_i)^2}{{a_i}^2} + \frac{(y-\beta_i)^2}{{b_i}^2} + \frac{(z-\gamma_i)^2}{{c_i}^2} \leq 1\}$, then the problem can be formulated as

$$\text{(ISO)} \qquad \text{Min} \quad Vol(\cup_{i=1}^{N_c} E_i)$$

$$\text{s.t.} \quad \frac{(x_v-\alpha_i)^2}{{a_i}^2} + \frac{(y_v-\beta_i)^2}{{b_i}^2} + \frac{(z_v-\gamma_i)^2}{{c_i}^2} \leq 1 + M \cdot y_{vi}, \qquad \forall v \in V$$

$$\sum_{i=1}^{N_c} y_{vi} = 1, \qquad \forall v \in V$$

$$\alpha_i, \beta_i, \gamma_i, a_i, b_i, c_i \geq 0, \text{and } y_{vi} \in \{0,1\}, \qquad \forall \text{i}, \ \forall v \in V$$

When $N_c = 1$, (ISO) becomes the classic minimum enclosing disk problem[119]. In the setting of radiation therapy, the optimal solution of the center of ellipsoids $s_i^* = (a_i^*, b_i^*, c_i^*)$ will be chosen as the isocenter. Mathematically, solving (ISO) is not easy. First, computing the volume of a union of ellipsoids/balls is complicated[120]. Second, even though we can find an explicit form to represent the volume of the union of ellipsoids, it is a nonlinear mixed-integer program and computationally hard to solve. Lee et al designed an integer programming approach to optimize the isocenter selection. The algorithm optimizes over all potential voxels and uses the quality of the plan outcome as objective functions to drive the selection and location of the isocenters[96].

In this work, we develop a heuristic approach to solve (ISO) to obtain a solution that results in highly conformal plans. Based on our experiment, we observed that it is not necessary to obtain an optimal solution as the isocenters for most of the cases. A near-optimal solution can already greatly improve the dose conformity as we can choose wisely the beam angles and optimize the MLC shape.

In practice, our first task is to determine N_c, the number of isocenters best suited for the tumor, before we can solve (ISO). We assume that the dose distribution of a single isocenter is spherical, we can obtain good dose conformity if the target also has spherical shape. Therefore, we can identify the spherical shaped parts of the target and the number of isocenters should match the number of such parts. We know that the target is discretized into voxels in CT space. We define a *z (x or y)-direction-slice* as the plane with all the voxels having the same z (x or y) value. If the target is a ball, the number of voxels in any direction-slices will gradually increase from zero to a maximum value and then decrease to zero again, which also means that the derivative of the curve will change from positive

to negative. In **figure 4.4**, we showed a schwannoma tumor which is tiny but irregular. For each of the anatomical direction, a voxel vs. slice curve is fitted. When a target is irregular, there must exist a direction (sagittal in this case) where there are multiple local maxima in the voxel-slice curve. Each peak of the curve represents a ball shaped part of the target. Therefore, the number of ball shaped parts in that direction is determined by the number of peaks p_x ($p_y$or p_z) in the curve. Then the maximum value $p^* = max\{p_x, p_y, p_z\}$ will be used as the number of isocenters. For some highly irregular shaped targets, p^* can be large. To balance plan complexity and dose conformity, we set the maximum number of isocenters to be 3. So $N_c = \max\{p^*, 3\}$. Among the 15 cases we tested, all the prostate tumors are ball shaped and the heuristic algorithm returns $N_c = 1$. Lung tumors are often big and irregular, in 4 out of 5 cases, N_c is greater than 1. For the intracranial cases, the tumors are tiny yet irregular, 3 out of 5 cases have N_c greater than 1. (**fig. 4.5**)

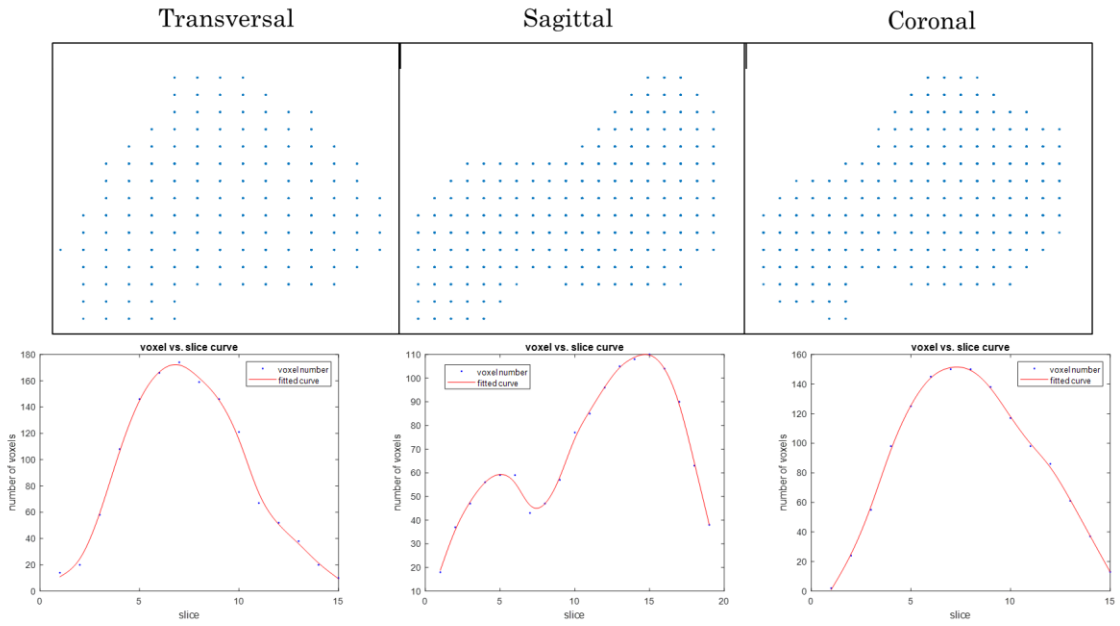

Figure 4.4. A schwannoma tumor case. Top: The shape of the tumor is plotted in transversal, sagittal and coronal view respectively. Each column of dots in the figure represents a z (x or y)-direction slice. Bottom: the voxel vs. slice curve fitted

Once N_c is determined, we need to determine the location of isocenters. When $N_c = 1$, a single-isocenter plan is preferred and the center of mass of the target will be used as the isocenter. When $N_c = 2$ or 3, however, the location of the isocenters in (ISO) can be potentially anywhere in the space, which makes it hard to solve. A possible solution is using the classic K-means clustering algorithm[121] to cluster target voxels into N_c clusters. However, the result of K-means algorithm is not satisfactory as it cannot capture the highly irregular shape of the target. Instead, we identify a set of good candidate locations L and the isocenters will be chosen from it by solving an optimization problem.

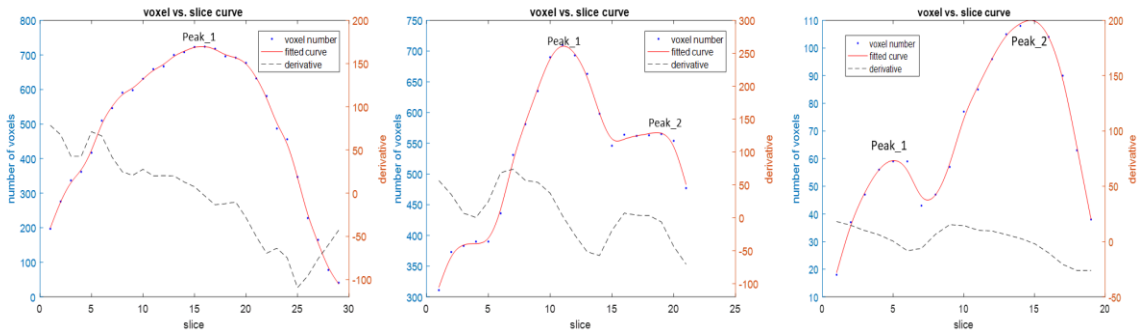

Figure 4.5. From left to right, prostate tumor, lung tumor, schwannoma tumor; number of target voxels in each slice (blue dot), fitted voxel vs. slice curve (solid red) and its derivative (dotted black).

Suppose $p^* = p_x$, then for each x-direction-slice, the center of mass of target voxels in each x-direction-slice is calculated and included in L. Define S as the set of surface points of the target and d_{ij} as the distance between a location $i \in L$ and a point $j \in S$. Intuitively, a location will be chosen if the average distance between all surface points to that location is small. Therefore, we formulated an integer program to find such locations so that the sum of distances between each surface point to the selected locations is minimized.

$$\text{(ISOFLP)} \quad \text{Min} \quad \sum_{i\in L}\sum_{j\in S} d_{ij}x_{ij}$$

$$\text{s.t.} \quad \sum_{i\in L} x_{ij} = 1, \qquad \forall j \in S$$

$$x_{ij} \le y_i, \qquad \forall i \in L,\ \forall j \in S$$

$$\sum_{i\in L} y_i \le N_c, \qquad \forall i \in L$$

$$x_{ij}, y_i \in \{0,1\} \qquad \forall i \in L,\ \forall j \in S$$

This problem is a facility location problem with no cost of opening facilities but a capacity on the number of facilities opened[122]. It is an integer program that is often used to solve the placement of facilities to best meet the demand of customers. Though integer programs are generally computationally difficult to solve, (ISOFLP) usually takes less than a minute to get optimal solution for the cases we tested. The solution of (ISOFLP) is used as the isocenters for our plan(**fig. 4.6**).

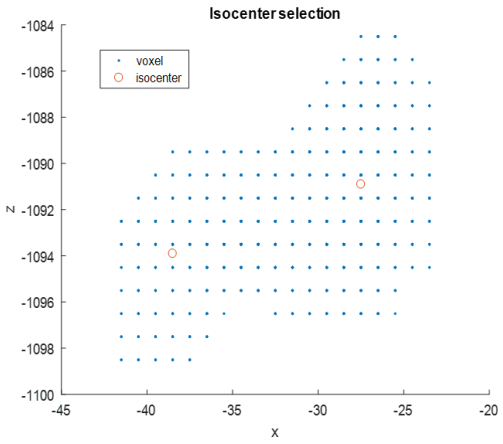

Figure 4.6. Set of potential candidate locations (blue dots); and selection of isocenter locations by solving ISOFLP with $N_c = 2$ (red circle).

4.2.2 Multi-objective direct aperture optimization

The main goal of radiation therapy is to deliver adequate dose to the tumor site while sparing as much as possible the normal tissues around tumor. The quality of a plan is evaluated by several criteria including biological functions (TCP, EUD, gEUD, etc.) and dosimetric functions (mean dose, homogeneity, etc.). We list below the criteria considered in this work and the corresponding definition.

- Coverage: the percentage of target volume receiving dose higher than prescription dose
- Max dose: the maximum dose allowed in tumor or OARs
- Mean dose: the average dose received in tumor or OARs
- Dose volume histogram (DVH): a frequency distribution of dose values within tumor or OARs
- Conformity: The conformity index (CI) is defined as ratio of volume enclosed by prescription isodose surface to the target volume enclosed by the same surface. It is a measure of how well the prescription isodose surface conforms to the target. The ideal value is 1.
- Homogeneity: The homogeneity index (HI) is defined as $\mathrm{HI} = \frac{\mathrm{D_{max}}}{\mathrm{D_{min}}}$, where $\mathrm{D_{max}}$ is the maximum dose received by the target ("max dose") and $\mathrm{D_{min}}$ is the minimum dose received by the target ("min dose"). It is a measure of uniformity of the dose distribution in target and should close to 1.
- Total MU: total number of monitor units which directly relates to the treatment time.

In practice, different patients have different clinical conditions. Radiation therapy, which is a multi-objective optimization problem, can be personalized to favor patient's own characteristics. For some patients, the best plan could be one which has full coverage of tumor without regard to the normal tissue receiving high dose. For other patients, whose critical structures are close to the tumor, doctors may prefer a plan with a slight underdose to the tumor while ensuring low dose to critical structures. Therefore, the optimization model should provide high flexibility for modification so that the "best" possible plan can be obtained. Compared to the traditional scalarization method, the lexicographic optimization method (LO) does not need the weighting factors of the objectives and doctors can directly place the optimization steps in order of clinical priority. Moreover, the solution of each step is guaranteed feasible and the objective of each step can only be compromised by a slight relaxation in later steps. Doctors can easily identify the trade-offs between different objectives and balance on conflicting goals[123].

In this thesis, we proposed a lexicographic linear direct aperture optimization model (LLDAO) using column generation algorithm. All objectives and constraints are linear in LLDAO and different objectives enter the optimization sequentially in order of clinical priority. At each step, the objective function is optimized using apertures generated until last step. New apertures will be generated using column generation when the current objective value is not clinically acceptable. This procedure will be fully automatic once the order of objectives is determined. Moreover, the final solution of LLDAO is clinically deliverable as it uses apertures in the optimization. The complete LLDAO procedure is illustrated in **fig. 4.7**.

The optimization will start with an initial set of apertures which are generated from the projection of PTV voxels of each beam angle. At each step, one of the objectives will be optimized with PTV and OAR dose upper bound and with objective functions from previous steps constrained. For dose-volume constraints, we adopted the CVaR constraints first introduced in [94]. Instead of bounding the minimum or maximum of a tail of the DVH, CVaR constraints bound the mean value of the tails. Let A denote the set of all candidate apertures, $D_{p,a}$ be the dose coefficient of aperture a to voxel p and x_a be the monitor unit of each aperture a. Then, the lower α-CVaR of PTV dose distribution is defined as

$$LCVaR_{PTV}(\alpha) = PTVQ^{\alpha} - \frac{1}{(1-\alpha)|PTV|}\sum_{P\in PTV} max\left(0, PTVQ^{\alpha} - \sum_{a\in A} D_{p,a}x_a\right)$$

where $PTVQ^{\alpha}$ is the maximum dose received by at least $100(1-\alpha)\%$ of PTV voxels. So (1-α)% PTV coverage constraint can be formulated as

$$LCVaR_{PTV}(\alpha) = PTVQ^{\alpha} - \frac{1}{(1-\alpha)|PTV|}\sum_{P\in PTV} max\left(0, PTVQ^{\alpha} - \sum_{a\in A} D_{p,a}x_a\right) \geq L^{\alpha}$$

and we can transform it into a set of linear constraints

$$PTVQ^{\alpha} - \frac{1}{(1-\alpha)|PTV|}\sum_{P\in PTV} tPTVQ_p{}^{\alpha} \geq L^{\alpha}$$

$$tPTVQ_p{}^{\alpha} \geq PTVQ^{\alpha} - \sum_{a\in A} D_{p,a}x_a \ , p \in PTV$$

$$tPTVQ_p{}^{\alpha} \geq 0 \ , p \in PTV$$

Such linear transformation will keep the optimization in LLDAO as a linear program without introducing nonlinear or integer component. To optimize conformity and achieve steep gradient around PTV, we introduce the shell structures around PTV and minimize the dose to them[96, 98]. The voxels in a shell structure locate in a certain distance to the surface of PTV. For example, SHELL_2MM is defined as the voxels 2mm away from PTV. The shell structures are treated as an OAR and optimizing the dose to it is proven to be effective to reduce conformity index[98]. In our work, we use SHELL_2MM and SHELL_4MM to optimize conformity index and SHELL_20MM to control low dose spillage.

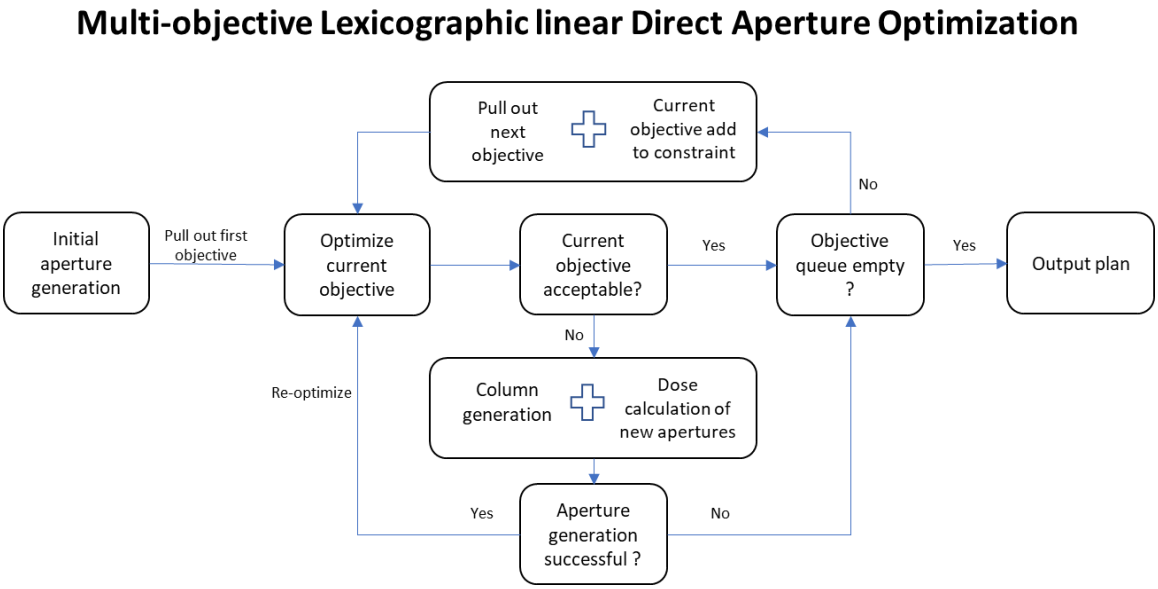

Figure 4.7. LLDAO process map. New apertures will be generated using column generation algorithm. Then the dose is calculated and added to the model to re-optimize. The process will go to next step when the current objective value is clinical acceptable or no apertures can be generated to further improve the objective.

Below we will show an efficient process of LLDAO that includes commonly used objectives in radiation therapy.

Step 1 (PTV min feasibility):

$$\text{Min} \quad \sum_{p\in PTV} Slack_p \tag{4.2.1}$$

$$\text{s.t.} \quad \sum_{a\in A} D_{p,a}x_a + Slack_p \geq PTVlb, \text{ p} \in \text{PTV} \tag{4.2.2}$$

$$\sum_{a\in A} D_{p,a}x_a \leq PTVub \ , \text{ p} \in \text{PTV} \tag{4.2.3}$$

$$\sum_{a\in A} D_{p,a}x_a \leq OARub \ , \text{ p} \in \text{OAR} \tag{4.2.4}$$

$$0 \leq x_a \leq MaxMU \ , a \in A \tag{4.2.5}$$

$$Slack_p \geq 0 \ , \text{ p} \in \text{PTV} \tag{4.2.6}$$

where $Slack_p$ is the underdose value of voxel p. $PTVlb, PTVub$ are the lower and upper dose limit on PTV voxels and $OARub$ is the upper dose limit on OAR voxels. $MaxMU$ is the maximum MU allowed for an aperture. When $\sum_{p\in PTV} Slack_p = 0$, there is no underdose for all PTV voxels. However, the initial aperture set will not guarantee the optimal objective value to be zero if constrained by (4.2.2)-(4.2.4). Therefore, new apertures should be generated until $\sum_{p\in PTV} Slack_p$ is zero.

Step 2 (PTV (1-α)% coverage):

$$\text{Max} \quad PTVQ^{\alpha} - \frac{1}{(1-\alpha)|PTV|}\sum_{P\in PTV} tPTVQ_p{}^{\alpha} \tag{4.2.7}$$

s.t. $(4.2.3) - (4.2.5)$ from previous steps

$$\sum_{a\in A} D_{p,a}x_a \geq PTVlb, \text{ p} \in \text{PTV} \quad (4.2.8)$$

$$tPTVQ_p{}^{\alpha} \geq PTVQ^{\alpha} - \sum_{a\in A} D_{p,a}x_a, \qquad \text{p} \in \text{PTV} \quad (4.2.9)$$

$$tPTVQ_p{}^{\alpha} \geq 0, \text{ p} \in \text{PTV} \quad (4.2.10)$$

$$PTVQ^{\alpha} \geq 0, \text{ p} \in \text{PTV} \quad (4.2.11)$$

In step 2, we directly maximize the lower α- CVaR of the PTV to achieve adequate dose coverage of PTV. From (4.2.7), we see that the lower α- CVaR is a lower bound of $PTVQ^{\alpha}$. So (1-α)% PTV coverage will be guaranteed if (4.2.7) is greater than the prescription dose. Again, new apertures will be generated when PTV coverage is not satisfied.

Step 3 (Optimize Conformity):

Min $$ShellQ^{\alpha} + \frac{1}{(1-\alpha)|SHELL|}\sum_{P\in SHELL} tShellQ_p{}^{\alpha} \quad (4.2.12)$$

s.t. $(4.2.3) - (4.2.5), (4.2.8) - (4.2.11)$ from previous steps

$$PTVQ^{\alpha} - \frac{1}{(1-\alpha)|PTV|}\sum_{P\in PTV} tPTVQ_p{}^{\alpha} \geq PTVDose_{\alpha} \quad (4.2.13)$$

$$tShellQ_p{}^{\alpha} \geq \sum_{a\in A} D_{p,a}x_a - ShellQ^{\alpha}, \text{ p} \in \text{SHELL} \quad (4.2.14)$$

$$tShellQ_p{}^{\alpha} \geq 0, \text{ p} \in \text{SHELL} \quad (4.2.15)$$

Here, $PTVDose_\alpha$ is the optimal objective value from step 2 with a small relaxation. For most cases we tested, plans from step 2 will satisfy PTV coverage and (4.2.7) is greater than prescription dose. So $PTVDose_\alpha$ is set to be the prescription dose. Although the shell structure is treated as an OAR in the optimization, the big difference between shell and OAR is that we cannot set dose limit on shell structures as it depends on tumor characteristics and the value of prescription dose. We can minimize either the total dose or the max dose to shell voxels to control dose spillage. Here we propose another perspective to the optimization of conformity. Suppose we want to get a plan with conformity index less than a reference value of 1.2. By the definition of conformity index, we know that at most $0.2|PTV|$ shell voxels can have dose larger than the prescription dose. This can be formulated as a dose-volume constraint on the shell structure. At most $\beta\% = \frac{20*|PTV|}{|SHELL|}\%$ of shell voxels can have dose larger than prescription dose. Although this is only a necessary condition for $\mathrm{CI} \leq 1.2$, empirically, it is very effective in reducing CI. Compared to minimizing total dose, CVaR formulation targets voxels with large dose so that CI can be reduced much faster.

Step 4 (minimize OAR mean dose):

$$\text{Min} \qquad \sum_{P\in OAR} d_p \tag{4.2.16}$$

s.t. $(4.2.3)-(4.2.5), (4.2.8)-(4.2.11), (4.2.13)-(4.2.15)$ from previous steps

$$ShellQ^\alpha + \frac{1}{(1-\alpha)|SHELL|}\sum_{P\in SHELL} tShellQ_p{}^\alpha \leq Shellub \tag{4.2.17}$$

$$\sum_{a\in A} D_{p,a}x_a = d_p, \text{ p} \in \text{OAR} \quad (4.2.18)$$

Here, $Shellub$ is the optimal objective value in step 3 with a small relaxation. One of the advantages of optimizing CI before OAR is that the conformal plan from step 3 is very likely to have low dose in the surrounding OARs. For OARs that need further reduction of dose, they are added in step 4 sequentially based on clinical priority and their mean dose is minimized. In our analysis, OARs are added from the closest to the farthest to the surface of PTV.

Step 5 (Reduce Total MU):

$$\text{Min} \quad \sum_{a\in A} x_a \quad (4.2.19)$$

$$\text{s.t.} \quad (4.2.3) - (4.2.5), (4.2.8) - (4.2.11), (4.2.13) - (4.2.15),$$

$$(4.2.17) - (4.2.18) \text{ from previous steps}$$

$$\sum_{P\in OAR} d_p \leq OAR\_Total\_Dose, \text{ p} \in \text{OAR} \quad (4.2.20)$$

Again, OAR_Total_Dose is the optimal objective value in step 4 with a relaxation. Step 5 addresses the trade-off between plan quality and plan complexity. Plans with longer treatment time are subject to more leakage radiation, which increases the total body integral dose. For all LINAC systems, the treatment time of a plan relates to the number of beams, apertures and total MU. We will discuss the beam selection in section 4.2.4 and focus on total MU here. Though the complexity of a plan depends on the complexity of the underlying planning objective[124], large total MU is sometimes unnecessary and can be

significantly reduced[125]. The traditional two-step optimization method often observes increase of total MU after leaf sequencing and is difficult to control during the optimization. Direct aperture method, by optimizing step 5, can minimize directly the total MU to generate highly efficient plans. The problem of direct aperture method, which is rarely mentioned in the literature, is the difficulty in keeping the aperture MU from very small values. Since direct aperture models are often solved by convex optimization method constrained only on the non-negativity of aperture MU, the optimal solution often has some apertures with very small MU (e.g. less than 10). Apertures with small MU are hard to deliver in practice and are subject to large errors. But simply eliminating these apertures will cause underdose to the target. Therefore, a strict positive lower bound on MU of every used aperture should be included. To solve this issue, we proposed a mixed-integer program based on step 5 to force the MU of all selected apertures greater than a minimum value.

Step 5' (Reduce Total MU + MinMU lower bound):

$$\text{Min} \quad \sum_{a\in A} x_a \tag{4.2.21}$$

$$\text{s.t.} \quad (4.2.3)-(4.2.5), (4.2.8)-(4.2.11), (4.2.13)-(4.2.15),$$

$$(4.2.17)\ -\ (4.2.18), (4.2.20) \text{ from previous steps}$$

$$x_a \le MaxMU\ y_a\ ,\ a \in A \tag{4.2.22}$$

$$x_a \ge MinMU\ y_a\ ,\ a \in A \tag{4.2.23}$$

$$y_a \; binary, a \in A \tag{4.2.24}$$

where y_a is a binary variable and equals 1 if aperture a is selected. $MinMU$ is the minimum MU allowed for an aperture. Step 5' is a mix-integer program and column generation cannot be applied. So total MU will first be minimized to a satisfactory value in step 5 and step 5' serves as a filtering step right after that.

In addition to these 5 objectives, other linear objectives can also be added into LLDAO. For example, we can minimize the max dose to OARs, minimize homogeneity index or minimize maximum MU allowed for an aperture.

4.2.3 Column generation

To successfully implement the LLDAO model, we developed an efficient column generation algorithm to create new apertures. All column generation algorithms developed in the past need to solve a pricing problem involving the dose coefficient $D_{p,a}$, which is the dose per unit monitor to voxel p from aperture a. It is assumed that the dose of an aperture equals the sum of dose of beamlets inside that aperture, i.e. $D_{p,a} = \sum_{i \in a} D_{p,i}$, where $D_{p,i}$ is the dose coefficient of beamlet i to voxel p. However, this assumption is generally not true in real practice especially when an aperture has irregular shape. Some methods have been proposed to address this issue. For example, a correction factor γ_a is used for each aperture so that $D_{p,a} = \gamma_a \sum_{i \in a} D_{p,i}$ [115]. Others decompose $D_{p,a}$ into 2 parts, $D_{p,a} = \sum_{i \in a} D_{p,i} + \varepsilon \sum_{i \notin a} D_{p,i}$, where ε is the transmission factor of the dose from the beamlets that are blocked by a [126]. However, based on our experiment, these

correction methods are still not satisfiable to compensate for the discrepancy between beamlet solution and aperture solution. For many deliverable plans we tested, huge underdose and conformity/homogeneity degradation are observed by just changing from beamlet-based dose calculation to aperture-based dose calculation (**fig. 4.8**). Such degradation cannot be removed by multiplying a constant scaling factor. We believe the discrepancy comes from the dose calculation algorithm. The dose scattering effect of a beamlet, when it is calculated for an aperture, is smaller than the effect which is calculated when only this beamlet open. This explains why the aperture-based dose is smaller than beamlet-based dose and why the degradation ratio increases with the increase of beamlet-based dose for OAR voxels (**fig. 4.9**).

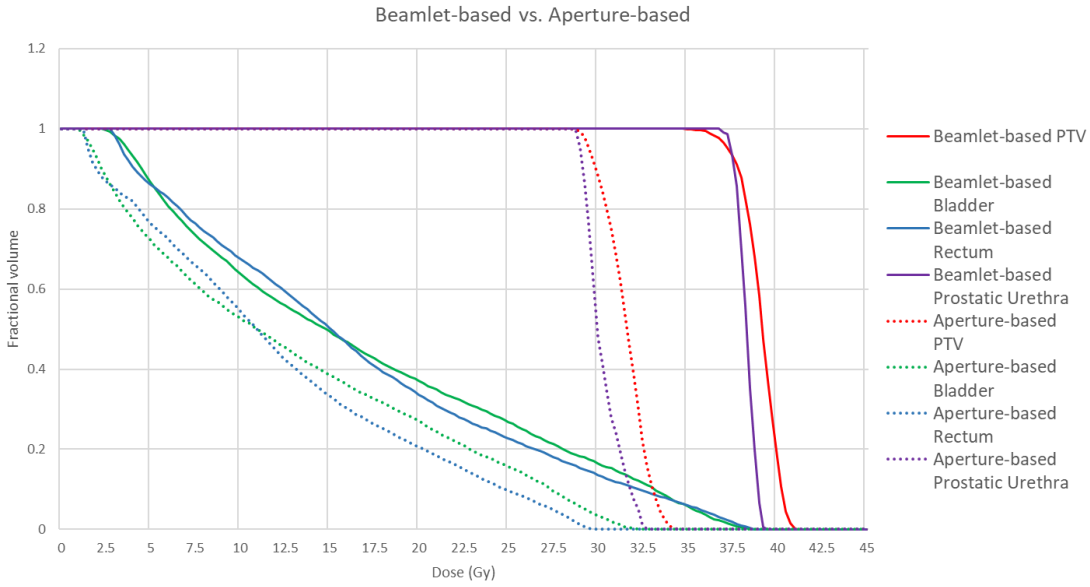

Figure 4.8. A prostate case solved by traditional two-step method. After leaf sequencing, dose is calculated using 2 different methods. Beamlet-based (solid): the dose of an aperture is calculated as the summation of each beamlet dose; Aperture-based (dotted): the dose of an aperture is directly calculated using pencil beam algorithm. The comparison of DVH shows huge underdose of the aperture-based dose calculation method.

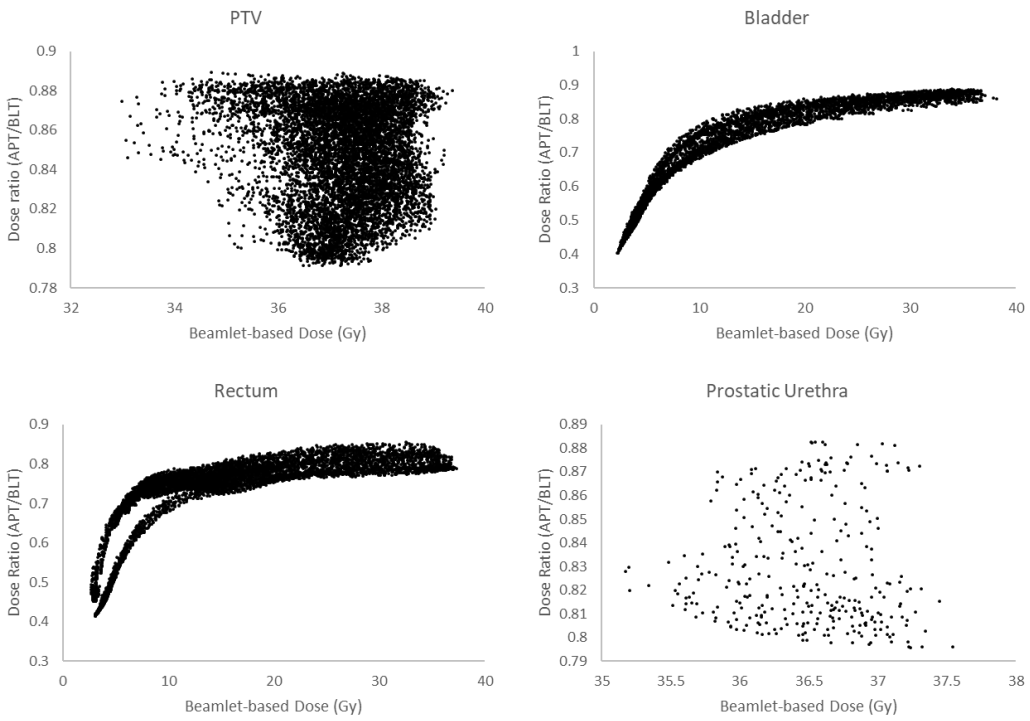

Figure 4.9. Dose degradation of aperture-based dose calculation of 4 structures. For each voxel, the ratio of aperture-based dose(APT) and beamlet-based dose(BLT) is calculated.

Therefore, using the "true" aperture dose in treatment planning is very important to guarantee the quality of the optimized plan and reduce error in QA process. However, this create a big trouble for solving the pricing problem to generate new apertures. No matter what master problem we use, the pricing problem must use the dose coefficient $D_{p,a}$ of the new aperture a, which becomes unknown without using beamlet dose (i.e. $D_{p,a} = \sum_{i \in a} D_{p,i}$). To solve this issue, we proposed a novel heuristic pricing problem (corresponding to LLDAO master problem) that generate new apertures efficiently. This algorithm

1) Does not need any dose information ($D_{p,a}$ or $D_{p,i}$) when generating apertures;
2) Generates apertures efficiently (in polynomial time) with common MLC constraints;

3) Creates multiple apertures in a single run to accelerate the optimization;

4) Saves time on dose calculation. No need to calculate beamlet dose.

In this column generation algorithm, the master problem can be any of the optimization problems in the LLDAO model. However, the corresponding pricing problems, which is to find new apertures, are of the same form. Precisely, the coefficient of variable x_a in the constraints is $D_{p,a}$. Then the reduced cost of an aperture a is given by

$$R(a) = c_a - \sum_{p\in PTV}(\lambda_p^1 + \lambda_p^2 + \lambda_p^3)D_{p,a} - \sum_{p\in Shell}\pi_p D_{p,a} - \sum_{p\in OAR}(\mu_p + \tau_p)D_{p,a} \quad (4.3.1)$$

where $\lambda_p^1 \geq 0$, $\lambda_p^2 \geq 0$, $\lambda_p^3 \leq 0$ are the dual variables corresponding to PTV lower bound constraints (4.2.8), PTV $(1-\alpha)\%$ coverage constraints (4.2.9) and PTV upper bound constraints (4.2.3). $\pi_p \leq 0$ are the dual variables corresponding to Shell CVaR constraints (4.2.14) and $\mu_p \leq 0$, $\tau_p \leq 0$ are the dual variables corresponding to OAR upper bound constraints (4.2.4), OAR dose constraints (4.2.18). c_a is the cost coefficient of aperture a in the objective function. Since the maximization of PTV (1-α)% coverage can be changed to a minimization problem by negating the sign of the objective function, all linear programs in LLDAO are minimization problems. So the pricing problem is to find apertures such that $R(a) < 0$, and can be written as

$$F^a := \sum_{p\in PTV}(\lambda_p^1 + \lambda_p^2 + \lambda_p^3)D_{p,a} + \sum_{p\in Shell}\pi_p D_{p,a} + \sum_{p\in OAR}(\mu_p + \tau_p)D_{p,a} > c_a \quad (4.3.2)$$

This inequality can be interpreted that an aperture can be priced out if the total dose gain in PTV voxels outperforms the total dose loss of Shell and OAR voxels by c_a. Therefore, adding this aperture will either increase PTV dose without violating OAR/Shell dose constraints or keep PTV dose level but reduce OAR/Shell dose.

Like other column generation algorithms, we solve the pricing problem for each beam separately. Each beam is uniquely defined by its position, up vector and target point (isocenter) and is discretized into beamlets with certain resolution. Since each voxel is uniquely projected to a beamlet i of beam b, we can re-arrange $F^a = \sum_{i \in b} {F_i}^a$, where

$${F_i}^a := \sum_{p \in PTV \cap \{i\}} (\lambda_p^1 + \lambda_p^2 + \lambda_p^3) D_{p,a} + \sum_{p \in Shell \cap \{i\}} \pi_p D_{p,a} + \sum_{p \in OAR \cap \{i\}} (\mu_p + \tau_p) D_{p,a} \quad (4.3.3)$$

Here $PTV \cap \{i\}$, $Shell \cap \{i\}$ or $OAR \cap \{i\}$ are the set of PTV, Shell or OAR voxels projected to beamlet i in the MLC plane. Recall that $D_{p,a}$ is the dose deposited by aperture a to voxel p, which is not the beamlet dose $D_{p,i}$. As a result, the size of beamlets can be different in different parts of the beam to fully take advantage of the flexibility of MLC. For example, higher resolution can be applied to the area where PTV voxels are projected and lower resolution to the other area. Though the exact value of $D_{p,a}$ is unknown currently, it has the following properties: 1) $D_{p,a} > 0$ for all voxels p and 2) $D_{p_1,a} \geq D_{p_2,a}$ if the distance between p_1 and beam is shorter than the distance between p_2 and beam[127]. In other word, $D_{p,a}$ is a non-negative function and attenuate with the distance. Define $DualSum_i = \sum_{p \in V \cap \{i\}} (\lambda_p^1 + \lambda_p^2 + \lambda_p^3 + \pi_p + \mu_p + \tau_p)$ as the sum of dual variables of the voxels in V that are projected to beamlet i. We can classify the beamlets into 5 groups:

- G1: Only PTV voxels are projected onto beamlet i and $\lambda_p^3 = 0, \forall p \in PTV \cap \{i\}$. Then ${F_i}^a = \sum_{p \in PTV \cap \{i\}} (\lambda_p^1 + \lambda_p^2) D_{p,a} \geq 0 \Leftrightarrow DualSum_i = \sum_{p \in PTV \cap \{i\}} (\lambda_p^1 + \lambda_p^2) \geq 0$ by property 1 of $D_{p,a}$.

- G2: Both PTV voxels and OAR/Shell voxels are projected onto beamlet i and $\lambda_p^3 = 0, \forall p \in PTV \cap \{i\}$. All OAR/Shell voxels are located farther to the beam than PTV voxels. Then $F_i{}^a = \sum_{p\in PTV\cap\{i\}}(\lambda_p^1 + \lambda_p^2)D_{p,a} + \sum_{p\in Shell\cap\{i\}}\pi_p D_{p,a} + \sum_{p\in OAR\cap\{i\}}(\mu_p + \tau_p)D_{p,a}$. By property 2 of $D_{p,a}$, we know that $\min_{p\in PTV\cap\{i\}} D_{p,a} \geq \max_{p\in Shell\cap\{i\}} D_{p,a}$ and $\min_{p\in PTV\cap\{i\}} D_{p,a} \geq \max_{p\in OAR\cap\{i\}} D_{p,a}$. So we have $DualSum_i = \sum_{p\in V\cap\{i\}}(\lambda_p^1 + \lambda_p^2 + \lambda_p^3 + \pi_p + \mu_p + \tau_p) \geq 0 \Longrightarrow F_i{}^a \geq 0$.
- G3: PTV voxels are projected onto beamlet i and $\lambda_p^1 = \lambda_p^2 = \lambda_p^3 = \pi_p = \mu_p = \tau_p = 0$, then $F_i{}^a = DualSum_i = 0$.
- G4: PTV voxels are projected onto beamlet i and $\exists p \in PTV \cap i, s.t. \lambda_p^3 < 0$. Then $F_i{}^a = \sum_{p\in PTV\cap i}(\lambda_p^1 + \lambda_p^2 + \lambda_p^3)D_{p,a} \geq 0$ cannot be guaranteed by $DualSum_i = \sum_{p\in V\cap\{i\}}(\lambda_p^1 + \lambda_p^2 + \lambda_p^3) \geq 0$.
- G5: Both PTV voxels and OAR/Shell voxels are projected onto beamlet i but some OAR/Shell voxels located closer to the beam than PTV voxels. If any one of π_p, μ_p, τ_p is nonzero, then $F_i{}^a \geq 0$ cannot be guaranteed by $DualSum_i = \sum_{p\in V\cap\{i\}}(\lambda_p^1 + \lambda_p^2 + \lambda_p^3 + \pi_p + \mu_p + \tau_p) \geq 0$.
- G6: Only OAR/Shell voxels are projected onto beamlet i. Then $F_i{}^a = \sum_{p\in Shell\cap\{i\}}\pi_p D_{p,a} + \sum_{p\in OAR\cap\{i\}}(\mu_p + \tau_p)D_{p,a} \leq 0$.

For beamlet i in G1, G2 and G3, $DualSum_i \geq 0$ implies $F_i{}^a \geq 0$ and this relationship is independent of the shape and dose of aperture a. Therefore, beamlets in G1-G3 with $DualSum_i \geq 0$ are of top priority to create new apertures. For beamlet i in G4 and G5, $DualSum_i \geq 0$ cannot guarantee $F_i{}^a \geq 0$ unless we calculate the dose coefficient $D_{p,a}$.

However, the inclusion of G4 and G5 beamlets enlarges the search space of new apertures and is useful to create large apertures. Since G5 beamlets will always reduce the value of F^a, these beamlets should never be used for aperture generation.

Since we do not know $D_{p,a}$, finding the aperture with the largest F^a is impossible for the pricing problem. Since $c_a = 0$ in all optimizations in LLDAO except the step of minimizing total MU, where $c_a = 1$, the pricing problem ends up with finding an aperture a such that F^a is as large as possible. From the previous discussion, we know that apertures with $DualSum_a = \sum_{i \in a} DualSum_i \geq 0$ are of high possibility to have $F^a > c_a$. Once these apertures are generated, their reduced costs will be checked the same time while their associated dose is calculated. Finally, apertures with $F^a > c_a$ ($R(a) < 0$) will be priced out. Based on our experiment, this heuristic algorithm can efficiently create a large set of apertures with $F^a > c_a$ at each iteration even though no dose information is used to generate these apertures. In addition, we observed that it is not necessary to eliminate apertures with $F^a < c_a$. Although they cannot be entered into basis at current step of the master problem, they may become basis in later steps. So, this aperture generation algorithm can accelerate the optimization of master problem by generating promising apertures that can be included in further steps.

Now we will explain how to generate apertures with $DualSum_a \geq 0$ from dual variables. First, a dual sum map(DSM), which is similar to fluence map, is created for each beam. Beams are discretized into beamlets with certain resolution. As each voxel is uniquely projected to a beamlet, the value of a beamlet i in DSM is $DSM_i = DualSum_i = \sum_{p \in V \cap \{i\}} \left(\lambda_p^1 + \lambda_p^2 + \lambda_p^3 + \pi_p + \mu_p + \tau_p\right)$. Next, a dual fluence map(DFM) will be created

from DSM such that $DFM_i = 1$ if beamlet i is used to create new apertures and $DFM_i = 0$ otherwise. Since $DSM_i < 0$ means that at least one voxel in $V \cap \{i\}$ reaches the dose upper bound, new apertures should avoid directly shooting on these voxels. Hence $DFM_i = 0$ for all beamlets i with $DSM_i < 0$. By considering the dose scattering effect, beamlets that are close to these negative $DualSum$ beamlets may not be used either. Let $\mathrm{i_x}$ and $\mathrm{i_y}$ be the x and y coordinates of beamlet $i \in \mathrm{b}$ and define $E_i^- \coloneqq \{j \in b \mid i_x - d_- \leq j_x \leq i_x + d_-,\ i_y - d_- \leq j_y \leq i_y + d_-,\ d_- \in N^+\}$ as the set of beamlets within d_- of beamlets i. Then $DFM_i = 0, \forall \mathrm{i} \in \{\mathrm{j} \in \mathrm{b} \mid \mathrm{j} \in \mathrm{E_i^-}, \mathrm{DSM_i} < 0\}$. For the remaining beamlets, $DFM_i = 1$ if $DSM_i > 0$. If $DSM_i = DualSum_i = 0$ and $i \in \mathrm{G3}$, we can include i in aperture a without changing the value of $DualSum_a$, but can potentially make a bigger and more regular. Similarly, define $E_i^+ \coloneqq \{j \in b \mid i_x - d_+ \leq j_x \leq i_x + d_+,\ i_y - d_+ \leq j_y \leq i_y + d_+,\ \mathrm{d_+} \in N^+\}$ and $DFM_i = 1, \forall \mathrm{i} \in \{\mathrm{j} \in \mathrm{b} \mid \mathrm{j} \in \mathrm{E_i^+} \cap G3, \mathrm{DSM_i} > 0\}$. Both d_- and d_+ are dilation parameters that control the shape of apertures. Larger d_- will lead to larger F^a but smaller shape while larger d_+ will lead to smaller F^a but larger shape. An example of the whole process is shown in **fig. 4.10a – fig. 4.10d.**

Once DFM is created, we can treat it as a fluence map and run leaf sequencing algorithms to generate apertures. For each aperture a obtained, we have

$$DualSum_a = \sum_{i \in a} DFM_i \times DualSum_i = \sum_{i \in a, DFM_i = 1} DualSum_i \geq 0 \qquad (4.3.4)$$

Since DFM has only one intensity level, leaf sequencing on DFM will be significantly simplified. Common MLC constraints are considered such as row continuity, interdigitation. In this study, Siochi's algorithm[108] are implemented to generate such apertures. In addition, some other MLC constraints specifically for our system, Cyberknife,

are also included: (1) minimum aperture area is 57.75mm^2; (2) minimum leaf opening is 5mm; (3) the opening must be at least 2 leaves wide at any position along the leaf moving direction of MLC. The final constraint is on the regularity of the aperture shape. Let Seq be the area of the equivalent square of an aperture and Ssa be the area of the aperture. Then $\sqrt{\mathrm{Seq}/\mathrm{Ssa}}$ should be greater than 0.57. After apertures are generated by Siochi's algorithm, we changed the shape of each aperture to satisfy these constraints. Basically, if a leaf's opening is less than 5mm, this leaf will be closed to satisfy constraint (2). If a column has only one leaf open, that column will be closed either to satisfy constraint (3). Constraint (1) and the shape regularization constraint will be checked, and failed apertures will be directly eliminated.

It is easy to see that both the Siochi's algorithm and the additional checking procedure runs in polynomial time of the dimension of the DFM. Also, beamlet dose calculation is replaced by aperture dose calculation, which is faster and more accurate. Therefore, our aperture generation algorithm is very efficient in terms of computational time.

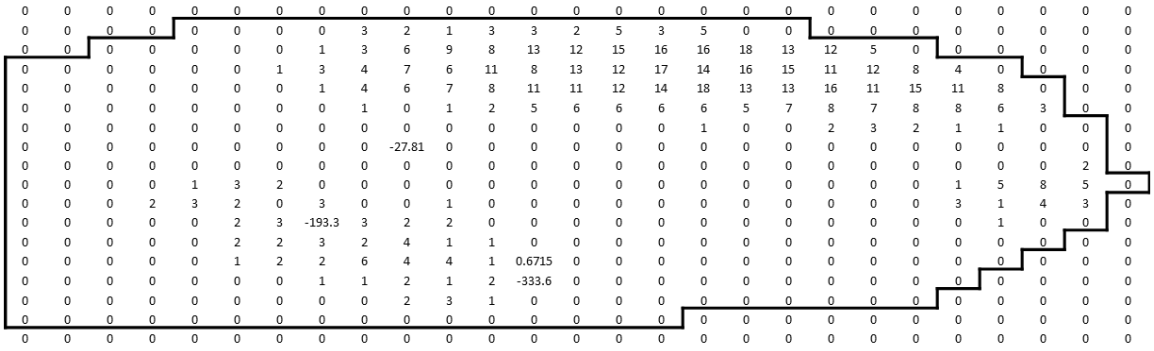

Figure 4.10a. Dual Sum Map (DSM), black lines enclose beamlets where PTV voxels are projected.

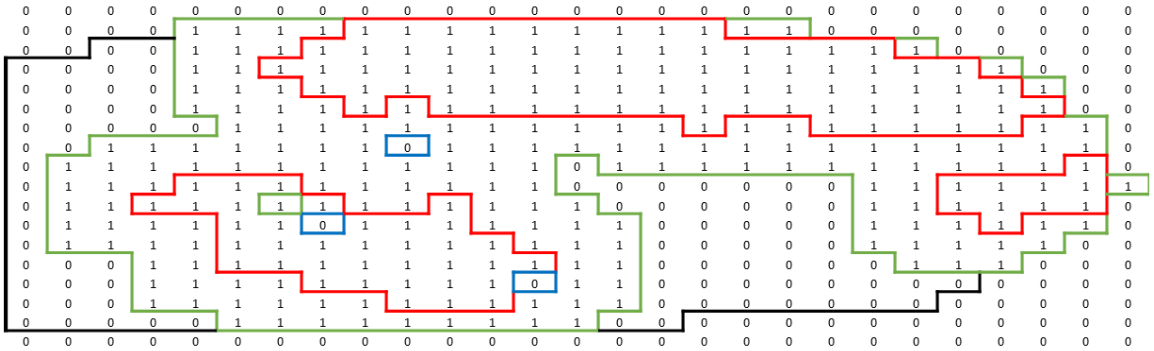

Figure 4.10b. Dual Fluence Map(DFM) with $d_- = 0$ and $d_+ = 2$, red lines enclose beamlets with $DSM_i > 0$, blue lines enclose beamlets with $DSM_i < 0$ and green lines encloses beamlets with $DSM_i = 0$ and within d_+ of beamlets with $DSM_i > 0$.

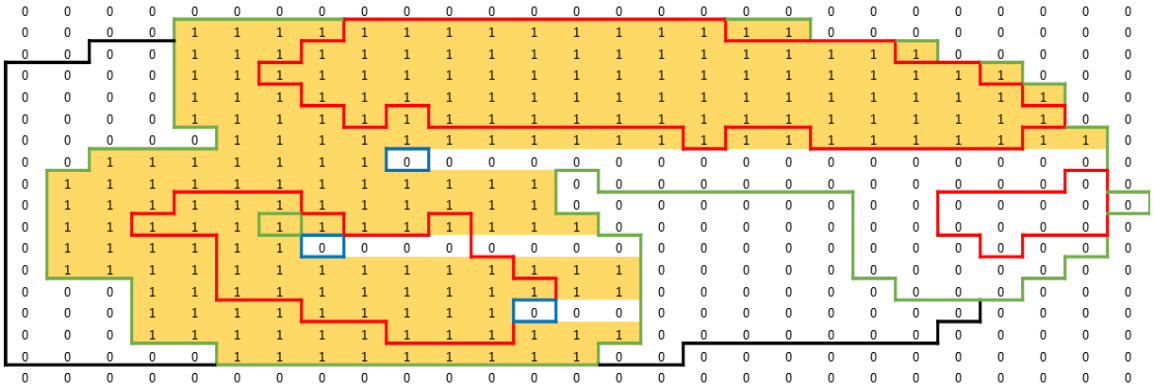

Figure 4.10c. An aperture(shaded) created by running Siochi's leaf sequencing algorithm.

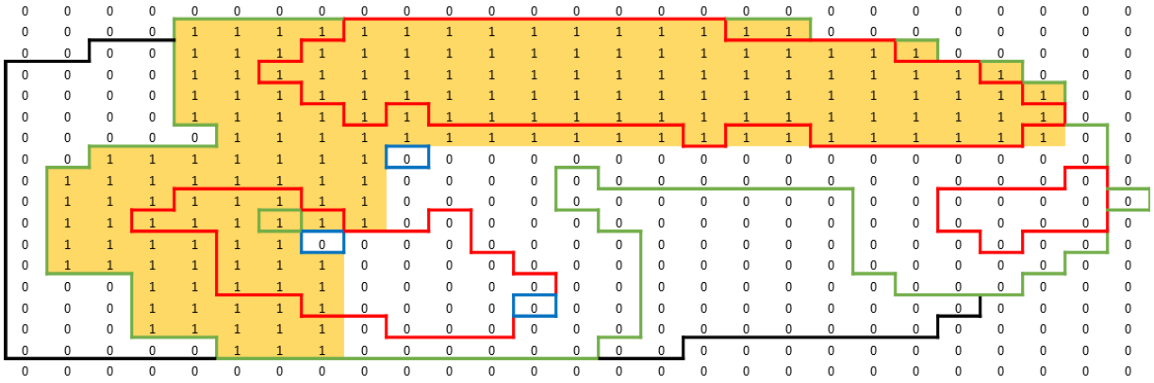

Figure 4.10d. Final Aperture(shaded) with shape corrected to satisfy MLC constraints. After dose calculation, the reduced cost is calculated as -421.547.

4.2.4 Beam Selection

Both fluence map optimization and direct aperture optimization often assume that a set of beam angles are pre-selected before the optimization. These beam angles are either chosen manually by planners or obtained by a heuristic algorithm combining geometry and intensity information. As the beam selection problem is in nature coupled with fluence map optimization, a combining model will outperform models solving these two problems separately. For example, there are mixed-integer models that simultaneously optimize beam angles and fluence pattern and produce global optimal solution of the beam selection and beam profile[96]. However, it usually takes longer time to solve than heuristic approaches, especially when the candidate beam angle set is large[97]. But the plan quality has proven to be superior[96, 98]. For direct aperture optimization, iterative algorithms are proposed to add beam angles greedily based on the first-order information[128]. These methods can return solution quickly but cannot guarantee global optimality of the selected beam angles.

In this thesis, we propose a mixed-integer model that couples the beam selection and direct aperture optimization together. This model, similar to [96], uses binary variable to indicate the selection of a beam angle and constrains on the maximum number of beam angles allowed. However, instead of beamlet weights, aperture weights are optimized. The general form of the model can be formulated as

$$\text{(DAO+BS)} \qquad \text{Min} \quad F(\boldsymbol{x}) \tag{4.4.1}$$

$$s.t. \qquad \boldsymbol{x} \in D, \tag{4.4.2}$$

$$x_a \leq MaxMU\ z_i, \qquad \forall a \in A_i,\ \forall i \in B \tag{4.4.3}$$

$$\sum_{i \in B} z_i \leq B_{max}, \tag{4.4.4}$$

$$x_a \geq\ 0, z_i \in \{0,1\} \qquad \forall a \in A_i,\ \forall i \in B \tag{4.4.5}$$

where D is the set of aperture weight satisfying dose constraints on target and OARs. A_i is the set of apertures of beam $i \in B$ and B_{max} is the maximum number of beams allowed.

Compared to beamlet FMO models in which the total number of beamlets is finite and known before optimization, DAO models have potentially infinite number of apertures and can only obtain a small set of them by column generation. Therefore, to make DAO+BS viable, we need to generate enough aperture shapes for each beam. As the column generation algorithm cannot be directly used to solve DAO+BS, we first solve the DAO with (4.4.2) and all beam angles included. By using the column generation algorithm proposed in 4.2.3, each beam will have many apertures generated and the objective function $F(\boldsymbol{x})$ will be minimized at the same time. Then constraints (4.4.3) - (4.4.5) are added to select at most B_{max} angles with the minimum objective value. Since the number of apertures generated in DAO is typically much smaller than the number of beamlets in FMO, each node in the branch-and-bound tree will be solved faster. Moreover, the optimal solution of DAO+BS, once obtained, is guaranteed the global optimal given the aperture set generated so far by column generation.

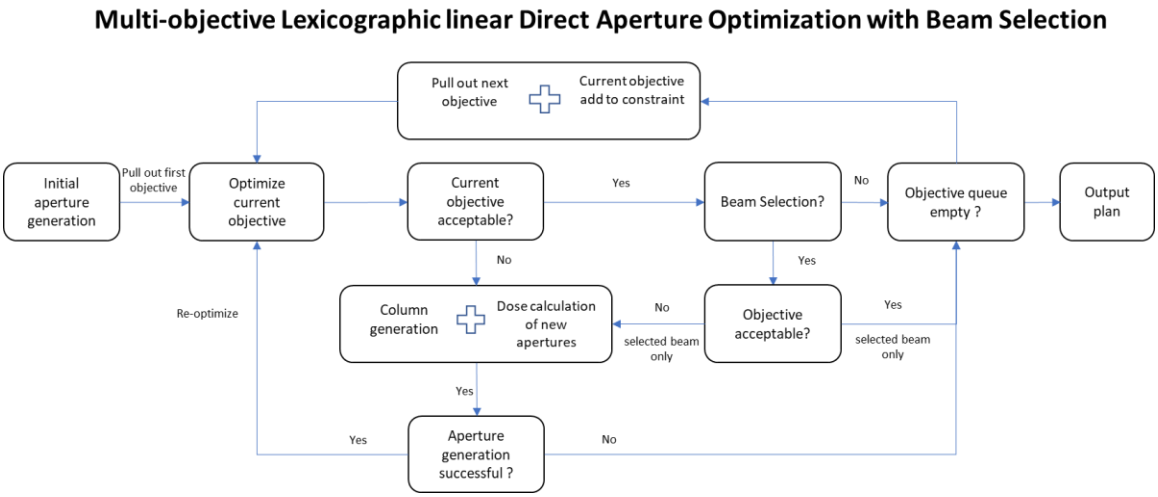

Figure 4.11. Process map of LLDAO with beam selection. Beam selection is performed after one of the steps of LLDAO. Once beams are selected, later optimization will be restricted on the selected beams and new apertures will only be generated from the selected beams.

This beam selection model serves as a module in the LLDAO model introduced in 4.2.2. Since different objectives in LLDAO can end up with different optimal beam selection, DAO+BS can be used after any step to produce a beam set that minimizes a specific treatment objective (**fig. 4.11**). For example, applying beam selection after optimizing conformity index will give a set of beams uniformly distributed in the 2D/3D space so that doses are spread out around the target to ensure good conformity. On the other hand, the set of beams selected after minimizing total dose of an OAR will likely avoid beams that directly pass through that OAR. Compared to plans with no constraints on the number of beams, plans with only a few beams used will likely see a compromise in the quality. To limit the degradation of plan quality, we first solve DAO with all beam angles included. Column generation is used to generate new apertures until no more apertures can be added to improve the objective function. Notice that solving DAO with all beams is the same as solving the LP relaxation of DAO+BS. Therefore, with enough apertures generated, our

algorithm can successfully reduce the number of beams used without compromising much on the plan quality. In our experiment, the degradation of plan quality is within 5% to the plan with all beams. Moreover, we can further close the gap by running one more round of column generation to generate apertures from the selected beam angles and re-optimize the same objective.

4.3 Computational Result

4.3.1 Patient cases and clinical guidelines

4.3.1.1 Prostate cases

We first tested the efficacy of our algorithm on 5 prostate cases. Voxels are sampled using $2\times2\times2mm^3$ for all structures. In addition to PTV and OARs, shell structures are also sampled to be used to optimize conformity. Each shell structure is the dilation of the surface of PTV by a certain distance. For prostate cases, shell structures located at 2mm, 4mm from PTV are used to control conformity and low dose spillage. The details of each case are described in **Table 4.1**. Treatment objectives are derived from RTOG 0938 [129] and are summarized in **Table 4.2**. The prescription dose is 36.25Gy per 5 fraction and the isodose should cover at least 95% of the PTV volume. The metric "D1cc < 38.06" means at most 1cc of rectum/bladder can have dose greater than 38.06Gy.

Table 4.1. Structure size of each prostate case

Structures	Prostate 1		Prostate 2		Prostate 3		Prostate 4		Prostate 5	
	# of voxel	Size (cm^3)	# of voxel	Size (cm^3)	# of voxel	Size (cm^3)	# of voxel	Size (cm^3)	# of voxel	Size (cm^3)
PTV	8393	67.14	12419	99.35	7780	62.24	14444	115.55	9168	73.34
Bladder	4124	32.99	7764	62.11	8056	64.45	10983	87.86	5320	42.56
Rectum	6413	51.30	8804	70.43	7203	57.62	8160	65.28	6681	53.45
Prostatic Urethra	319	2.55	434	3.47	278	2.22	274	2.19	276	2.21
Shell	8331	66.648	10287	82.30	8272	66.18	11191	89.53	8725	69.80

Table 4.2. Treatment objectives for prostate cases (36.25Gy/5Fx)

Structure	Metric	Goal (Gy)
PTV	D95%	>36.25
PTV	D100%	>34.4
PTV	D0%	<43.5
Rectum	D1cc	<38.06
Rectum	D90%	<32.625
Rectum	D80%	<29.00
Rectum	D50%	<18.125
Bladder	D1cc	<38.06
Bladder	D90%	<32.625
Bladder	D50%	<18.125
Prostatic Urethra	D0%	<38.78

4.3.1.2 Lung cases

Lung cases are discretized using the same voxel size as prostate cases, $2\times2\times2mm^3$ for all structures. Moreover, shell structures located at 2mm, 4mm and 20mm from PTV are used to control conformity and R50, which is the ratio of the volume of 50% of the prescription dose isodose to the volume of the PTV[130]. **Table 4.3** summarizes the size of each

structure and **Table 4.4** shows the treatment objectives which are derived from RTOG 0813 [130].

Table 4.3. Structure size of each lung case

Structures	Lung 1		Lung 2		Lung 3		Lung 4		Lung 5	
	# of voxel	Size (cm^3)	# of voxel	Size (cm^3)	# of voxel	Size (cm^3)	# of voxel	Size (cm^3)	# of voxel	Size (cm^3)
PTV	11215	89.72	18616	148.93	3726	29.81	11573	92.58	10177	81.42
Spinal	1860	14.88	3388	27.10	1809	14.47	1387	11.10	2469	19.75
Esophagu	1301	10.41	4015	32.12	1472	11.78	1936	15.49	2643	21.14
Heart[1]	60572	484.58	--	--	--	--	8690	69.52	--	--
Trachea	1272	10.18	1404	11.23	1629	13.03	463	3.70	2961	23.69
Proximal Bronchus	505	4.04	331	2.65	460	3.68	812	6.50	458	3.66
Lung	488938	3911.50	559039	4472.31	291112	2328.90	363402	2907.22	420691	3365.53
Vessels	--	--	19338	154.70	--	--	--	--	--	--
Brachial Plexus	--	--	1956	15.65	--	--	--	--	3694	29.55
Shell	10369	82.95	17206	137.65	5490	43.92	10241	81.93	9205	73.64

1. "--" means that such structure is not delineated in the DICOM and is not considered in the treatment planning optimization of that case.

Table 4.4. Treatment objectives for Lung cases (50Gy/5Fx)

Structure	Metric	Goal (Gy)
PTV	D95%	>50
PTV	D99%	>45
PTV	D0%	<62.5
Cord	D0%	<30
Cord	D0.25cc	<22.5
Cord	D0.5cc	<13.5
Lung	D1500cc	<12.5
Lung	D1000cc	<13.5
Esophagus	D0%	<52.5
Esophagus	D5cc	<27.5

Table 4.4 continued

Heart	D0%	<52.5
Heart	D15cc	<32
Trachea	D0%	<52.5
Trachea	D4cc	<18
Proximal bronchus	D0%	<52.5
Proximal bronchus	D4cc	<18
Brachial Plexus	D0%	<32
Brachial Plexus	D3cc	<30
vessels	D0%	<52.5
vessels	D10cc	<47

4.3.1.3 Intracranial cases

We also tested our algorithm on 5 intracranial cases, including a schwannoma case, a pituitary case, two meningioma cases and a brain metastases case. Since the tumors in some cases are very tiny, the voxel size is set to be $1\times1\times1mm^3$. Each case has unique clinical objectives and the details are shown in **Table 4.5 - 4.9.**

Table 4.5. Structure size and treatment objectives for Intracranial 1 (12Gy/1Fx)

Structure	# of voxels[1]	Size (cm^3)	Metric	Goal (Gy)
PTV	1299	1.30	D98%	>12
PTV			D100%	>11
Brainstem	37204	37.20	D0%	<12.5
Facialis	728	0.73	D0%	<15
CAI	14	0.01	D0%	<14
Trigeminus	514	5.14	D0%	<15
Left Eye	8570	8.57	D0%	<0.5
Left Optic Nerve	1365	1.37	D0%	<1
Right Eye	8714	8.71	D0%	<0.5
Right Optic Nerve	1532	1.53	D0%	<1
Pituitary	336	0.34	D0%	<1
Optic Chiasm	1512	1.51	D0%	<1

1. The voxel size is $1\times1\times1mm^3$.

Table 4.6. Structure size and treatment objectives for Intracranial 2 (25Gy/5Fx)

Structure	# of voxels[1]	Size (cm3)	Metric	Goal (Gy)
PTV	3657	3.66	D95%	>25
PTV			D0%	<42
Brainstem	33748	33.75	D0%	<12
Left Eye	10234	10.23	D0%	<2
Left Optic Nerve	492	4.92	D0%	<13.5
Right Eye	10274	10.27	D0%	<2
Right Optic Nerve	756	7.56	D0%	<13.5
Mandible	46280	46.28	D0%	<5
Optic Chiasm	139	0.14	D0%	<12

1. The voxel size is $1\times1\times1mm^3$.

Table 4.7. Structure size and treatment objectives for Intracranial 3 (25Gy/5Fx)

Structure	# of voxels	Size (cm3)	Metric	Goal (Gy)
PTV	3265	26.12	D95%	>25
Left Eye	846	6.77	D0%	<2
Right Eye	882	7.06	D0%	<2
Brainstem	2634	21.07	D0%	<35
Optic System	247	1.98	D0%	<18
Whole brain	201813	1614.5	D20cc	<12

Table 4.8. Structure size and treatment objectives for Intracranial 4 (25Gy/5Fx)

Structure	# of voxels	Size (cm3)	Metric	Goal (Gy)
PTV	2982	23.86	D95%	>25
PTV			D0%	<62.5
Left Eye	952	7.62	D0%	<2
Right Eye	994	7.95	D0%	<2
Brainstem	2906	23.25	D0%	<17.5
Left Optic Nerve	168	1.34	D0%	<25.5
			D0.25cc	<15
Right Optic Nerve	122	0.98	D0%	<25.5
			D0.25cc	<15
Optic Chiasm	64	0.51	D0%	<25.5
			D0.25cc	<15
Spinal cord	292	2.34	D0%	<12.5
Whole brain	162856	1302.85	D43cc	<12

Table 4.9. Structure size and treatment objectives for Intracranial 5 (20Gy/1Fx)

Structure	# of voxels[1]	Size (cm3)	Metric	Goal (Gy)
GTV1	539	0.539	D95%	>20
GTV2	408	0.408	D95%	>20
GTV3	74	0.074	D95%	>20
GTV4	2787	2.79	D95%	>20
GTV5	129	0.129	D95%	>20
Brainstem	25666	25.67	D0.3cc	<12
Whole brain	1196182	1196.18	D30cc	<10
			D20cc	<12
Left Optic Nerve	326	3.26	D0.2cc	<8
Right Optic Nerve	326	3.26	D0.2cc	<8
Left Hippocampus	1986	1.86	mean	<3
Right Hippocampus	2435	2.44	mean	<3
Optic Chiasm	331	0.33	D0%	<8
Left Lens	151	1.51	D0%	<2
Right Lens	175	1.75	D0%	<2
Left Eye	8892	8.89	D0%	<8
Right Eye	9050	9.05	D0%	<8

1. The voxel size is $1\times1\times1mm^3$.

For all 15 cases, by considering the delivery of radiation in real practice, the minimum MU of an aperture is set to be 10 MU per fraction and the maximum MU is set to be 200 MU per fraction. The total MU is an objective which will be minimized in the LLDAO.

4.3.2 Beams and initial apertures

Candidate beams are created using the node position in body/head paths implemented in the CyberKnife system. Beams are non-coplanar and uniquely determined by the node position from which the beams are delivered, up vector of the LINAC and target position/isocenter (**fig. 4.12**). Moreover, beams that directly pass through a critical organ or avoidance structure before reaching the target will be eliminated. Although this

additional preprocessing procedure often makes the planning more difficult, it benefits the patients in real practice by further reducing radiation to normal tissues. The multi-leaf collimator consists of 26 leaf pairs with each of width 3.85mm. Leaves move in the direction that are perpendicular to both the up vector and the direction from the node position to the target position. In this study, we generated the beamlets of size $3.85\times2mm^2$ for all prostate and lung cases and $3.85\times1mm^2$ for intracranial cases. The number and location of isocenters are decided by the isocenter selection algorithm introduced in section 4.2.1. The average solution time for solving the isocenter problem is 41.73 seconds for lung cases and 24.34 seconds for intracranial cases.

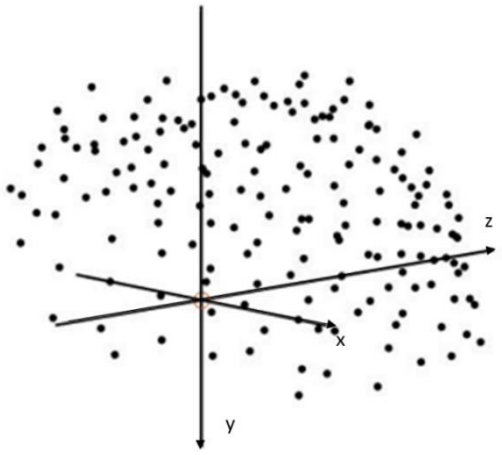

Figure 4.12. Candidate non-coplanar beams in CT space. There are 171 node positions (dot) with 1 isocenter (red circle)

To start the LLDAO, we generated a set of initial apertures for each beam from the projection of PTV onto the MLC plane, which is spanned by the up vector and the leaf motion direction. For each beam, apertures will be generated from beamlets where PTV voxels are projected. Moreover, beamlets will be subtracted if there are OAR voxels, which

locate closer to the beam than PTV voxels, projected into it. **Fig. 4.13** shows an example of creating initial apertures from this procedure. Often multiple apertures will be created if the projection is of irregular shape or disconnected. Moreover, aperture shapes are corrected to satisfy delivery constraints on MLC, such as row continuity, interdigitation. Apertures with area smaller than the minimum requirement will be discarded. Details of each case are summarized in **Table 4.10**.

Table 4.10. Size of beam and initial aperture set

Case	# of isocenters	# of beams[1]	# of initial apertures
Prostate 1	1	62	63
Prostate 2	1	67	67
Prostate 3	1	76	76
Prostate 4	1	49	49
Prostate 5	1	59	59
Lung 1	2	134	134
Lung 2	3	191	285
Lung 3	1	83	83
Lung 4	2	173	175
Lung 5	2	141	155
Intracranial 1	2	211	187
Intracranial 2	3	436	474
Intracranial 3	2	289	303
Intracranial 4	1	140	141
Intracranial 5	5	675	1142

1. The number of beams after preprocessing

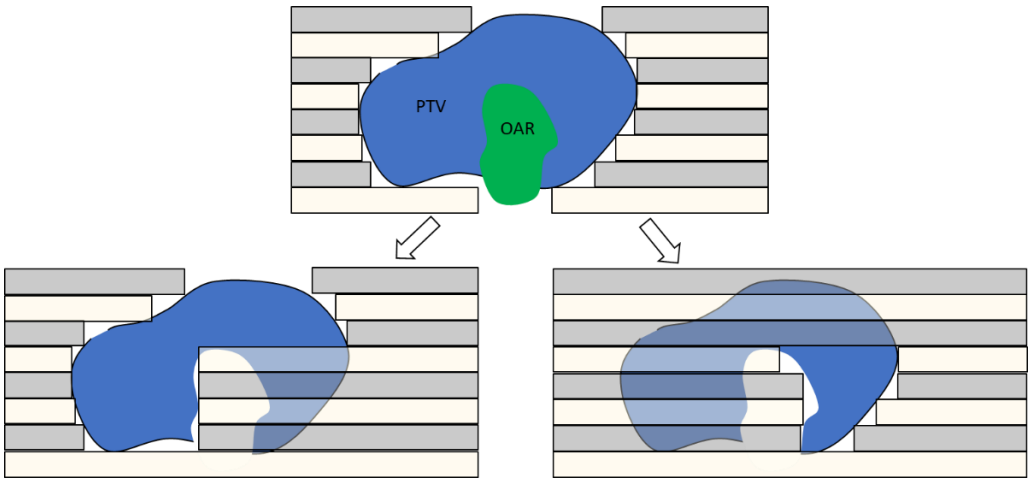

Figure 4.13. Initial apertures are created to cover PTV projection subtracted by OAR projection

4.3.3 Optimization result

Based on the clinical objectives of each case, 4 main steps are implemented in the LLDAO to generate the treatment plan. The first step is to satisfy PTV minimum dose level and coverage requirements. All beam angles will be included in the optimization. Step 2 of LLDAO optimizes conformity index by minimizing dose to shell structures. Beam angle optimization will also be implemented to select a subset of beam angles out of the whole candidate beam set. In step 3, dose to OARs will be minimized. The order of each OAR added into LLDAO is based on the number of voxels that are close to the target. The last step is to minimize total MU of the plan. There are two considerations of optimizing conformity and beam selection in step 2. First, plans obtained after this step have rapid dose fall-off outside PTV, which means little dose will be deposited to surrounding OARs. Therefore, it will be easy to optimize the dose of OARs in the following steps. Second, based on our experiment, beam selection plays a critical role in optimizing conformity. The conformity index of a plan with poor beam selection can be much worse than one with good beam selection. And such difference cannot be decreased by simply generating new apertures. Therefore, we optimize beam selection in this step to obtain a set of beams with good (small) conformity index. Moreover, with beam selected in step 2, we only need to generate new apertures from the selected beam angles in the following steps so that the computation time can be saved.

When optimizing each step in LLDAO, new apertures will be generated if the current objective does not satisfy the clinical requirement. However, objectives that do not have a specific clinical requirement (e.g. conformity index, total MU) will be optimized until no new apertures can be generated by the column generation algorithm. After a step is

finished, the objective function will be put into constraints in the next step and will be constrained by the optimal objective value relaxed by 1%. **Fig. 4.14a – Fig. 4.14g** shows the progress of plan quality during LLDAO for prostate 1. Starting with the initial aperture set and the entire candidate beam set, minimum dose requirement and 95% prescription dose coverage of PTV are first satisfied respectively. By ensuring PTV requirements, dose to shell structures are then minimized to reduce conformity index. Clearly more beams and apertures are needed in this step to spread out radiation around the target.

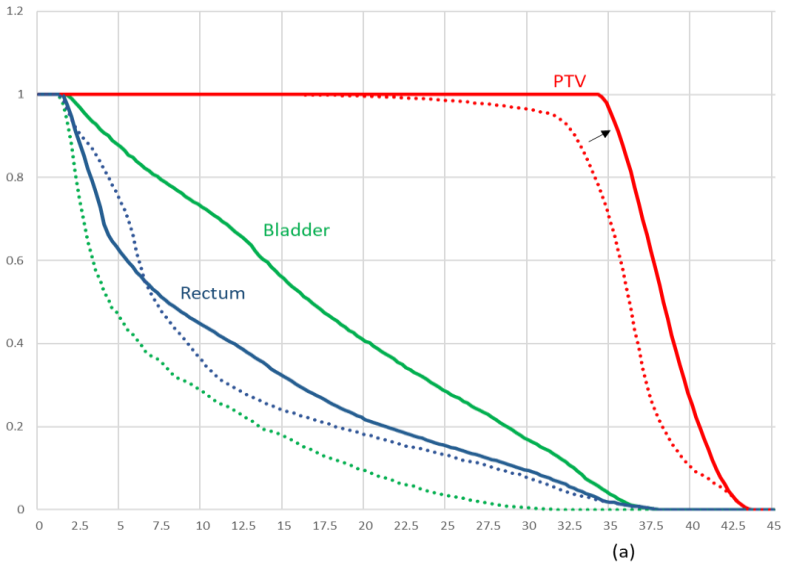

Metric	Step 0	Step 1
PTV D95%	31.57	35.10
PTV D100%	13.92	34.40
PTV D0%	43.50	43.50
Rectum D1cc	34.84	34.88
Rectum D90%	27.90	29.47
Rectum D80%	18.20	21.30
Rectum D50%	7.17	7.89
Bladder D1cc	25.68	35.38
Bladder D90%	19.48	32.79
Bladder D50%	4.30	16.71
Prostatic Urethra D0%	38.78	38.78
Conformity Index	1.40	1.35
# of beams	8	34
# of apertures	9	51
Total MU	6929.27	10622.90

Figure 4.14a. Increase dose to PTV to satisfy minimum dose requirement 34.4Gy.

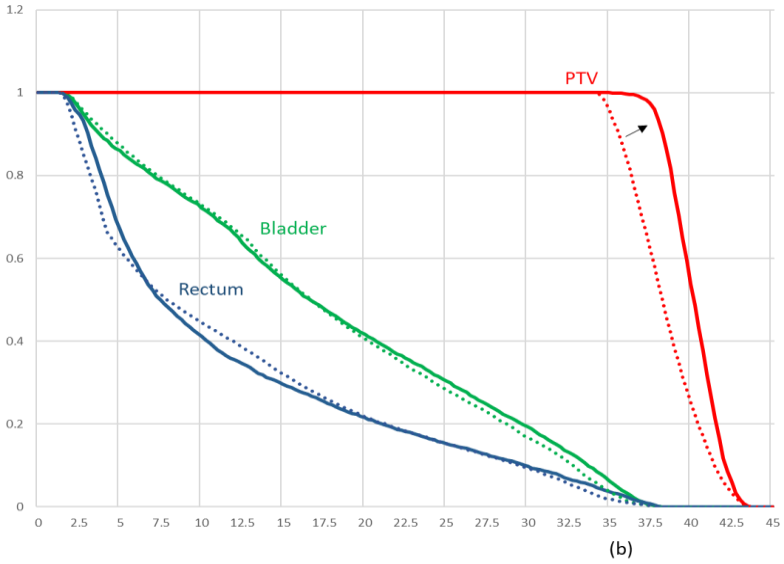

Metric	Step 1	Step 2
PTV D95%	35.10	37.88
PTV D100%	34.40	35.03
PTV D0%	43.50	43.50
Rectum D1cc	34.88	36.36
Rectum D90%	29.47	29.83
Rectum D80%	21.30	21.07
Rectum D50%	7.89	7.46
Bladder D1cc	35.38	36.22
Bladder D90%	32.79	33.69
Bladder D50%	16.71	16.63
Prostatic Urethra D0%	38.78	38.78
Conformity Index	1.35	1.47
# of beams	34	34
# of apertures	51	53
Total MU	10622.90	13205.60

Figure 4.14b. Maximize lower 5% CVaR of PTV dose distribution to ensure 95% of PTV voxels have dose greater than 36.25Gy

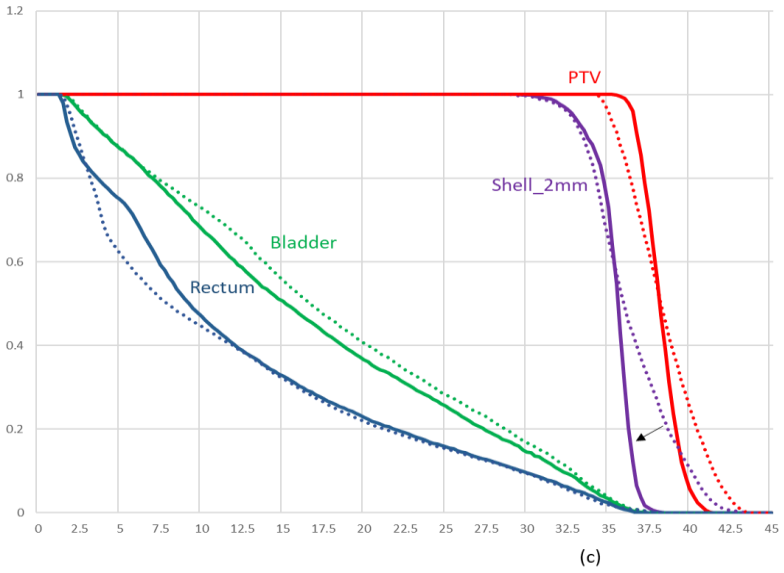

Metric	Step 2	Step 3
PTV D95%	37.88	36.54
PTV D100%	35.03	35.20
PTV D0%	43.50	41.56
Rectum D1cc	36.36	35.23
Rectum D90%	29.83	29.65
Rectum D80%	21.07	21.89
Rectum D50%	7.46	9.27
Bladder D1cc	36.22	35.14
Bladder D90%	33.69	32.10
Bladder D50%	16.63	15.20
Prostatic Urethra D0%	38.78	38.78
Conformity Index	1.47	1.09
# of beams	34	44
# of apertures	53	101
Total MU	13205.60	14088.70

Figure 4.14c. Minimize dose to Shell_2mm structure to reduce conformity index.

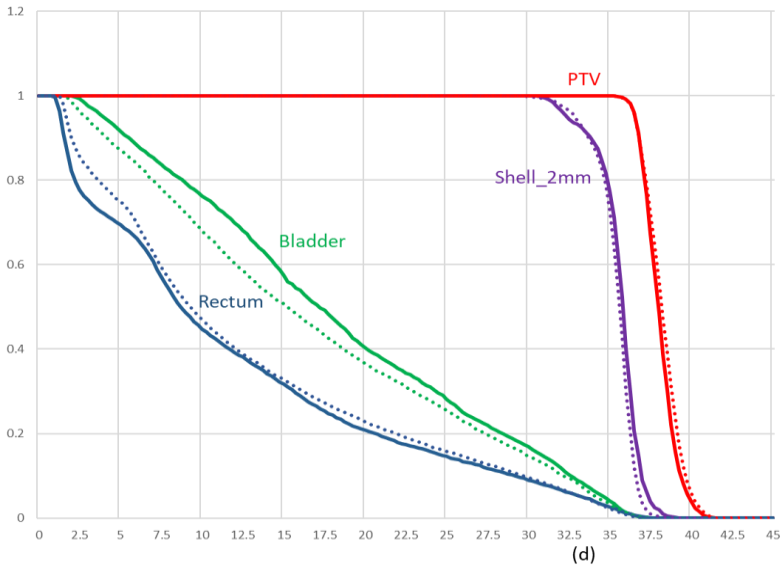

Metric	Step 3	Step 4
PTV D95%	36.54	36.56
PTV D100%	35.20	34.73
PTV D0%	41.56	42.14
Rectum D1cc	35.23	35.46
Rectum D90%	29.65	29.24
Rectum D80%	21.89	20.61
Rectum D50%	9.27	8.68
Bladder D1cc	35.14	35.37
Bladder D90%	32.10	32.58
Bladder D50%	15.20	17.19
Prostatic Urethra D0%	38.78	38.78
Conformity Index	1.09	1.12
# of beams	44	20
# of apertures	101	72
Total MU	14088.70	13557.90

Figure 4.14d. Minimize dose to Shell_2mm with only 20 beams allowed to be selected.

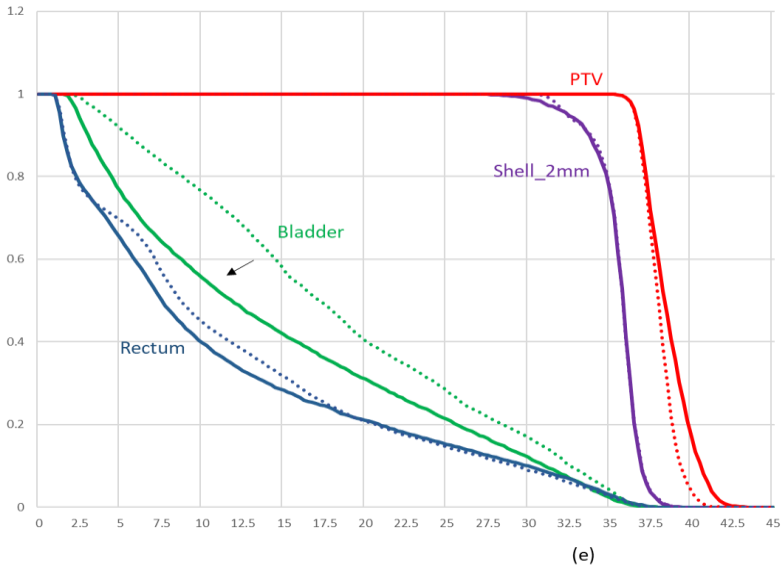

Metric	Step 4	Step 5
PTV D95%	36.56	36.59
PTV D100%	34.73	34.40
PTV D0%	42.14	43.50
Rectum D1cc	35.46	35.78
Rectum D90%	29.24	29.90
Rectum D80%	20.61	20.82
Rectum D50%	8.68	7.56
Bladder D1cc	35.37	34.54
Bladder D90%	32.58	30.98
Bladder D50%	17.19	11.79
Prostatic Urethra D0%	38.78	38.78
Conformity Index	1.12	1.12
# of beams	20	20
# of apertures	72	71
Total MU	13557.90	15175.80

Figure 4.14e. Minimize mean dose of bladder using 20 beams selected by beam angle optimization.

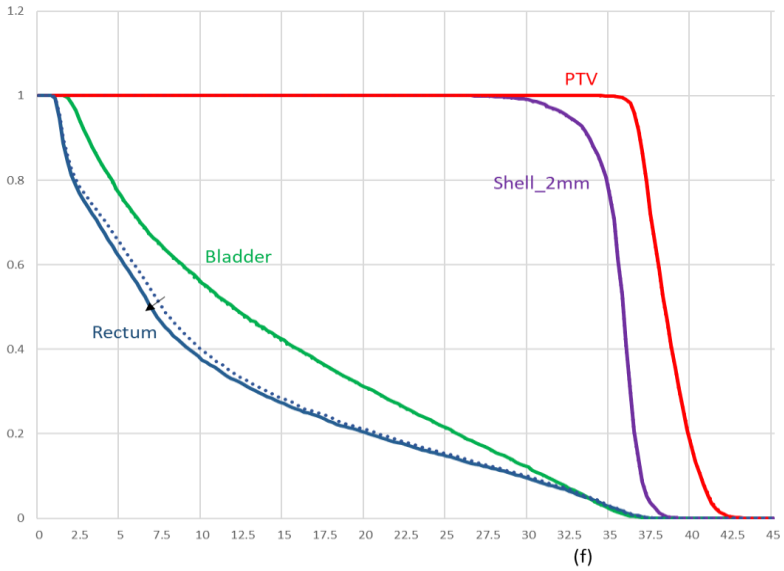

Metric	Step 5	Step 6
PTV D95%	36.59	36.59
PTV D100%	34.40	34.40
PTV D0%	43.50	43.50
Rectum D1cc	35.78	35.67
Rectum D90%	29.90	29.51
Rectum D80%	20.82	20.24
Rectum D50%	7.56	6.85
Bladder D1cc	34.54	34.58
Bladder D90%	30.98	31.03
Bladder D50%	11.79	11.89
Prostatic Urethra D0%	38.78	38.78
Conformity Index	1.12	1.12
# of beams	20	20
# of apertures	71	72
Total MU	15175.80	15198.00

Figure 4.14f. Minimize mean dose of rectum using 20 beams selected by beam angle optimization.

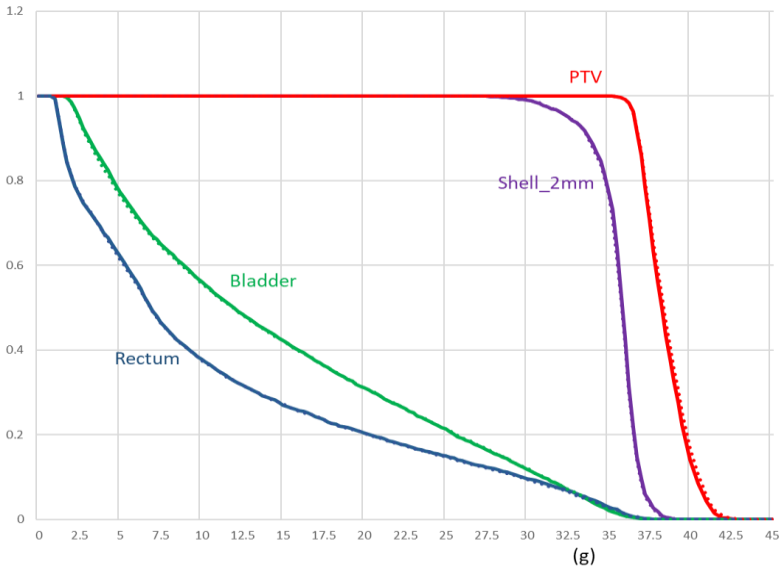

Metric	Step 6	Step 7
PTV D95%	36.59	36.57
PTV D100%	34.40	34.40
PTV D0%	43.50	43.15
Rectum D1cc	35.67	35.66
Rectum D90%	29.51	29.65
Rectum D80%	20.24	20.25
Rectum D50%	6.85	6.89
Bladder D1cc	34.58	34.52
Bladder D90%	31.03	30.93
Bladder D50%	11.89	11.94
Prostatic Urethra D0%	38.78	38.78
Conformity Index	1.12	1.12
# of beams	20	20
# of apertures	72	62
Total MU	15198.00	13759.30

Figure 4.14g. Minimize total MU with the minimum MU allowed for an open aperture set as 50.

Beam angle optimization is performed to select a set of beams with the minimum dose to shell structures given the aperture set generated until this step. Since mixed-integer program usually takes a long time to reach optimal, the first intermediate feasible solution obtained with optimality gap less than 1% will be selected. Compared to the plan with no limit on the number of beams used, plans after beam selection have a slight increase in conformity index. **Table 4.11** summarizes the change of conformity index when the maximum number of beams allowed, B_{max}, is constrained. For most of the cases, the degradation of conformity, due to beam selection, is less than 5%. Moreover, conformity improves as B_{max} increases. It shows that the beam angle optimization model, with enough apertures generated by the column generation algorithm, effectively reduces the number of beams used while maintaining the quality of the plan.

Table 4.11. Conformity index(CI) of the plan after beam selection with different B_{max}

Case	B_{max} = 20		B_{max} = 25		B_{max} = 30		B_{max} = 35[1]		B_{max} = 40[1]		All
	CI	% of increase	CI	% of increase	CI	% of increase	CI	% of increase	CI	% of increase	CI
Prostate 1	1.109	1.85	1.104	1.34	1.098	0.82	--	--	--	--	1.089
Prostate 2	1.111	3.29	1.104	2.56	1.091	1.42	--	--	--	--	1.076
Prostate 3	1.089	1.23	1.085	0.85	1.080	0.38	--	--	--	--	1.076
Prostate 4	1.104	1.56	1.098	0.98	1.094	0.63	--	--	--	--	1.087
Prostate 5	1.108	2.91	1.109	2.94	1.108	2.86	--	--	--	--	1.077
Lung 1	1.032	1.02	1.029	0.73	1.028	0.67	--	--	--	--	1.021
Lung 2	1.154	8.34	1.137	6.82	1.130	6.17	--	--	--	--	1.065
Lung 3	1.089	3.49	1.074	2.1	1.064	1.1	--	--	--	--	1.052
Lung 4	1.071	2.69	1.069	2.57	1.061	1.78	--	--	--	--	1.042
Lung 5	1.091	3.78	1.068	1.54	1.066	1.37	--	--	--	--	1.051
Intracranial	--	--	--	--	1.143	4.15	1.143	4.15	1.143	4.15	1.097
Intracranial	--	--	--	--	1.191	1.17	1.183	0.44	1.179	0.11	1.177
Intracranial	--	--	--	--	1.095	0.18	1.096	0.31	1.095	0.16	1.093
Intracranial	--	--	--	--	1.231	4.13	1.205	1.92	1.185	0.29	1.182
Intracranial	--	--	--	--	1.304	6.53	1.261	3.05	1.260	2.96	1.224

After beam selection, doses to OARs are minimized to satisfy the dose-volume constraints. For structures with large number of voxels, we divide the whole structure into several small parts based on the distance to the target. Parts close to the target will be first added to the optimization since the dose to these parts are higher than those far away from the target. This procedure prevents the size of the optimization from being too large and reduces the solution time. The last step of LLDAO is to minimize total MU of the plan. By generating new apertures, we can reduce the total MU while maintaining the quality of the plan (**fig. 4.14(g)**). Moreover, the mixed-integer program (step 5' in section 2.3) will be solved to ensure that all selected apertures will be at least 10 MU per fraction. The plan quality of the final solutions is shown in **Table 4.12-4.18**.

Table 4.12. Plan quality of the optimal solution for 5 prostate cases

Structure Metric	Goal (Gy)	Prostate 1	Prostate 2	Prostate 3	Prostate 4	Prostate 5
PTV D95%	>36.25	36.57	36.56	36.63	36.64	36.61
PTV D100%	>34.4	34.40	34.40	34.40	34.40	34.40
PTV D0%	<43.5	43.15	43.28	41.74	43.50	42.99
Rectum D1cc	<38.06	35.66	35.68	35.53	35.32	35.65
Rectum D90%	<32.625	29.65	28.35	26.87	29.42	31.07
Rectum D80%	<29.00	20.25	18.73	16.04	21.50	24.10
Rectum D50%	<18.125	6.89	5.41	2.43	5.37	6.01
Bladder D1cc	<38.06	34.52	34.67	30.32	35.58	35.58
Bladder D90%	<32.625	30.93	28.28	14.25	29.18	32.21
Bladder D50%	<18.125	11.94	11.11	2.69	12.95	16.34
Prostatic Urethra	<38.78	38.78	38.78	38.78	38.78	38.78
Conformity Index		1.12	1.12	1.12	1.12	1.12
# of beams		20	20	19	20	20
# of apertures		62	83	52	84	75
Total MU		13759.30	14710.80	11542.40	17817.80	15419.60

Table 4.13. Plan quality of the optimal solution for 5 lung cases Structure Metric

Structure Metric	Goal	Lung 1	Lung 2	Lung 3	Lung 4	Lung 5
PTV D95%	>50	51.10	50.00	50.55	50.81	50.85
PTV D99%	>45	49.48	48.82	49.64	49.62	49.58
PTV D0%	<62.5	62.50	61.74	57.05	59.89	61.30
Cord D0%	<30	9.11	14.66	13.51	14.00	14.00
Cord D0.25cc	<22.5	8.21	13.04	12.15	13.58	13.65
Cord D0.5cc	<13.5	7.73	12.23	11.50	13.38	13.28
Lung D1500cc	<12.5	5.73	4.88	1.29	3.29	0.73
Lung D1000cc	<13.5	9.97	7.12	3.62	6.63	1.78
Esophagus D0%	<52.5	35.04	45.29	27.25	19.23	40.73
Esophagus D5cc	<27.5	12.44	27.50	14.71	8.71	16.01
Heart D0%	<52.5	49.10	--	--	45.04	--
Heart D15cc	<32	21.60	--	--	20.96	--
Trachea D0%	<52.5	3.58	42.22	27.60	4.18	47.22
Trachea D4cc	<18	1.14	20.85	15.81	1.14	20.30
Proximal bronchus	<52.5	48.13	32.78	33.79	50.12	7.76
Proximal bronchus	<18	3.72	11.83	7.89	10.14	1.50
Brachial Plexus	<32	--	29.35	--	--	19.37
Brachial Plexus	<30	--	14.76	--	--	11.66
Vessels D0%	<52.5	--	50.59	--	--	--
Vessels D10cc	<47	--	35.29	--	--	--
Conformity Index		1.09	1.08	1.09	1.09	1.09
# of beams		21	29	18	24	22
# of apertures		78	161	46	73	59
Total MU		39887.60	81418.8	19901.4	36374.3	30870.6

Table 4.14. Plan quality of the optimal solution for intracranial case 1

Structure Metric	Goal (Gy)	Intracranial 1
PTV D98%	>12	12.09
PTV D100%	>11	11.67
Brainstem D0%	<12.5	12.50
Facialis D0%	<15	14.43
CAI D0%	<14	13.74
Trigeminus D0%	<15	12.41
Left Eye D0%	<0.5	0.04
Left Optic Nerve D0%	<1	0.13
Right Eye D0%	<0.5	0.07
Right Optic Nerve D0%	<1	0.63
Pituitary D0%	<1	0.20
Optic Chiasm D0%	<1	1.00

Table 4.14 continued

Conformity Index	1.17
# of beams	22
# of apertures	29
Total MU	4048.67

Table 4.15. Plan quality of the optimal solution for intracranial case 2

Structure Metric	Goal (Gy)	Intracranial 2
PTV D95%	>25	25.07
PTV D0%	<42	42.00
Brainstem D0%	<12	12.00
Left Eye D0%	<2	0.61
Left Optic Nerve D0%	<13.5	13.50
Right Eye D0%	<2	1.05
Right Optic Nerve D0%	<13.5	13.50
Mandible D0%	<5	4.73
Optic Chiasm D0%	<12	12.00
Conformity Index		1.34
# of beams		40
# of apertures		44
Total MU		12650.50

Table 4.16. Plan quality of the optimal solution for intracranial case 3

Structure Metric	Goal (Gy)	Intracranial 3
PTV D95%	>25	25.16
Left Eye D0%	<2	2.00
Right Eye D0%	<2	1.88
Brainstem D0%	<35	13.60
Optic System D0%	<18	17.69
Whole brain D20cc	<12	12.65
Conformity Index		1.06
# of beams		30
# of apertures		90
Total MU		14855

Table 4.17. Plan quality of the optimal solution for intracranial case 4

Structure Metric	Goal (Gy)	Intracranial 4
PTV D95%	>25	25.30
PTV D0%	<62.5	35.00
Left Eye D0%	<2	1.65
Right Eye D0%	<2	2.00
Brainstem D0%	<17.5	13.45
Left Optic Nerve D0%	<25.5	25.50
Left Optic Nerve D0.25cc	<15	7.12
Right Optic Nerve D0%	<25.5	24.65
Right Optic Nerve D0.25cc	<15	10.25
Optic Chiasm D0%	<25.5	24.60
Optic Chiasm D0.25cc	<15	11.61
Spinal cord D0%	<12.5	4.40
Whole brain D43cc	<12	9.53
Conformity Index		1.17
# of beams		30
# of apertures		92
Total MU		11260.90

Table 4.18. Plan quality of the optimal solution for intracranial case 5

Structure Metric	Goal (Gy)	Intracranial 5
GTV1 D95%	>20	20.94
GTV2 D95%	>20	21.00
GTV3 D95%	>20	20.05
GTV4 D95%	>20	20.73
GTV5 D95%	>20	20.52
Brainstem D0.3cc	<12	4.02
Whole brain D30cc	<10	7.88
Whole brain D20cc	<12	9.27
Left Optic Nerve	<8	3.53
Right Optic Nerve	<8	0.97
Left Hippocampus	<3	1.00
Right Hippocampus	<3	1.00
Optic Chiasm D0%	<8	2.50
Left Lens D0%	<2	0.73
Right Lens D0%	<2	0.33
Left Eye D0%	<8	6.77
Right Eye D0%	<8	3.47
Conformity Index		1.30
# of beams		35
# of apertures		81
Total MU		18584.30

For all prostate cases, our method produces plans satisfying all dosage criteria with good conformity. All cases use 20 beams (case 3 uses 19) with fewer than 85 apertures. The total MU is less than 18,000 for all cases. Lung cases use multiple isocenters and more beams than prostate cases since the tumor is larger and more irregular. Except for the violation of "trachea D4cc" for case 2 and case 5, all other dosage criteria are satisfied. Lung case 2 and case 5 have trachea adjacent to PTV and we could not find a feasible plan even using the beamlet-based FMO method. Especially for lung case 2, which has the largest tumor (149cc) with all critical structures wrapping around, the plan uses 161 apertures with total MU of 81418.8. Finally, feasible plans for all 5 intracranial cases are generated.

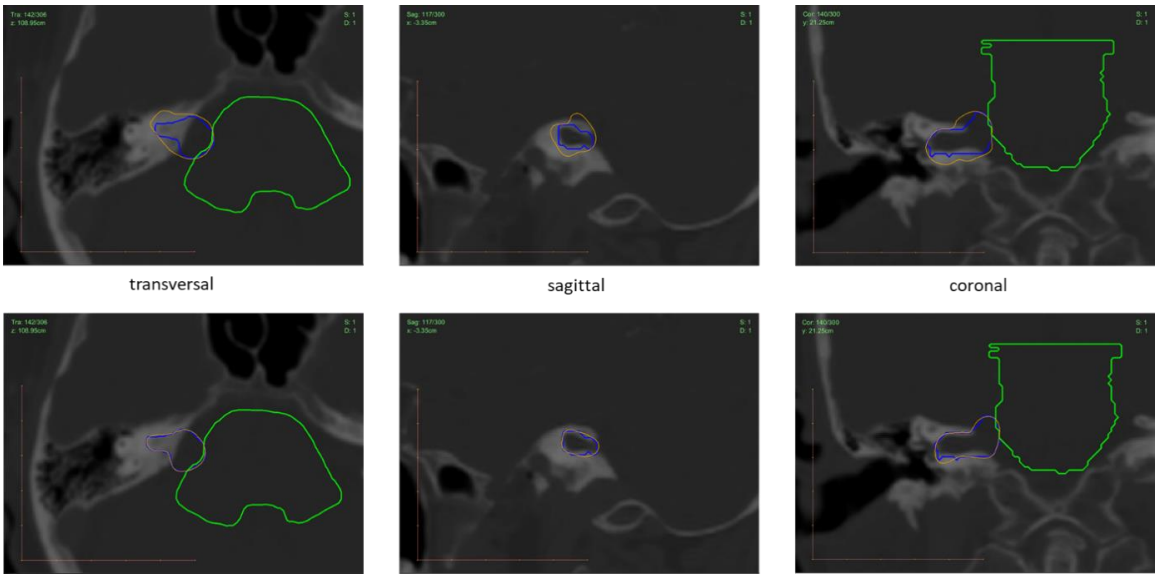

Figure 4.15. Comparison of dose conformity between one-isocenter plan (top) and two-isocenter plan (bottom) for intracranial case 1. PTV(blue), brainstem(green) and the 12Gy isodose line(yellow) is depicted in transversal, sagittal and coronal view. The conformity index of one-isocenter plan is 1.55 and the two-isocenter plan is 1.17.

Low conformity is essential for all clinical cases. For the intracranial cases, excess radiation to normal brain cell is detrimental. Although brain tumors are usually tiny, their shapes are highly irregular and hence one-isocenter plans usually result in poor conformity. However, using multiple beam isocenters can effectively improve the conformity index[98]. The difference in conformity between single-isocenter plan and multi-isocenter plan is significant in **fig. 4.15**. By implementing the isocenter selection algorithm introduced in section 2.1, the two-isocenter plan makes the prescription isodose line tightly conform to the shape of the tumor. Compared to the one-isocenter plan with conformity index 1.55, the two-isocenter plan improves the conformity index to 1.17.

As the radiotherapy planning is a multi-objective optimization, there are no optimal solutions that optimize each objective simultaneously. Medical physicists often generate multiple plans to balance between different objectives and present them for clinicians to select. To evaluate the quality trade-offs of the plan obtained by our LLDAO algorithm, we generate the efficient frontier of the optimization considering three aspects: conformity index, OAR dose and total MU (**fig. 4.16**). By ensuring prescription dose coverage, the weighted sum of these three objectives are optimized using direct aperture optimization with our column generation algorithm. Each point on the efficient frontier represents a pareto-optimal solution of the optimization. The pattern of the efficient frontier is quite similar across the 15 cases. Basically, more aperture MU is needed if we want the plan to have less dose to OARs and be more conformal. The solution obtained by the LLDAO algorithm, which is the star point in figure 15, optimizes each objective sequentially in the order of conformity -> mean OAR dose -> total MU. Therefore, the plan has small

conformity index, low mean OAR dose but high total MU compared to other plans on the efficient frontier.

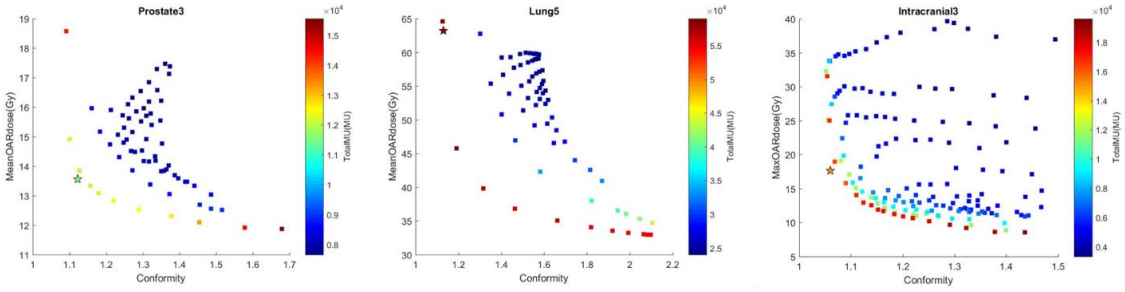

Figure 4.16. Efficient Frontier of the multi-objective direct aperture optimization. Conformity index mean OAR dose (max OAR dose for intracranial cases) and total MU are x, y and z axis respectively. The star points are the optimal LLDAO solution

Table 4.19. Computational statistics of the LLDAO+BS algorithm for 15 cases

Case	Optimization			Aperture generation			Dose Calculation		Total time (cpu sec)
	Linear (cpu sec)	Beam Selection (cpu sec)	TotalMU +MinMU (cpu sec)	Total (cpu sec)	# of aperture	Time (cpu sec)	Aperture-based (cpu sec)	Beamlet-based[1] (cpu sec)	
Pros 1	1200.4	992.6	271.1	2464.1	247.0	39.0	124.3	18600.3	2627.3
Pros 2	3625.9	4156.9	1405.3	9188.1	420.0	74.2	533.6	24899.9	9795.9
Pros 3	1170.4	440.5	421.7	2032.6	338.0	76.5	452.7	29280.4	2561.8
Pros 4	4411.7	6833.7	527.8	11773.2	300.0	59.3	657.4	30940.5	12489.9
Pros 5	2505.5	12130.2	192.8	14828.5	305.0	69.6	605.5	33470.5	15503.7
Lung 1	3912.5	6153.2	197.9	10263.6	901.0	269.2	55862.1	152965.0	66395.0
Lung 2	99578.4	91902.0	6762.0	198242.3	2025.0	914.0	141299.2	250548.0	340455.5
Lung 3	151.8	241.1	15.6	408.5	355.0	58.9	15982.6	120879.0	16450.0
Lung 4	2093.0	8301.2	153.3	10547.5	972.0	288.1	93915.0	165198.0	104750.6
Lung 5	1605.1	1521.2	103.6	3229.9	789.0	209.3	84671.9	141168.0	88111.1
Intra 1	23.6	84.3	16.3	124.2	455.0	111.1	708.9	113379.0	944.2
Intra 2	1237.1	2537.1	101.3	3875.5	1827.0	318.5	5557.3	84838.8	9751.3
Intra 3	704.9	4194.9	905.1	5804.9	3135.0	391.6	267.5	11113.5	6463.9
Intra 4	500.4	6173.8	1386.6	8060.7	1506.0	150.7	152.9	6010.1	8364.4
Intra 5	889.5	14301.0	141.1	15331.6	4371.0	526.3	2808.8	5243.8	18666.6

The linear and mixed-integer programs in the LLDAO+BS method are solved by CPLEX® v12.6.3 with default parameters and the column generation is solved by MATLAB®. The detailed computational statistics is summarized in **Table 4.19**. The entire process consists of three parts: optimization, aperture generation and aperture-based dose calculation. There are two mixed-integer programs in LLDAO+BS model: beam angle optimization and total MU minimization with positive MU lower bound. For all cases, beam angle optimization takes up the majority effort in optimization. Except for lung cases, optimization takes up the majority of solution time. As the lateral scatter correction is needed to calculate dose in lung, the fast GPU accelerated dose calculation algorithm cannot be used. Therefore, dose calculation is much slower and takes up the majority of effort in solving the lung cases. We also include the time of beamlet-based dose calculation, which is needed in traditional FMO and DAO methods, using the same dose calculation algorithm from the Cyberknife. Since the number of beamlets in traditional FMO or DAO is far more than the number of apertures generated in our method, it takes much longer time to calculate the beamlet dose (even longer than the total solution time of our method). This shows that our method, by skipping beamlet dose calculation, is highly efficient to produce plans with good quality.

We also tested the efficiency of the column generation algorithm. Let $N_0(k)$ denote the number of new apertures generated in the k-th step of column generation. After the dose calculation, apertures with negative reduced cost will be added to the optimization and denote the number such apertures as $N_1(k)$. Finally, let $N_2(k)$ be the number of apertures used in the optimal solution of the k-th step. Then we have $N_0(k) \geq N_1(k) \geq N_2(k), \forall$k. In **Fig. 4.17**, $N_0(k), N_1(k), N_2(k)$ and the objective value of each step are shown for 2

optimization problems: maximize PTV 95% coverage for prostate case 1(left) and minimize total MU for lung case 1(right).

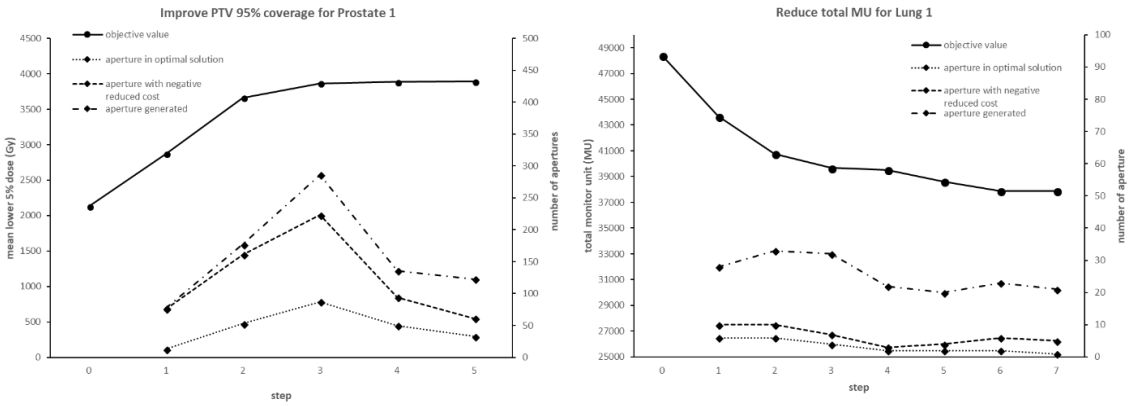

Figure 4.17. Behavior of the column generation algorithm. Left: improving PTV 95% coverage for prostate case 1 with 5 steps of column generation. Right: reducing total MU for lung case 1 with 7 steps of column generation.

In both problems, as the initial aperture set greatly affects the optimization at step 0, N_0 is small in step 1. However, it increases as the step k increases and the objective value improves rapidly during these steps. As the objective value gradually converges, N_0 will then decrease again. For improving PTV 95% coverage, we can see that $N_1(k)/N_0(k)$ decreases and $N_2(k)/N_1(k)$ increases as the optimization proceeds (**table 4.20**). This means that more apertures will be used although fewer l objective-improving apertures are generated. For reducing total MU, however, the efficiency is worse than the previous problem and less predictable. Such difference originates from the column generation algorithm. In section 4.2.3, an aperture a is created if its $DualSum_a > 0$ and then is kept if $F^a > c_a$, which is equivalent to negativity of the reduced cost. For problems where the

objective function only contains dose variables (e.g. PTV 95% coverage), we have $c_a = 0$. However, for the problem of minimizing total MU, we have $c_a = 1$. Therefore, more apertures will be filtered out as they failed to satisfy $F^a > c_a$.

Table 4.20. Efficiency of the column generation algorithm

Step k	Improve PTV 95% coverage		Reduce total MU	
	$N_1(k)/N_0(k)$	$N_2(k)/N_1(k)$	$N_1(k)/N_0(k)$	$N_2(k)/N_1(k)$
$k = 1$	0.987013	0.171053	0.357143	0.6
$k = 2$	0.909605	0.329193	0.30303	0.6
$k = 3$	0.77972	0.390135	0.21875	0.571429
$k = 4$	0.691176	0.531915	0.136364	0.666667
$k = 5$	0.495935	0.540984	0.2	0.5
$k = 6$	--	--	0.26087	0.333333
$k = 7$	--	--	0.238095	0.2

4.4 Conclusion

In this chapter, we studied the entire optimization process of radiotherapy planning. We developed a multi-objective direct aperture optimization model that optimizes each treatment objectives sequentially based on their clinical priority[12-14]. New apertures will be generated until all objectives are clinically acceptable. Unlike current column generation algorithms used in direct aperture optimization, our algorithm does not require beamlet dose calculation to determine the shape of new apertures. Instead, new apertures are created by a heuristic algorithm that only uses dual values. After the dose is calculated using aperture-based dose calculation, apertures will be priced out and added to the optimization. This method not only skips the lengthy beamlet dose calculation but more importantly avoids the issue of dose discrepancy between beamlet-based dose and aperture-based dose

to improve the plan accuracy. Since multiple apertures are generated in each round of column generation, the optimization process converges to the optimal solution much faster than traditional column generation algorithm which only generate one aperture each round.

From the result of 15 test cases, our model produces deliverable plans satisfying clinical requirements. Excluding two mixed-integer programs: beam angle optimization and total MU minimization with positive MU lower bound, each optimization takes less than 1 hour to solve. As we skip the beamlet dose calculation, the whole process can be solved faster than the models using beamlet dose approach. Moreover, plans using our method are deliverable and use small number of apertures. Since minimization of total MU is included as an objective in our model, we can directly address the trade-off between plan quality (dose requirement) and plan efficiency (total MU), which is not possible in the traditional two-step approach. Compare to the clinical plans of these patient cases, our plans are more conformal and expose the OAR and normal tissue to lower radiation dose.

We also incorporated the beam angle optimization into the multi-objective direct aperture optimization to optimally select beam angles. This is the first model that optimize beam angle and aperture weight simultaneously in a direct aperture optimization framework. The mixed-integer model selects a small set of beams with just a little compromise on plan quality. Moreover, we proposed an optimization model to determine the number and location of the isocenters of beams. The result shows that using multiple isocenters can greatly improve dose conformity around the target, especially for tumors with irregular shapes.

Although our heuristic column generation approach avoids the use of beamlet dose, we sacrifice the efficiency of generating objective-improving apertures. In some cases, the ratio of apertures used to the apertures generated is still low, which wastes some time on dose calculation and optimization. Our future research will focus on developing the column generation algorithm to improve the efficiency. Another research direction is to develop a model that optimally determine the priority of each treatment objective so that a personalized optimal treatment plan can be obtained.

Acknowledgment

This work is partially supported by a grant from Accuray and the National Science Foundation. We acknowledge that the reported patient cases (data and results) performed for the various clinical sites require approval and citation.

REFERENCES

1. Tripp, S. and M. Grueber, *Economic impact of the human genome project.* Battelle Memorial Institute, 2011. **58**.
2. Hamburg, M.A. and F.S. Collins, *The path to personalized medicine.* New England Journal of Medicine, 2010. **363**(4): p. 301-304.
3. Gunter, T.D. and N.P. Terry, *The emergence of national electronic health record architectures in the United States and Australia: models, costs, and questions.* Journal of medical Internet research, 2005. **7**(1).
4. Denton, B.T., et al., *Medical decision making: open research challenges.* IIE Transactions on Healthcare Systems Engineering, 2011. **1**(3): p. 161-167.
5. Jun, J., S.H. Jacobson, and J.R. Swisher, *Application of discrete-event simulation in health care clinics: A survey.* Journal of the operational research society, 1999. **50**(2): p. 109-123.
6. Miller, H.E., W.P. Pierskalla, and G.J. Rath, *Nurse scheduling using mathematical programming.* Operations Research, 1976. **24**(5): p. 857-870.
7. Lee, E.K., et al., *Machine learning for predicting vaccine immunogenicity.* Interfaces, 2016. **46**(5): p. 368-390.
8. *Stratified, personalised or P4 medicine: a new direction for placing the patient at the centre of healthcare and health education (Technical report).* . Academy of Medical Sciences., May 2015. Retrieved 6 Jan 2016.
9. Eva K. Lee, X.W., Francine Baker-Witt, Michael D. Wright, Alexander Quarshie, *Outcome-Driven Personalized Treatment Design for Managing Diabetes.* Interfaces - The Daniel H. Wagner Prize for Excellence in Operations Research Practice, To appear 2018.
10. Eva K. Lee, X.W., Francine Baker-Witt, Michael D. Wright, Alexander Quarshie, *Predicting Treatment Dose-effect Using Self-monitored Blood Glucose Data for Diabetes Management*. 2018: British Journal of Clinical Pharmacology. Manuscript sumbitted for publication.
11. Eva K. Lee, X.W., Francine Baker-Witt, Michael D. Wright, Alexander Quarshie, *Dose-effect Evidence-based Personalized Treatment Planning for Managing Gestational Diabetes Mellitus*. 2018: Diabetes Care. Manuscript sumbitted for publication.
12. Eva K. Lee, X.W., Zhuonan Li, *Isocenter Selection in Radiation Therapy Treatment Planning*. 2018: Medical Physics. Manuscript sumbitted for publication.
13. Eva K. Lee, X.W., Zhuonan Li, *A Multi-objective Direct Aperture and Beam Angle Optimization Model for External Beam Radiotherapy*. 2018: International Journal of Radiation Oncology • Biology • Physics. Manuscript sumbitted for publication.
14. Eva K. Lee, Y.C., Xin Wei, Zhuonan Li, *Strategies in Aperture Generation within a Multi-Objective Direct Aperture and Beam Angle Optimization Framework*. 2018:

International Journal of Radiation Oncology • Biology • Physics. Manuscript submitted for publication.
15. Ogurtsova, K., et al., *IDF Diabetes Atlas: Global estimates for the prevalence of diabetes for 2015 and 2040.* Diabetes research and clinical practice, 2017. **128**: p. 40-50.
16. Association, A.D., *Economic costs of diabetes in the US in 2012.* Diabetes care, 2013. **36**(4): p. 1033-1046.
17. Gardner, D.G., D. Shoback, and F.S. Greenspan, *Greenspan's basic & clinical endocrinology*. 2007: McGraw-Hill Medical.
18. Control, D., C.T.E.o.D. Interventions, and C.S.R. Group, *Intensive diabetes treatment and cardiovascular disease in patients with type 1 diabetes.* New England Journal of Medicine, 2005. **353**(25): p. 2643-2653.
19. Palmer, A.J., et al., *Outline of a diabetes disease management model: principles and applications.* Diabetes research and clinical practice, 2000. **50**: p. S47-S56.
20. Palmer, A.J., et al., *The CORE Diabetes Model: projecting long-term clinical outcomes, costs and costeffectiveness of interventions in diabetes mellitus (types 1 and 2) to support clinical and reimbursement decision-making.* Current Medical Research and Opinion®, 2004. **20**(S1): p. S5-S26.
21. Cobelli, C., et al., *Diabetes: models, signals, and control.* Biomedical Engineering, IEEE Reviews in, 2009. **2**: p. 54-96.
22. Bergman, R.N., et al., *Quantitative estimation of insulin sensitivity.* American Journal of Physiology-Endocrinology And Metabolism, 1979. **236**(6): p. E667.
23. De Winter, W., et al., *A mechanism-based disease progression model for comparison of long-term effects of pioglitazone, metformin and gliclazide on disease processes underlying type 2 diabetes mellitus.* Journal of pharmacokinetics and pharmacodynamics, 2006. **33**(3): p. 313-343.
24. Brown, S.A., R.W. Nelson, and G.D. Bottoms, *Models for the pharmacokinetics and pharmacodynamics of insulin in alloxan‐induced diabetic dogs.* Journal of pharmaceutical sciences, 1987. **76**(4): p. 295-299.
25. Hill, A.V., *The combinations of haemoglobin with oxygen and with carbon monoxide. I.* Biochemical Journal, 1913. **7**(5): p. 471.
26. Landersdorfer, C.B. and W.J. Jusko, *Pharmacokinetic/pharmacodynamic modelling in diabetes mellitus.* Clinical pharmacokinetics, 2008. **47**(7): p. 417-448.
27. Miyazaki, M., et al., *ISSN 0022-3573 Pharmacokinetic–pharmacodynamic modelling of human insulin: validity of pharmacological availability as a substitute for extent of bioavailability.* JPP, 2001. **53**: p. 1235-1246.
28. Bremer, T. and D.A. Gough, *Is blood glucose predictable from previous values? A solicitation for data.* Diabetes, 1999. **48**(3): p. 445-451.
29. Sandham, W., et al. *Neural network and neuro-fuzzy systems for improving diabetes therapy*. in *Engineering in Medicine and Biology Society, 1998. Proceedings of the 20th Annual International Conference of the IEEE*. 1998. IEEE.
30. Wang, Q., et al., *Personalized State-space Modeling of Glucose Dynamics for Type 1 Diabetes Using Continuously Monitored Glucose, Insulin Dose, and Meal Intake*

An Extended Kalman Filter Approach. Journal of diabetes science and technology, 2014. **8**(2): p. 331-345.
31. Sedigh-Sarvestani, M., D.J. Albers, and B.J. Gluckman. *Data assimilation of glucose dynamics for use in the intensive care unit*. in *Engineering in Medicine and Biology Society (EMBC), 2012 Annual International Conference of the IEEE*. 2012. IEEE.
32. Derendorf, H. and B. Meibohm, *Modeling of pharmacokinetic/pharmacodynamic (PK/PD) relationships: concepts and perspectives.* Pharmaceutical research, 1999. **16**(2): p. 176-185.
33. Gibaldi, M. and D. Perrier, *Pharmacokinetics*. 1975: Marcel Dekker.
34. Holford, N.H. and L.B. Sheiner, *Kinetics of pharmacologic response.* Pharmacology & therapeutics, 1982. **16**(2): p. 143-166.
35. Sheiner, L.B., et al., *Simultaneous modeling of pharmacokinetics and pharmacodynamics: application to d-tubocurarine.* Clinical pharmacology and therapeutics, 1979. **25**(3): p. 358-371.
36. Frey, N., et al., *Population PKPD modelling of the long‐term hypoglycaemic effect of gliclazide given as a once‐a‐day modified release (MR) formulation.* British journal of clinical pharmacology, 2003. **55**(2): p. 147-157.
37. Chan, P. and N. Holford, *Drug treatment effects on disease progression.* Annual review of pharmacology and toxicology, 2001. **41**(1): p. 625-659.
38. Schweppe, F.C., *Uncertain dynamic systems*. 1973: Prentice-Hall.
39. Gelb, A., *Applied optimal estimation*. 1974: MIT press.
40. Jovanovic, L. and D.J. Pettitt, *Gestational diabetes mellitus.* Jama, 2001. **286**(20): p. 2516-2518.
41. Metzger, B.E., et al., *Hyperglycemia and adverse pregnancy outcomes.* N Engl J Med, 2008. **358**(19): p. 1991-2002.
42. Bellamy, L., et al., *Type 2 diabetes mellitus after gestational diabetes: a systematic review and meta-analysis.* Lancet, 2009. **373**(9677): p. 1773-9.
43. Hillier, T.A., et al., *Screening for gestational diabetes mellitus: a systematic review for the U.S. Preventive Services Task Force.* Ann Intern Med, 2008. **148**(10): p. 766-75.
44. Chen, Y., et al., *Cost of gestational diabetes mellitus in the United States in 2007.* Population health management, 2009. **12**(3): p. 165-174.
45. Organization, W.H., *Diagnostic criteria and classification of hyperglycaemia first detected in pregnancy.* 2013.
46. Yogev, Y. and G.H. Visser. *Obesity, gestational diabetes and pregnancy outcome*. in *Seminars in Fetal and Neonatal Medicine*. 2009. Elsevier.
47. Beckmann, C.R.B. and A.C.O. Gynecologists, *Obstetrics and Gynecology*. 2010: Lippincott Williams & Wilkins.
48. Todorova, K., et al., *A pharmacoeconomical model for choice of a treatment for pregnant women with gestational diabetes.* Acta diabetologica, 2007. **44**(3): p. 144-148.
49. Kimber-Trojnar, Z., et al., *Glyburide for the treatment of gestational diabetes mellitus.* Pharmacological reports: PR, 2007. **60**(3): p. 308-318.

50. Dornhorst, A., et al., *Calorie restriction for treatment of gestational diabetes.* Diabetes, 1991. **40**(Supplement 2): p. 161-164.
51. Hawkins, J.S., et al., *Weekly compared with daily blood glucose monitoring in women with diet-treated gestational diabetes.* Obstetrics & Gynecology, 2009. **113**(6): p. 1307-1312.
52. Jacqueminet, S. and M.F. Jannot-Lamotte, *Therapeutic management of gestational diabetes.* Diabetes Metab, 2010. **36**(6 Pt 2): p. 658-71.
53. Jovanovic-Peterson, L., E.P. Durak, and C.M. Peterson, *Randomized trial of diet versus diet plus cardiovascular conditioning on glucose levels in gestational diabetes.* American journal of obstetrics and gynecology, 1989. **161**(2): p. 415-419.
54. Kim, C., *Gestational diabetes: risks, management, and treatment options.* International journal of women's health, 2010. **2**: p. 339.
55. Naidoo, P., R. Virendra, and M. Layla, *Effects of gliclazide dose escalation on postprandial hyperglycemia in type 2 diabetes mellitus: A prospective, open-label, case-controlled, dose-escalation study.* Current therapeutic research, 2006. **67**(2): p. 81-102.
56. Thompson, D., et al., *Prophylactic insulin in the management of gestational diabetes.* Obstetrics & Gynecology, 1990. **75**(6): p. 960-964.
57. Scarpello, J.H., *Review: Optimal dosing strategies for maximising the clinical response to metformin in type 2 diabetes.* The British Journal of Diabetes & Vascular Disease, 2001. **1**(1): p. 28-36.
58. Alwan, N., D.J. Tuffnell, and J. West, *Treatments for gestational diabetes.* The Cochrane Library, 2009.
59. Welschen, L.M., et al., *Self-monitoring of blood glucose in patients with type 2 diabetes who are not using insulin: a systematic review.* Diabetes care, 2005. **28**(6): p. 1510-1517.
60. Stewart, B. and C.P. Wild, *World cancer report 2014.* Health, 2017.
61. Khan, F.M. and B.J. Gerbi, *Treatment planning in radiation oncology*. 2012: Wolters Kluwer Health/Lippincott Williams & Wilkins.
62. Brahme, A., *Optimization of stationary and moving beam radiation therapy techniques.* Radiotherapy and Oncology, 1988. **12**(2): p. 129-140.
63. Otto, K., *Volumetric modulated arc therapy: IMRT in a single gantry arc.* Medical physics, 2008. **35**(1): p. 310-317.
64. Kilby, W., et al., *The CyberKnife® robotic radiosurgery system in 2010.* Technology in cancer research & treatment, 2010. **9**(5): p. 433-452.
65. Landberg, T., et al., *Report 50.* Journal of the International Commission on Radiation Units and Measurements, 1993. **os26**(1): p. NP-NP.
66. Schlegel, W. and A. Mahr, *3D conformal radiation therapy: Multimedia introduction to methods and techniques*. 2007: Springer Publishing Company, Incorporated.
67. Ehrgott, M., A. Holder, and J. Reese, *Beam selection in radiotherapy design.* Linear Algebra and its Applications, 2008. **428**(5-6): p. 1272-1312.
68. Siddon, R.L., *Fast calculation of the exact radiological path for a three‐dimensional CT array.* Medical physics, 1985. **12**(2): p. 252-255.

69. Bourland, J. and E. Chaney, *A finite‐size pencil beam model for photon dose calculations in three dimensions.* Medical physics, 1992. **19**(6): p. 1401-1412.
70. Gu, X., et al., *GPU-based ultra-fast dose calculation using a finite size pencil beam model.* Physics in Medicine & Biology, 2009. **54**(20): p. 6287.
71. Fippel, M., *Fast Monte Carlo dose calculation for photon beams based on the VMC electron algorithm.* Medical physics, 1999. **26**(8): p. 1466-1475.
72. Shepard, D.M., et al., *Optimizing the delivery of radiation therapy to cancer patients.* Siam Review, 1999. **41**(4): p. 721-744.
73. Langer, M., et al., *Operations research applied to radiotherapy, an NCI-NSF–sponsored workshop February 7–9, 2002.* International Journal of Radiation Oncology• Biology• Physics, 2003. **57**(3): p. 762-768.
74. Ehrgott, M. and R. Johnston, *Optimisation of beam directions in intensity modulated radiation therapy planning.* OR Spectrum, 2003. **25**(2): p. 251-264.
75. Pugachev, A. and L. Xing, *Pseudo beam's-eye–view as applied to beam orientation selection in intensity-modulated radiation therapy.* International Journal of Radiation Oncology• Biology• Physics, 2001. **51**(5): p. 1361-1370.
76. Das, S., et al., *Beam orientation selection for intensity-modulated radiation therapy based on target equivalent uniform dose maximization.* International Journal of Radiation Oncology• Biology• Physics, 2003. **55**(1): p. 215-224.
77. Meedt, G., M. Alber, and F. Nüsslin, *Non-coplanar beam direction optimization for intensity-modulated radiotherapy.* Physics in Medicine & Biology, 2003. **48**(18): p. 2999.
78. Djajaputra, D., et al., *Algorithm and performance of a clinical IMRT beam-angle optimization system.* Physics in Medicine & Biology, 2003. **48**(19): p. 3191.
79. Pugachev, A., A. Boyer, and L. Xing, *Beam orientation optimization in intensity‐modulated radiation treatment planning.* Medical Physics, 2000. **27**(6): p. 1238-1245.
80. Hou, Q., et al., *Beam orientation optimization for IMRT by a hybrid method of the genetic algorithm and the simulated dynamics.* Medical Physics, 2003. **30**(9): p. 2360-2367.
81. Schreibmann, E., et al., *Multiobjective evolutionary optimization of the number of beams, their orientations and weights for intensity-modulated radiation therapy.* Physics in Medicine & Biology, 2004. **49**(5): p. 747.
82. Li, Y., et al., *A particle swarm optimization algorithm for beam angle selection in intensity-modulated radiotherapy planning.* Physics in Medicine & Biology, 2005. **50**(15): p. 3491.
83. Ehrgott, M., H.W. Hamacher, and M. Nußbaum, *Decomposition of matrices and static multileaf collimators: a survey*, in *Optimization in medicine*. 2008, Springer. p. 25-46.
84. Brahme, A. and A. Argren, *Optimal dose distribution for eradication of heterogeneous tumors.* Acta Oncologica, 1987. **26**(5): p. 377-385.
85. Lim, G.J., et al., *An optimization framework for conformal radiation treatment planning.* INFORMS Journal on Computing, 2007. **19**(3): p. 366-380.

86. Xing, L., et al., *Fast iterative algorithms for three‐dimensional inverse treatment planning.* Medical Physics, 1998. **25**(10): p. 1845-1849.
87. Niemierko, A., *Reporting and analyzing dose distributions: a concept of equivalent uniform dose.* Medical physics, 1997. **24**(1): p. 103-110.
88. Niemierko, A., *A generalized concept of equivalent uniform dose (EUD).* Med Phys, 1999. **26**(6): p. 1100.
89. Choi, B. and J.O. Deasy, *The generalized equivalent uniform dose function as a basis for intensity-modulated treatment planning.* Physics in Medicine & Biology, 2002. **47**(20): p. 3579.
90. Webb, S., *Optimization by simulated annealing of three-dimensional conformal treatment planning for radiation fields defined by a multileaf collimator.* Physics in Medicine & Biology, 1991. **36**(9): p. 1201.
91. Wu, Q., et al., *Optimization of intensity-modulated radiotherapy plans based on the equivalent uniform dose.* International Journal of Radiation Oncology• Biology• Physics, 2002. **52**(1): p. 224-235.
92. Peñagarícano, J.A., et al., *An assessment of biologically-based optimization (BORT) in the IMRT era.* Medical Dosimetry, 2005. **30**(1): p. 12-19.
93. Morrill, S.M., et al., *Dose‐volume considerations with linear programming optimization.* Medical Physics, 1991. **18**(6): p. 1201-1210.
94. Romeijn, H.E., et al., *A novel linear programming approach to fluence map optimization for intensity modulated radiation therapy treatment planning.* Physics in Medicine & Biology, 2003. **48**(21): p. 3521.
95. Deasy, J., *Multiple local minima in radiotherapy optimization problems with dose–volume constraints.* Medical physics, 1997. **24**(7): p. 1157-1161.
96. Lee, E.K., T. Fox, and I. Crocker, *Simultaneous beam geometry and intensity map optimization in intensity-modulated radiation therapy.* International Journal of Radiation Oncology• Biology• Physics, 2006. **64**(1): p. 301-320.
97. Lee, E.K., T. Fox, and I. Crocker, *Integer programming applied to intensity-modulated radiation therapy treatment planning.* Annals of Operations Research, 2003. **119**(1-4): p. 165-181.
98. Lee, E.K., T. Fox, and I. Crocker, *Optimization of radiosurgery treatment planning via mixed integer programming.* Medical physics, 2000. **27**(5): p. 995-1004.
99. Wang, C., J. Dai, and Y. Hu, *Optimization of beam orientations and beam weights for conformal radiotherapy using mixed integer programming.* Physics in Medicine & Biology, 2003. **48**(24): p. 4065.
100. Jee, K.-W., D.L. McShan, and B.A. Fraass, *Lexicographic ordering: intuitive multicriteria optimization for IMRT.* Physics in Medicine & Biology, 2007. **52**(7): p. 1845.
101. Wilkens, J.J., et al., *IMRT treatment planning based on prioritizing prescription goals.* Physics in Medicine & Biology, 2007. **52**(6): p. 1675.
102. Breedveld, S., P.R. Storchi, and B.J. Heijmen, *The equivalence of multi-criteria methods for radiotherapy plan optimization.* Physics in Medicine & Biology, 2009. **54**(23): p. 7199.

103. Sun, X. and P. Xia, *A new smoothing procedure to reduce delivery segments for static MLC‐based IMRT planning.* Medical physics, 2004. **31**(5): p. 1158-1165.
104. Webb, S., D. Convery, and P. Evans, *Inverse planning with constraints to generate smoothed intensity-modulated beams.* Physics in Medicine & Biology, 1998. **43**(10): p. 2785.
105. Bortfeld, T.R., et al., *X-ray field compensation with multileaf collimators.* International Journal of Radiation Oncology• Biology• Physics, 1994. **28**(3): p. 723-730.
106. Ahuja, R.K. and H.W. Hamacher, *A network flow algorithm to minimize beam‐on time for unconstrained multileaf collimator problems in cancer radiation therapy.* Networks, 2005. **45**(1): p. 36-41.
107. Baatar, D., et al., *Decomposition of integer matrices and multileaf collimator sequencing.* Discrete Applied Mathematics, 2005. **152**(1-3): p. 6-34.
108. Siochi, R.A.C., *Minimizing static intensity modulation delivery time using an intensity solid paradigm.* International Journal of Radiation Oncology• Biology• Physics, 1999. **43**(3): p. 671-680.
109. Ernst, A.T., V.H. Mak, and L.R. Mason, *An exact method for the minimum cardinality problem in the treatment planning of intensity-modulated radiotherapy.* INFORMS Journal on Computing, 2009. **21**(4): p. 562-574.
110. Mak, V., *Iterative variable aggregation and disaggregation in IP: An application.* Operations research letters, 2007. **35**(1): p. 36-44.
111. Engel, K., *A new algorithm for optimal multileaf collimator field segmentation.* Discrete Applied Mathematics, 2005. **152**(1-3): p. 35-51.
112. Shepard, D., et al., *Direct aperture optimization: A turnkey solution for step‐and‐shoot IMRT.* Medical physics, 2002. **29**(6): p. 1007-1018.
113. Cassioli, A. and J. Unkelbach, *Aperture shape optimization for IMRT treatment planning.* Physics in Medicine & Biology, 2012. **58**(2): p. 301.
114. Hardemark, B., et al., *Direct machine parameter optimization with RayMachine in Pinnacle.* Ray-Search White Paper, 2003.
115. Romeijn, H.E., et al., *A column generation approach to radiation therapy treatment planning using aperture modulation.* SIAM Journal on Optimization, 2005. **15**(3): p. 838-862.
116. Preciado-Walters, F., et al., *Column generation for IMRT cancer therapy optimization with implementable segments.* Annals of Operations Research, 2006. **148**(1): p. 65-79.
117. Jin, X., et al., *Technical and Dosimetric Considerations in Multi-Isocenter Intensity Modulated Radiotherapy for Nasopharyngeal carcinoma with Small Multileaf Collimator.* Medical Dosimetry, 2009. **34**(1): p. 9-15.
118. Liao, R., et al., *Optimization of multiple‐isocenter treatment planning for linac‐based stereotactic radiosurgery.* Computer Aided Surgery, 2000. **5**(4): p. 220-233.
119. Welzl, E., *Smallest enclosing disks (balls and ellipsoids)*, in *New results and new trends in computer science*. 1991, Springer. p. 359-370.

120. Cazals, F., H. Kanhere, and S. Loriot, *Computing the volume of a union of balls: a certified algorithm.* ACM Transactions on Mathematical Software (TOMS), 2011. **38**(1): p. 3.
121. Lloyd, S., *Least squares quantization in PCM.* IEEE transactions on information theory, 1982. **28**(2): p. 129-137.
122. Drezner, Z. and H.W. Hamacher, *Facility location: applications and theory*. 2001: Springer Science & Business Media.
123. Schlaefer, A. and A. Schweikard, *Stepwise multi‐criteria optimization for robotic radiosurgery.* Medical physics, 2008. **35**(5): p. 2094-2103.
124. Mohan, R., et al., *The impact of fluctuations in intensity patterns on the number of monitor units and the quality and accuracy of intensity modulated radiotherapy.* Medical physics, 2000. **27**(6): p. 1226-1237.
125. Craft, D., P. Süss, and T. Bortfeld, *The tradeoff between treatment plan quality and required number of monitor units in intensity-modulated radiotherapy.* International Journal of Radiation Oncology• Biology• Physics, 2007. **67**(5): p. 1596-1605.
126. Men, C., et al., *An exact approach to direct aperture optimization in IMRT treatment planning.* Physics in Medicine & Biology, 2007. **52**(24): p. 7333.
127. Attix, F.H., *Introduction to radiological physics and radiation dosimetry*. 2008: John Wiley & Sons.
128. Dong, P., et al., *4π non-coplanar liver SBRT: a novel delivery technique.* International Journal of Radiation Oncology• Biology• Physics, 2013. **85**(5): p. 1360-1366.
129. Lukka, H., J. Bahary, and C. Lawton, *RTOG 0938: A randomized phase II trial of hypofractionated radiotherapy for favorable risk prostate cancer.* RTOG, Hamilton, Canada, 2015.
130. Group, R.T.O., *RTOG 0813: Seamless phase I/II study of stereotactic lung radiotherapy (SBRT) for early stage, centrally located, non-small cell lung cancer (NSCLC) in medically inoperable patients.* Philadelphia, PA: Radiation Therapy Oncology Group, 2010.